The study of $D^\pm$ and D^0 meson production in deep inelastic scattering at HERA II with the ZEUS detector.

Daniel Nicholass

University College London

August 2008

Submitted to University College London in fulfilment

of the requirements for the award of the

degree of Doctor of Philosophy.

Abstract

Installed in 2000/2001, the ZEUS micro vertex detector provided the capability to reconstruct secondary vertices displaced from the primary by distances of the order 100 μm. In order to be useful for tagging heavy flavour mesons the micro vertex detector was aligned with a combination of tracks from cosmic events and ep events in the HERA collider.

This thesis presents measurements of $D^\pm$ and D^0 meson production obtained with the ZEUS detector at HERA using an integrated luminosity of 133.6 pb^{-1}. The measurements cover the kinematic range $5 < Q^2 < 1000$ GeV^2, $0.02 < y < 0.7$, $1.5 < p_T^D < 15$ GeV and $|\eta^D| < 1.6$. Combinatorial background to the D meson signals is reduced by using the ZEUS micro vertex detector to reconstruct displaced secondary vertices. Production cross sections are compared with the predictions of next-to-leading order QCD which is found to describe the data well. Measurements are extrapolated to the full kinematic phase space in order to obtain the open charm contribution, $F_2^{c\bar{c}}$, to the proton structure function, F_2.

Acknowledgements

Outline

In this thesis an analysis of $D^{\pm}$ and D^0 meson production in deep inelastic scattering at HERA II and an extraction of the open charm contribution, $F_2^{c\bar{c}}$, to the proton structure function, F_2, is presented. The analysis was performed with 133.6 pb^{-1} of data collected with the ZEUS detector in the period 2004-2005. Chapter 1 briefly outlines the kinematics of a deep inelastic scattering (DIS) event and the theoretical picture of the process. Chapter 2 begins with a discussion of charm production in DIS before moving onto the properties of D mesons and the measurement of charm at HERA. Chapter 3 describes the HERA ep collider and the ZEUS detector with more detail given for the components most relevant to this thesis. In Chapter 4 the alignment of the micro vertex detector is discussed with the procedure using tracks from ep collisions emphasised, This was a necessary first step for the later analysis of $D^{\pm}$ and D^0 mesons. Chapter 5 describes the reconstruction of the DIS events, D mesons and lifetime based variables used for the analysis. Chapters 6-8 constitute the main analysis work in this thesis. Chapter 6 begins with a brief description of the Monte Carlo sample used before detailing the procedures used to correct and validate this sample for use in the analysis. Finally the analysis procedure and results are given in Chapters 7 and 8 along with a summary and discussion of future potential.

Contents

List of Figures

11

12

15

16

17

19

List of Tables

21

Chapter 1

Deep inelastic scattering

This chapter will discuss deep inelastic scattering (DIS) and the current under-standing of the internal structure of the proton. The Lorentz invariant kinematic variables used to describe DIS events are introduced before structure functions and their evolution are discussed.

1.1 Neutral current DIS

A neutral current deep inelastic event between an electron and a proton occurs when the electron emits an off-shell (virtual) photon or Z^0 boson which interacts with a constituent of the proton causing the proton to break up. As the virtual photon interacts with an internal constituent of the proton such processes provide information about the proton's underlying structure. A diagram of a DIS event is shown in figure 1.1. In the diagram the quantities k, k' and p represent the four-momenta of the incoming electron, outgoing electron and incoming proton respectively. The four-momentum of the exchanged boson, q, is given by the difference in the four-momentum of the electron before and after the boson's emission,
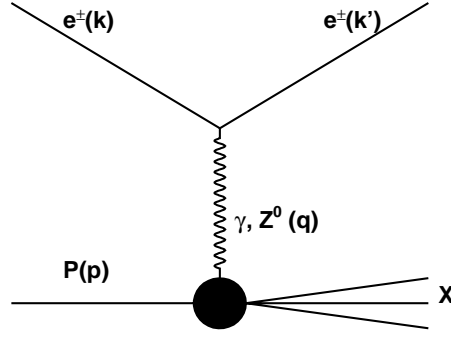
Figure 1.1: *Feynman diagram of neutral current DIS.*

$$q = k - k' \tag{1.1}$$

The scattering process can be described by the following Lorentz scalars:

$$Q^2 = -q^2 = (k - k')^2, \tag{1.2}$$

$$s = (k + P)^2 \simeq 2k \cdot P, \tag{1.3}$$

$$y = \frac{P \cdot q}{P \cdot k} \simeq \frac{2P \cdot q}{s}, \tag{1.4}$$

$$x = \frac{Q^2}{2P \cdot q}. \tag{1.5}$$

These are associated by the relation:

$$Q^2 = sxy, \tag{1.6}$$

where s is the square of the centre of mass energy, y and x are the Bjorken scaling variables and Q^2 is the virtuality of the exchanged boson. At HERA the centre of mass energy of the ep collision is $\sqrt{s} = 318$ GeV^2. The Q^2 scalar can be seen as a measure of the resolving power of the event with higher values of Q^2 corresponding to higher momentum transfer and as such greater resolving power. This implies that at high Q^2 the photon resolves the proton at the parton level

rather than the proton as a whole. The variable y can be seen as the inelasticity of the event; it gives the fraction of the electron energy involved in the process as measured in the proton rest frame. Finally, x measures the fraction of the proton momentum carried by the struck parton.

1.2 Structure functions and the quark-parton model

Feynman's parton model [1] assumed the proton to be composed of point-like free objects called partons meaning that inelastic ep collisions can be viewed as elastic electron-parton events. In the infinite momentum frame of the proton the partons can be assumed to have zero transverse momentum and therefore by neglecting the proton and parton masses and requiring 4-momentum conservation the following relation can be obtained:

$$0 \approx m^2 = (\xi p + q)^2 = \xi^2 p^2 - Q^2 + 2\xi p \cdot q \tag{1.7}$$

$$\implies \xi = \frac{Q^2}{2p \cdot q} = x \tag{1.8}$$

Where ξ is the fraction of the proton momentum carried by the struck parton and p, q and x are the previously defined variables. From this relation we conclude that in the infinite momentum frame, the Bjorken scaling variable x can be interpreted as the fraction of the longitudinal proton momentum carried by the parton in the hard scatter.

At this point we introduce the concept of the proton structure functions, F_i, which describe the momentum distributions of the partons within the proton, the shape of which cannot be calculated using current mathematical knowledge. The DIS cross section in terms of these functions is:

$$\frac{d\sigma(e^{\pm}p)}{dxdQ^2} = \frac{2\pi\alpha^2}{xQ^4} \left[Y_+ F_2 - y^2 F_L \mp Y_- xF_3 \right] \tag{1.9}$$

25

where, $Y_{\pm} = 1 \pm (1-y)^2$ and α is the electromagnetic coupling constant. The F_2, F_L and F_3 structure functions describe the neutral current scattering, coupling to longitudinally polarised photons and the parity violation arising from Z^0 exchange respectively. The xF_3 term is neglected in this thesis as low Q^2 $(Q^2 < M_Z^2)$ events are dominated by virtual photon exchange. The y^2F_L term is also neglected as it is only significant at high y and all measurements contained in this thesis are for $y < 0.7$. It was predicted [2] that in the limit $Q^2 \to \infty$, $\nu \to \infty$, where $\nu = \frac{p \cdot q}{M}$, the proton structure functions would depend on a single variable, x, giving:

$$F_1(x) = \frac{1}{2} \sum_i e_i^2 \left(q_i(x) + \bar{q}_i(x) \right) \tag{1.10}$$

$$F_2(x) = x \sum_i e_i^2 \left(q_i(x) + \bar{q}_i(x) \right) \tag{1.11}$$

where,

$$F_L(x) = F_2(x) - 2xF_1(x) \tag{1.12}$$

and $q_i(x)$ are the Parton Distribution Functions (PDFs). These describe the probability of finding a parton at a given value of x. This prediction, known as Bjorken scaling, was confirmed at SLAC at $Q^2 \approx 4\,\mathrm{GeV}^2$ [3]. The underlying partons of the proton were identified as quarks which were first predicted by Murray Gell-Mann in the 1960's [4]. Quarks are spin $1/2$ fermions resulting in F_L being zero which in turn leads to the Callan-Gross relation

$$2xF_1(x) = F_2(x) \tag{1.13}$$

1.2.1 The improved quark-parton model

If a proton is composed solely of 3 quarks then the sum of the fractional momentum of these quarks should equal unity.

$$\sum_i \int_0^1 dx\, f_i(x)\, x = 1 \tag{1.14}$$

26

Experimentally this sum was found to be ≈ 0.5 [5] which led to the conclusion that 50% of the proton momentum is carried by neutral particles. These partons are known as gluons; observational evidence for these partons was found in e^+e^- collisions in the form of 3-jet events at the TASSO and Jade experiments [6]. Following the discovery of gluons the quark-parton model (QPM) was modified to include quarks which interact via gluon exchange. This became quantum chromodynamics (QCD) in which gluons themselves can split into quark or gluon pairs. If a quark radiates a gluon it can result in the quark having a transverse momentum in relation to the direction of the proton velocity, the result being that coupling to longitudinally polarised photons is then possible leading to a violation of the Callan-Gross relation. The value of the longitudinal structure function, F_L, is therefore no longer zero but lies in the range $0 < F_L < F_2$.

The QCD picture of the proton is one of a dynamic system in which quark and gluon pairs are constantly being created and annihilated. As this system is probed at ever increasing values of Q^2 more of the proton substructure and hence greater numbers of partons are resolved. This is known as scaling violation and introduces a logarithmic dependence on Q^2 into the structure functions. This feature was measured at HERA [7] and can be clearly seen in figure 1.2.

1.3 Measurement and Evolution of the Parton Densities

The precise mathematical form of the PDFs cannot be predicted from first principles. However, postulations can be made to justify some functional form which is then fit to structure function measurements from a number of HEP experiments. The ZEUS, H1, CTEQ and MRST groups all produce PDFs by fitting to experimental data, examples of different PDF sets can be seen in figure 1.3.
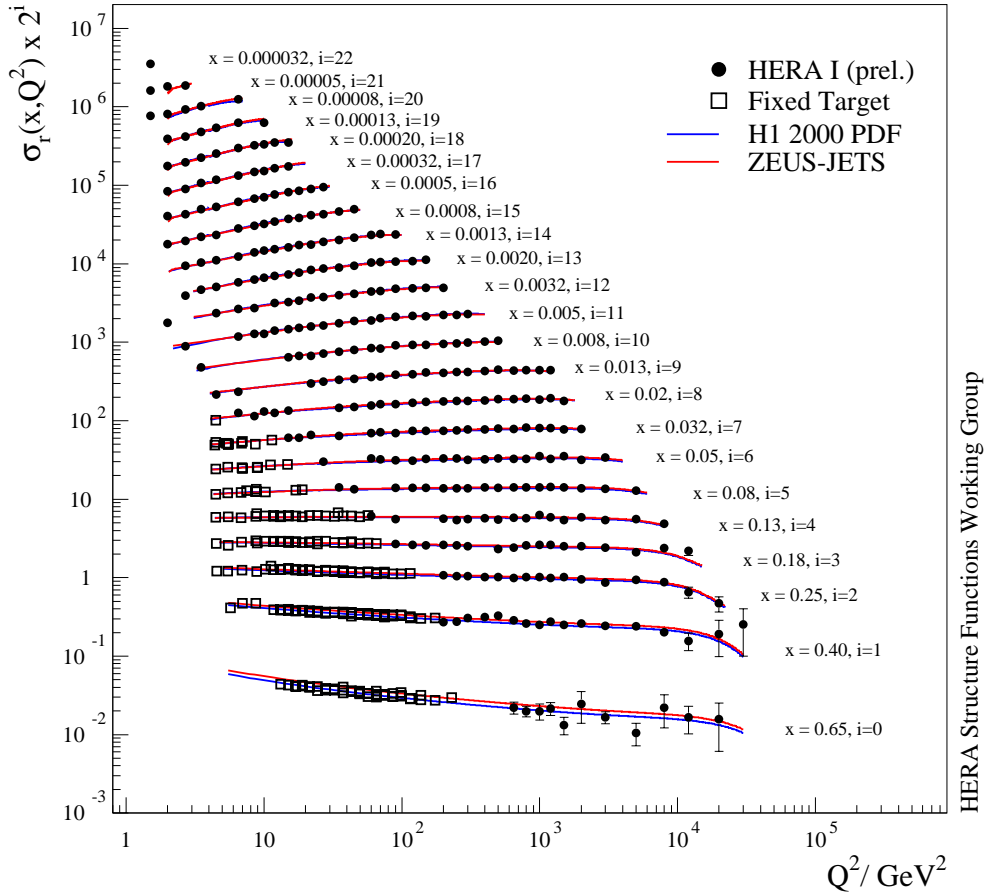
Figure 1.2: *The reduced cross section, $\sigma_r(x, Q^2)$, as a function of Q^2 for fixed x. This is proportional to the structure function F_2 when F_L and xF_3 are neglected. Fixed-target results and the combined H1-ZEUS HERA I measurements are compared to the H1 and ZEUS NLO QCD fits.*
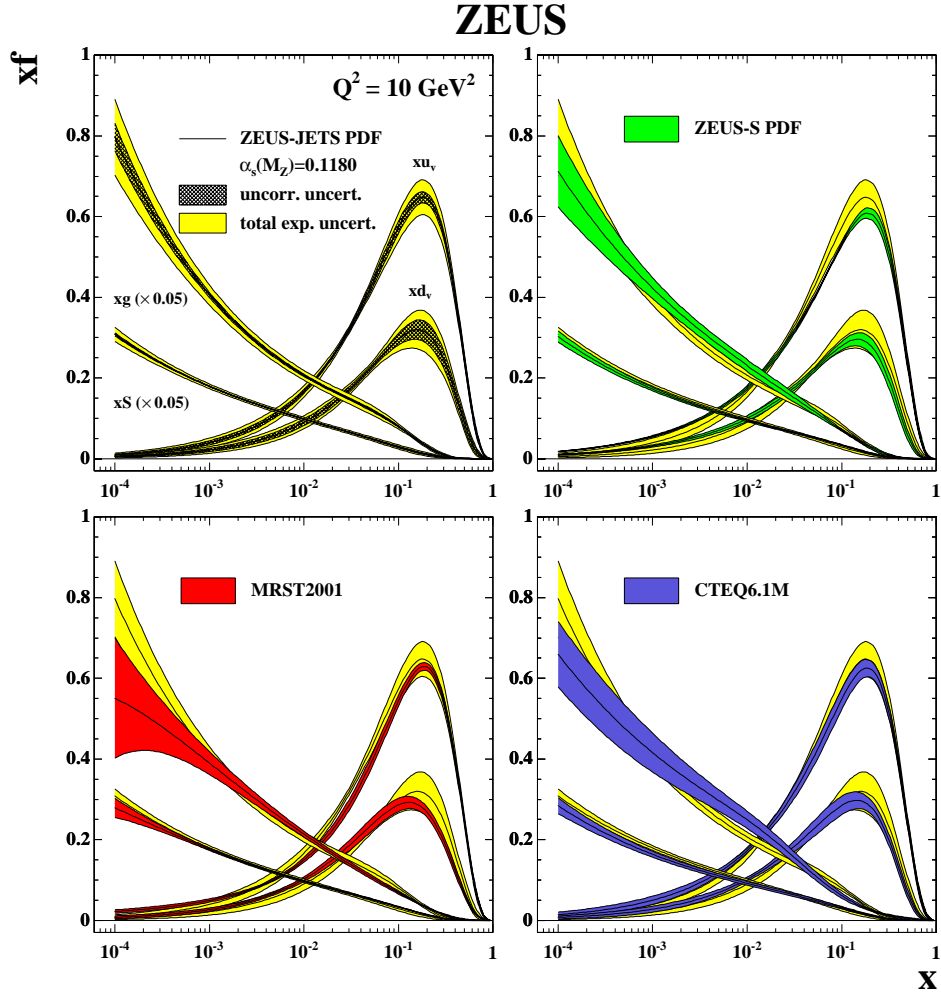
Figure 1.3: *PDFs extracted from (a) the ZEUS-JETS fit (b) the ZEUS-JETS fit compared to ZEUS-S PDFs (c) ZEUS-JETS PDFs compared to MRST2001 PDFs [8] and (d) ZEUS-JETS PDFs compared to CTEQ6.1 PDFs [9].*
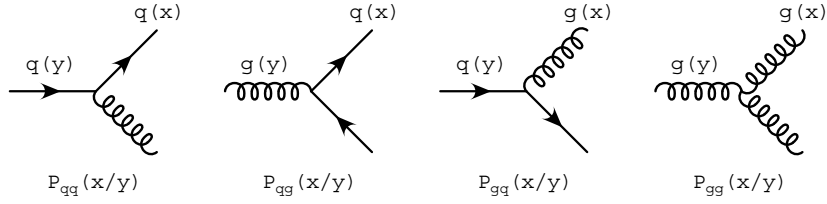
Figure 1.4: *Illustration of the leading order splitting functions, P_{ij}, used in the DGLAP equations.*

The physics governing the proton substructure is expected to be universal and independent of the scattering process and so it follows that the same will be true for proton PDFs. However, due to its Q^2 dependence, before a PDF measured at one experiment can be used at another it must be evolved to the correct scale. One method for this evolution is via the Dokshitzer-Gribov-Lipatov-Altarelli-Parisi (DGLAP) equation [10]. For the evolution of a quark distribution this is given by:

$$\frac{\partial q_i(x, Q^2)}{\partial \ln Q^2} = \frac{\alpha_s(Q^2)}{2\pi} \int_x^1 \frac{d\xi}{\xi} \left[\sum_j q_j(\xi, Q^2) P_{q_i q_j}\left(\frac{x}{\xi}\right) + g(\xi, Q^2) P_{q_i g}\left(\frac{x}{\xi}\right) \right]$$
(1.15)

and for the gluon by:

$$\frac{\partial g_i(x, Q^2)}{\partial \ln Q^2} = \frac{\alpha_s(Q^2)}{2\pi} \int_x^1 \frac{d\xi}{\xi} \left[\sum_j q_j(\xi, Q^2) P_{g q_j}\left(\frac{x}{\xi}\right) + g(\xi, Q^2) P_{gg}\left(\frac{x}{\xi}\right) \right]$$
(1.16)

where the P_{ij} terms are the "splitting" functions which may be interpreted as the probability of parton i being emitted by parton j with a fraction x/ξ of parton j's momentum. The splitting functions are the result of the idea that the particle involved in the hard scatter may not have originally been a constituent of the proton and may itself have radiated another particle prior to the scattering event. The leading order splitting function used in the DGLAP equations are illustrated in figure 1.4.

1.4 Summary

This chapter outlined the principles of deep inelastic scattering along with our current understanding of the underlying structure of the proton. The proton is seen as a dynamic system containing 3 valence quarks and a continuously fluctuating sea of gluons and $q\bar{q}$ pairs. The distribution of these partons is described by structure functions, the forms of which must be measured experimentally at a given scale. A structure function measured at one experiment can be evolved to a suitable scale for use at another experiment using the DGLAP equations.

Chapter 2

Charm at HERA

2.1 The discovery of the c quark

In the early 1970's the QPM had yet to be accepted as the underlying basis for hadronic structure and was regarded by some as a mathematical trick rather than an underlying truth. One of the main shortcomings of the model was its prediction of flavour changing neutral currents between the currently known quark flavours up, u, down, d and strange s. The solution to this problem [11] was the introduction of a fourth as yet unidentified quark, charm (c) and when a narrow resonance state at 3.1 GeV was simultaneously discovered at SLAC and Brookhaven in 1974 [12] it was identified as the bound $c\bar{c}$ state and the QPM was fully accepted.

2.2 Charm production at HERA

The mass of the charm quark ($m_c \approx 1.5$ GeV) leads to its suppression in the quark-gluon sea of the proton and therefore leading order production of c quarks at HERA occurs by boson-gluon fusion (BGF) [13]. This process is illustrated in figure 2.1, where a quark in the proton emits a gluon with momentum ξP. This then splits
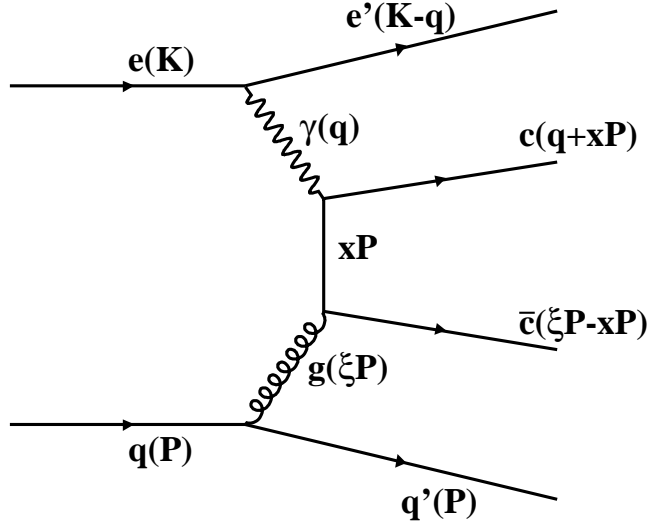
Figure 2.1: *$c\bar{c}$ pair production in boson-gluon fusion.*

into a $c\bar{c}$ pair, one with momentum xP which interacts with the virtual photon and one with momentum $P(\xi - x)$. The large value of m_c poses certain challenges to the theoretical treatment of the production as it can spoil the convergence of the perturbative series due to the presence of $\log(m_c/Q^2)$ terms. Three regimes exist for the treatment of massive quarks and these are summarised below:

- *Zero Mass Variable Flavour Number Scheme (ZM-VFNS):* m_c is considered to be zero with charm production only turning on at a predetermined scale. This treatment is expected to be valid for scales much larger than m_c.

- *Fixed Flavour Number Scheme (FFNS):* Charm quarks are not considered as partons in the PDFs and are only produced in the final state with m_c chosen to be some sensible value; at HERA the production is dominated by BGF. This treatment is expected to be valid at scales near m_c.

- *General Mass Variable Flavour Number scheme (GM-VFNS):* The charm quark is treated as massive, with the formalism tending to the FFNS, at scales

33

Parameter	Value
Proton PDF	ZEUS-S
Charm mass (m_c)	1.5 GeV
Peterson Parameter ($\epsilon_{Pet.}$)	0.035
Renormalisation and Factorisation scale (μ)	$\sqrt{Q^2 + 4m_c^2}$

Table 2.1: *Inputs to the HVQDIS program.*

near m_c and the ZM-VFNS at scales much greater than the charm mass.

Only the massive scheme as formalised in the HVQDIS program [14] is used for theoretical comparisons in this thesis as formulations of the other schemes are not currently available.

2.2.1 HVQDIS

The HVQDIS program was used to calculate D meson cross sections at next-to-leading order. The program allows calculation of both total and differential cross sections in kinematic variables such as Q^2 and x and hadronic variables such as p_T^D in a defined kinematic range. Calculations are performed in the fixed-flavour-number scheme (FFNS) which assumes the proton consists of only the lightest three quarks. This means that the only mechanism available for heavy flavour production is BGF. After the production of the heavy flavour quark, fragmentation occurs in accord with the Peterson fragmentation function (section 2.2.1). The input parameters used to obtain the predictions are summarised in table 2.1. Where the ZEUS-S PDF is a next-to-leading order QCD fit to structure function data in the FFNS with the QCD cut off scale, $\Lambda_{QCD}^{(3)} = 0.363$ GeV. The charm mass was set to be consistent with the best value in global QCD fits with $m_c = 1.5$ GeV [15].

To estimate the contribution of beauty production, the NLO calculation and
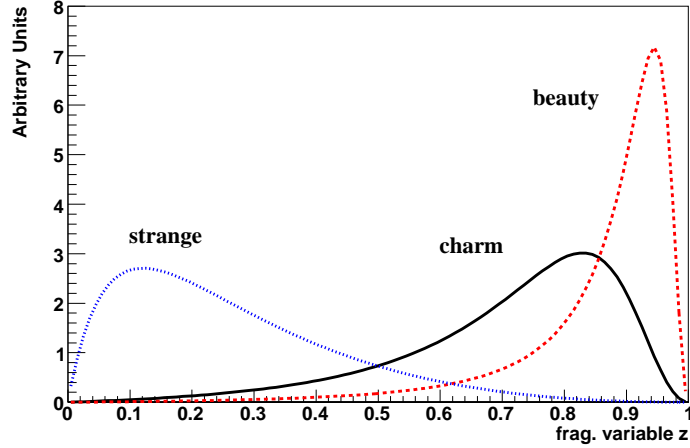
Figure 2.2: *Peterson fragmentation function as a function of the fragmentation variable, z, for s, c and b quarks.*

hadronisation from the Monte Carlo were combined, using $d\sigma(b \to D)_{\text{NLO+MC}} = d\sigma(b\bar{b})_{\text{NLO}} \cdot \mathcal{C}_{had}$ where $\mathcal{C}_{had} = d\sigma(b \to D)_{\text{MC}}/d\sigma(b\bar{b})_{\text{MC}}$. The ZEUS NLO QCD fit was used as the proton PDF, so that the mass used in this fit was also used in the HVQDIS program. The hadronisation fraction, $f(b \to D)$, was set to 0.231 and 0.596 for the $D^{\pm}$ and D^0 respectively [16] with the beauty mass set to $m_b = 4.3$ GeV.

Peterson fragmentation

The Peterson fragmentation describes the fractional energy of a quark that is retained by the colourless hadron. By kinematic considerations it is suggested that the shape of the fragmentation function will vary strongly with the mass of the quark [17]. The result is that a greater fraction of a heavy quark's momentum will be passed to the hadron than that for a light quark. The functional form is:

$$D_Q(z) \propto \frac{1}{z\left[1 - \left(\frac{1}{z}\right) - \frac{\epsilon}{(1-z)}\right]^2} \tag{2.1}$$

where z is the ratio of the hadron momentum to the quark momentum and ϵ is a tunable parameter which in this analysis is set to $\epsilon = 0.035$ [18]. Figure 2.2 shows the function for the three heaviest quarks produced at HERA with the heaviest, b, peaking at a far higher value than the lightest.

2.3 The D mesons

Name	Constituents	Charge	Isospin	Angular Momentum	Mass (MeV)	$c\tau(\mu m)$
D^+	$c\bar{d}$	e	$\frac{1}{2}$	0	1869.3 ± 0.4	311.8 ± 2.1
D^0	$c\bar{u}$	0	$\frac{1}{2}$	0	1864.5 ± 0.4	122.9 ± 0.4
D_s^+	$c\bar{s}$	e	0	0	1968.2 ± 0.5	149.9 ± 2.1
D^{*+}	$c\bar{d}$	e	$\frac{1}{2}$	1	2010.0 ± 0.4	

Table 2.2: *Property summary of four commonly studied D mesons [19].*

As charm cannot be observed in the final state, production is often studied in the D sector using the four mesons most easily reconstructed in an experimental situation: D^+, D^0, D_s^+ and D^{*+}, the properties of which are summarised in Table 2.2. Charm quarks produced in a hard scatter will hadronise to these D mesons in fractions which are expected to be independent of the process which created them. Table 2.3 shows the hadronisation fractions for four D mesons as measured in DIS, photoproduction (γp) and electron-positron (e^+e^-) annihilation. The values agree within uncertainties reinforcing the idea that fragmentation can be treated as independent of the hard process. These hadronisation fractions are defined as the ratio of the production cross section for a given meson to the sum of the production cross sections for all charm ground states that decay weakly. In the

	ZEUS (DIS) [20]	ZEUS (γp) [21]	Combined e^+e^- [22]	H1 (DIS) [23]
$f(c \to D^+)$	$0.216\,^{+0.021}_{-0.029}$	$0.217\,^{+0.024}_{-0.022}$	$0.226\,^{+0.019}_{-0.017}$	0.203 ± 0.026
$f(c \to D^0)$	$0.605\,^{+0.027}_{-0.060}$	$0.523\,^{+0.035}_{-0.042}$	$0.557\,^{+0.027}_{-0.026}$	0.560 ± 0.046
$f(c \to D_s^+)$	$0.092\,^{+0.018}_{-0.017}$	$0.095\,^{+0.028}_{-0.019}$	$0.101\,^{+0.035}_{-0.022}$	0.151 ± 0.055
$f(c \to D^{*+})$	$0.229\,^{+0.014}_{-0.026}$	$0.200\,^{+0.014}_{-0.016}$	0.238 ± 0.008	0.263 ± 0.032

Table 2.3: *The fraction of c quarks hadronising as a particular D meson, $f(c \to D)$, as measured in various processes.*

analyses detailed in this thesis hadronisation fractions are used to extract $F_2^{c\bar{c}}$ from the $D^{\pm}$ and D^0 production cross sections.

2.3.1   Lifetimes of the ground state D mesons

One important property of the ground state D mesons is their proper times, $c\tau$, which are found to be of the order 100 μm (Table 2.2). From a naive spectator driven model of D meson decay (figure 2.3) it would be expected that the lifetimes of the charged and neutral mesons should be almost identical [24] but this is clearly not borne out by the data. Several unknown contributions to the overall decay width exist, which could potentially explain the discrepancy:

- The presence of two same-state $\bar{d}$ in the final state extends the D^+ lifetime due to Pauli interference;

- Weak annihilation of the c and $\bar{d}$ in the D^+;

- W boson exchange between the c and $\bar{u}$ in the D^0.

The amplitudes of the last two decays are expected to be small due to helicity and colour suppression although in both cases this suppression can be overcome by the
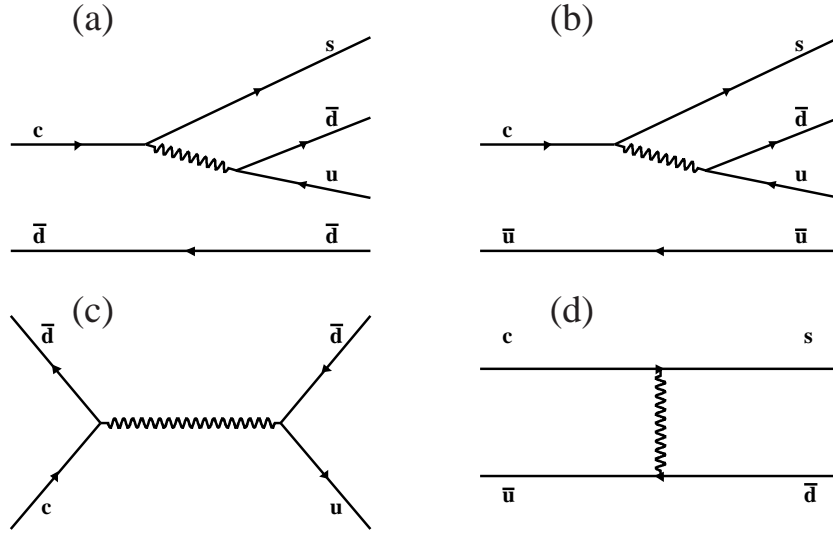
Figure 2.3: *Spectator decay diagrams for (a) D^+ and (b) D^0 mesons along with (c) weak annihilation for the D^+ and (d) W exchange for the D^0.*

emission of a gluon.

2.4   Identification of charm production events at HERA

The production of charm at HERA has been identified through several methods the most widely used of which tags the c quark through the reconstruction of a $D^{*\pm}$ meson via the decay chain

$$D^{*\pm} \to D^0 + \pi_s$$
$$D^0 \to K^{\mp}\pi^{\pm}$$

where π_s signifies a "slow" pion. This decay chain can be reconstructed with very little background due to the double tag afforded by the D^0 and the slow pion. Figure 2.4 shows the clean signal obtained from 81.9 pb^{-1} of ZEUS data [25]. The combined branching ratio for this decay chain is 2.6 % meaning that the vast majority of $D^{*\pm}$ mesons produced are not reconstructed. Additionally, most c
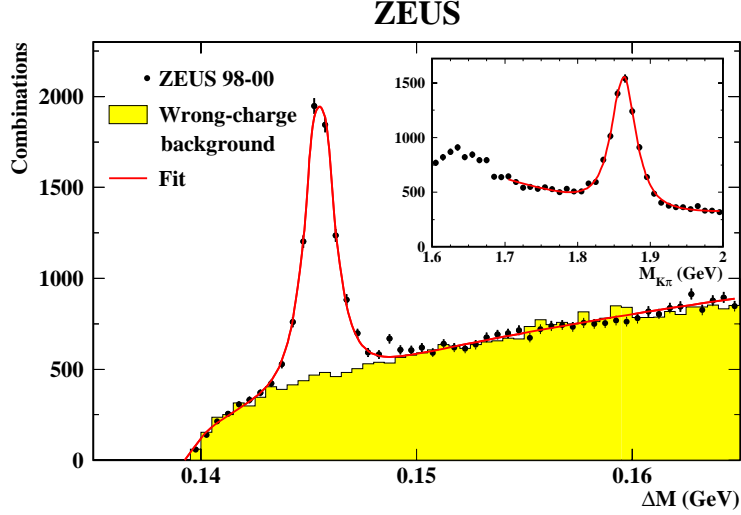
Figure 2.4: *The distribution of the mass difference, $\Delta M = (M_{K\pi\pi_s} - M_{K\pi})$, for $D^{*\pm}$ candidates (solid dots) for 81.9 pb^{-1} of ZEUS data. The $M_{K\pi}$ distribution for the D^0 candidates in the range $0.143 < \Delta M < 0.148$ GeV is shown as an inset [25].*

quarks produced will not fragment to a $D^{*\pm}$ and so any information inferred about c production from $D^{*\pm}$ mesons alone is subject to large correction factors. Charm production can also be studied by the reconstruction of the weakly decaying D mesons $D^{\pm}$, D^0 and $D_s^{\pm}$. The normally large backgrounds to these mesons can be reduced through the use of precision tracking to tag candidates through displaced vertices. This technique was first used at HERA by the H1 collaboration [23]. Figure 2.5 shows the effectiveness of using lifetime tags in reducing backgrounds for D^+ mesons reconstructed in the decay chain $D^+ \rightarrow K^-\pi^+\pi^+$. The most inclusive method of charm identification used at HERA to date does not rely on the explicit reconstruction of a charmed meson candidate but the distance of closest approach or impact parameter between a track and the primary vertex [26]. As a charmed meson will travel a relatively long distance before decaying weakly, any tracks produced by the decay will not pass through the primary vertex and hence will have a significant impact parameter. By choice of an appropriate sign
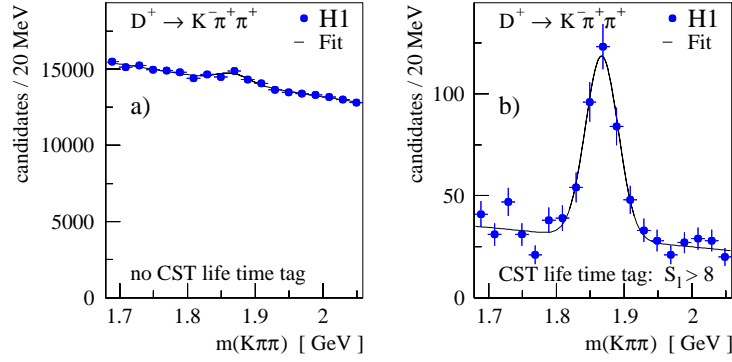
Figure 2.5: *Invariant mass distributions $M_{K\pi\pi}$ for $D^+ \to K^-\pi^+\pi^+$ decay candidates (a) before and (b) after a displaced vertex based cut with 47.8 pb^{-1} of H1 data [23].*
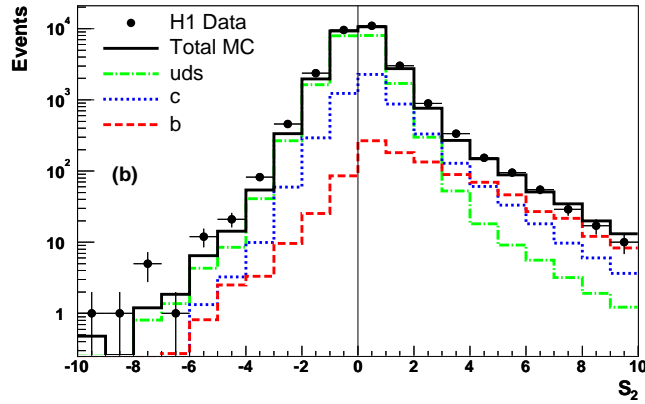
Figure 2.6: *The distribution of the signed impact parameter significance, S_2, relative to the primary vertex in the xy plane for 57.4 pb^{-1} of H1 data. The distribution is shown for tracks with the second highest significance, defined as the impact parameter divided by the uncertainty on the impact parameter. The light flavour, c and b expectation from MC is also shown.*

convention for this impact parameter the fraction of charm (and beauty) present in the data sample can be extracted. Figure 2.6 shows the distribution of the signed impact parameter significance, $S = \delta/\sigma(\delta)$, for tracks reconstructed in 57.4 pb^{-1} of H1 data. The charm and beauty contributions as predicted from MC are seen to grow with increasing significance.
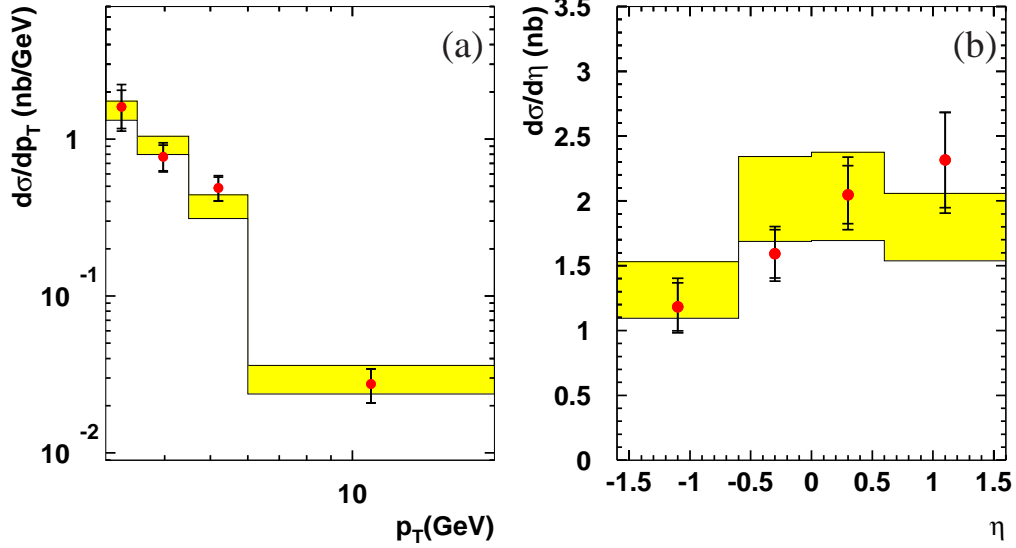
Figure 2.7: *Differential cross sections for (a) $D^{\pm}$ as a function of $p_T^{D^{\pm}}$ and (b) D^0 as a function of η^{D^0} (points) compared to the prediction of HVQDIS (shaded). The inner error bars show the statistical uncertainty and the outer bars show the statistical and systematic uncertainties added in quadrature.*

2.5 Selected results from the HERA experiments

2.5.1 D meson production cross sections

Both H1 and ZEUS have measured inclusive production cross sections of $D^{\pm}$, D^0, $D_s^{\pm}$ and $D^{*\pm}$ mesons in DIS [20, 23, 25]. Figure 2.7 shows inclusive cross sections measured at ZEUS for the transverse momentum of the $D^{\pm}$ meson, $p_T^{D^{\pm}}$, and pseudorapidity of the D^0 meson, η^{D^0}. Pseudorapidity is defined as

$$\eta = -\ln\left[\tan\left(\frac{\theta}{2}\right)\right], \qquad (2.2)$$

where θ is the angle of the particle trajectory relative to the proton beam direction. The NLO QCD predictions are found to describe the data well. Figure 2.8 shows the visible differential p_T^D, η^D and Q^2 production cross sections for four D mesons divided by their measured hadronisation fractions. The similarity in shapes
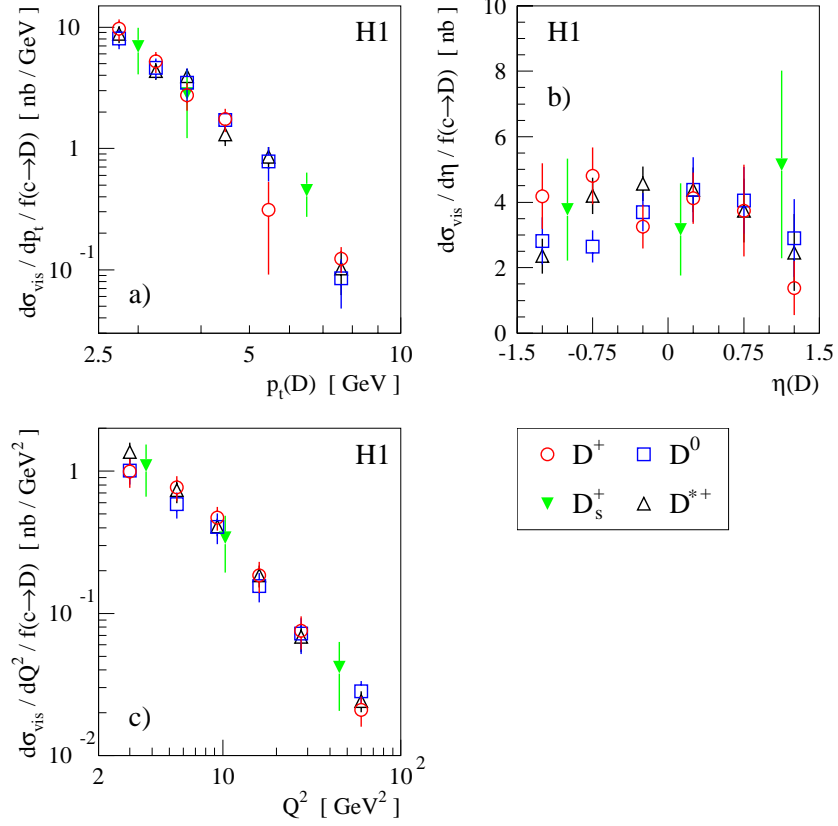
Figure 2.8: *Visible differential production cross sections for four D mesons, divided by their hadronisation fractions shown as a function of (a) transverse momentum of the D meson $p_t(D)$, (b) the pseudorapidity of the D meson, $\eta(D)$ and (c) the photon virtuality Q^2. The quadratic sum of the statistical and systematic uncertainties not common to the different mesons are shown by the error bars.*

between the D mesons demonstrates the compatibility with an event description in which the fragmentation of charm quarks is factorisable from the hard scatter.

2.5.2 Measurements of the open charm contribution, $F_2^{c\bar{c}}$, to the proton structure function F_2

In analogy with equation 1.9 the value of $F_2^{c\bar{c}}$ at $Q^2 \ll M_Z^2$ and low y is given by;

$$\frac{d\sigma^{c\bar{c}}(e^\pm p)}{dxdQ^2} = \frac{2\pi\alpha^2}{xQ^4} \left[1 + (1-y)^2 F_2^{c\bar{c}}\right] \tag{2.3}$$
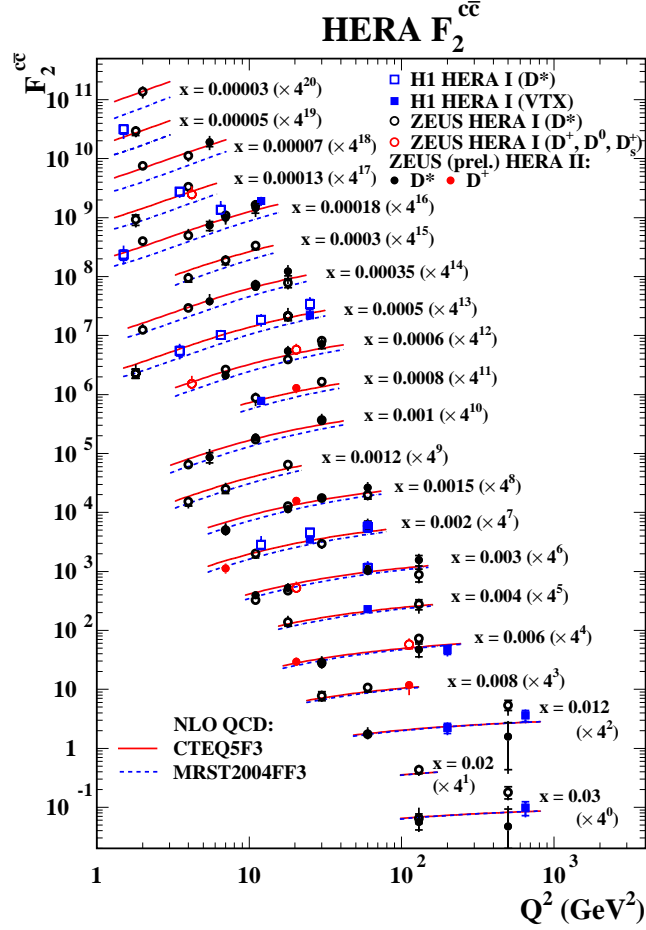
Figure 2.9: *Values of $F_2^{c\bar{c}}$ measured at different Q^2 and x values with various methods of charm tagging. The inner error bars show the statistical uncertainty while the outer error bars represent the statistical and systematic uncertainties added in quadrature.*

implying that by measurement of the double differential cross section of charm in Q^2 and x, $F_2^{c\bar{c}}$ can be extracted. Such extractions have been performed at HERA using all three charm tagging techniques outlined in section 2.4 [20, 25, 26]. As charm production at HERA occurs via BGF, any measurement of $F_2^{c\bar{c}}$ places direct constraints on the relatively poorly known gluon PDF. Figure 2.9 shows values of $F_2^{c\bar{c}}$ measured using the inclusive impact parameter technique along with other values extracted by tagging D mesons.

Chapter 3

HERA and the ZEUS detector

The Hadron-Elektron Ring Anlage (HERA) was located at the Deutches Elektronen Synchrotron (DESY) in Hamburg, Germany. The data analysed in this thesis was collected from the electron-proton collisions in the HERA ring using the ZEUS detector. This chapter details the experimental components most relevant to this thesis.

3.1   The HERA accelerator

HERA was the world's first, and to date only, electron-proton collider. Situated 10-20 m beneath the Volkspark area of Hamburg (figure 3.1), HERA had a circumference of 6.3 km. The accelerator began regular operation in May 1992 and continued until July 2007. The HERA ring itself was composed of two independent storage rings, one for protons and the other for electrons (or positrons). Interactions occurred in four straight sections, 360 m long, situated around the ring.
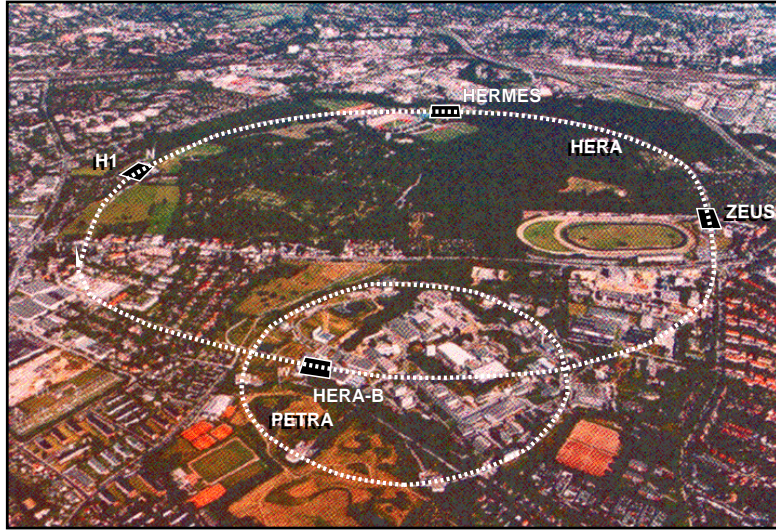
Figure 3.1: *The HERA collider and PETRA pre-accelerator in the Volkspark area of Hamburg.*

3.1.1 The HERA injection chain

The layout of HERA and the associated pre-accelerators is shown in figure 3.2. Electrons were first accelerated to 200 MeV in the linear accelerator before being transferred to the DESY II synchrotron and accelerated up to 7.5 GeV. From here they were passed to the PETRA ring where they were accelerated to 14 GeV before finally being injected into HERA and accelerated to 27.5 GeV. The electron ring in HERA used non-superconducting magnets and superconducting radio frequency cavities for the electron acceleration.

The proton injection chain began with H^- ions accelerated to 50 MeV in the proton linear accelerator. They were then transferred to DESY III and accelerated to 7.5 GeV. At this point the electrons were stripped off. The protons were then accelerated to 40 GeV in PETRA II before being injected into HERA and accelerated to 920 GeV. The proton ring in HERA used superconducting dipole and quadrupole magnets along with non-superconducting radio frequency cavities for the proton acceleration.
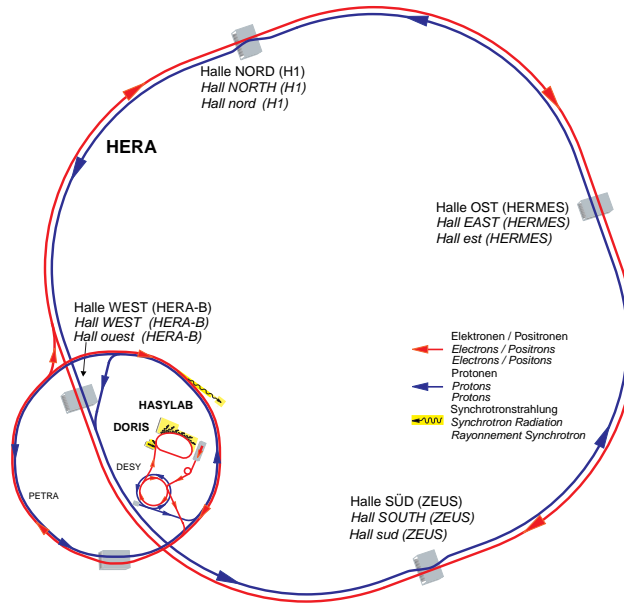
Figure 3.2: *Schematic of HERA and pre-accelerators.*

At the interaction regions surrounded by the ZEUS and H1 detectors the electron and proton beams collided at zero crossing angle. To achieve this the guiding magnets deflected the protons into the same vacuum pipe as the electrons before the protons were brought back into the proton ring after passing the interaction region.

3.2 The ZEUS detector

The ZEUS detector [27] was one of two multipurpose particle detectors designed to measure final state particles from ep collisions in the HERA storage ring, the other being the H1 detector. ZEUS provided near 4π solid angle coverage about the interaction region. The following section will detail the components of the ZEUS detector most relevant to the work contained in this thesis. Figure 3.3 shows a cutaway of the ZEUS detector with the components most relevant to this thesis
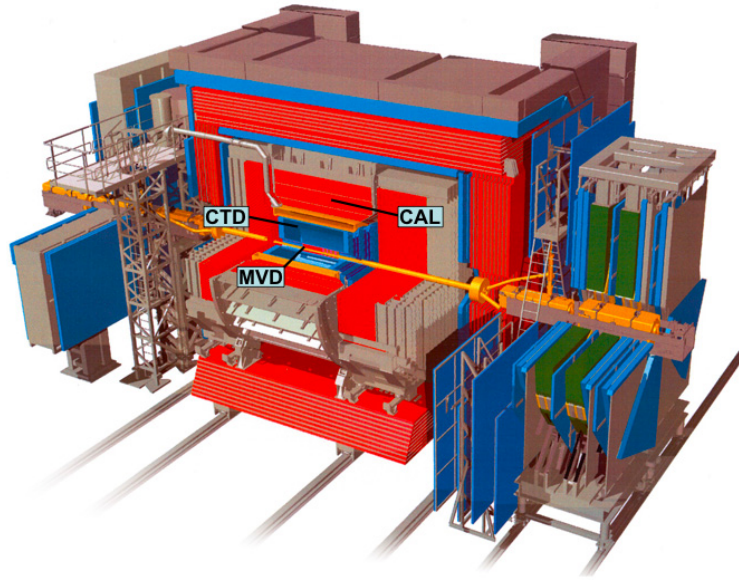
Figure 3.3: *Cutaway of the ZEUS detector showing the major components used in this thesis.*

highlighted[1].

3.2.1 The silicon micro vertex detector

The silicon micro vertex detector (MVD) [28] was separated into barrel (BMVD) and forward (FMVD) sections. The BMVD consisted of 600 square single-sided silicon-strip detectors arranged into three concentric cylindrical layers about the z axis[2] providing polar-angle coverage for tracks with three planes of information from $30°$ to $150°$. Sensors in the BMVD were paired into half-modules and

---

[1]The ZEUS coordinate system is a right-handed Cartesian system, with the z axis pointing in the proton beam direction, referred to as the "forward direction", and the x axis pointing towards the centre of HERA. The coordinate origin is at the nominal interaction point.

[2]Approximately 25% of the azimuthal angle was covered by only two layers due to limited space.
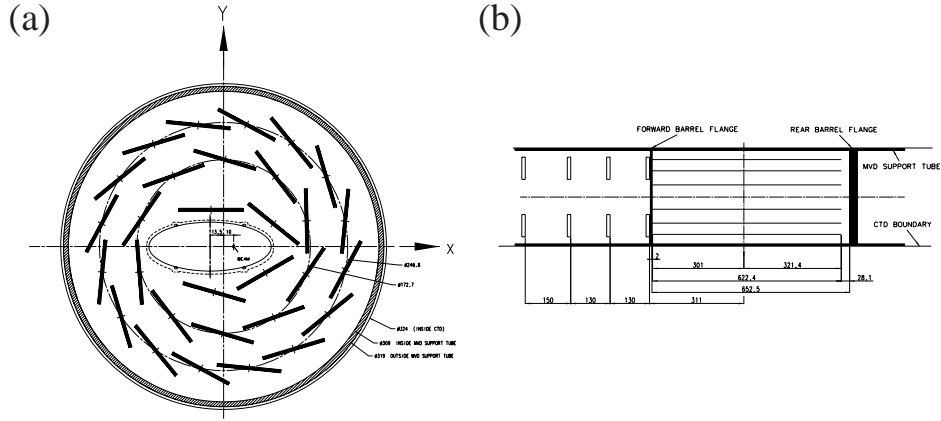
Figure 3.4: *(a) xy cross section of the BMVD and (b) yz cross section of the MVD*

oriented such that one provided $r\phi$ information and the other $z\phi$. The FMVD was composed of an additional 112 wedge-shaped detectors arranged in four vertical planes, which extended the polar-angle coverage in the forward region to $7°$. The barrel (forward) detectors consisted of 512 (418), 14 μm wide readout strips with a pitch of 120 μm. In addition there were 5 intermediate strips between each readout strip for capacitive charge division. During testbeam conditions a spatial resolution of 13 μm was measured for perpendicular tracks on a barrel half-module and tracks reconstructed with Kalman filter techniques in the CTD-BMVD system have been measured to have an impact parameter resolution of 100 μm in regions where three cylindrical layers are traversed. Figure 3.4 shows the layout of the MVD.

3.2.2 The central tracking detector

Charged particles which passed through the MVD were tracked in the central tracking detector (CTD) [29]. The CTD consisted of 72 cylindrical drift chamber layers organised into 9 superlayers (figure 3.5) covering the polar angle region
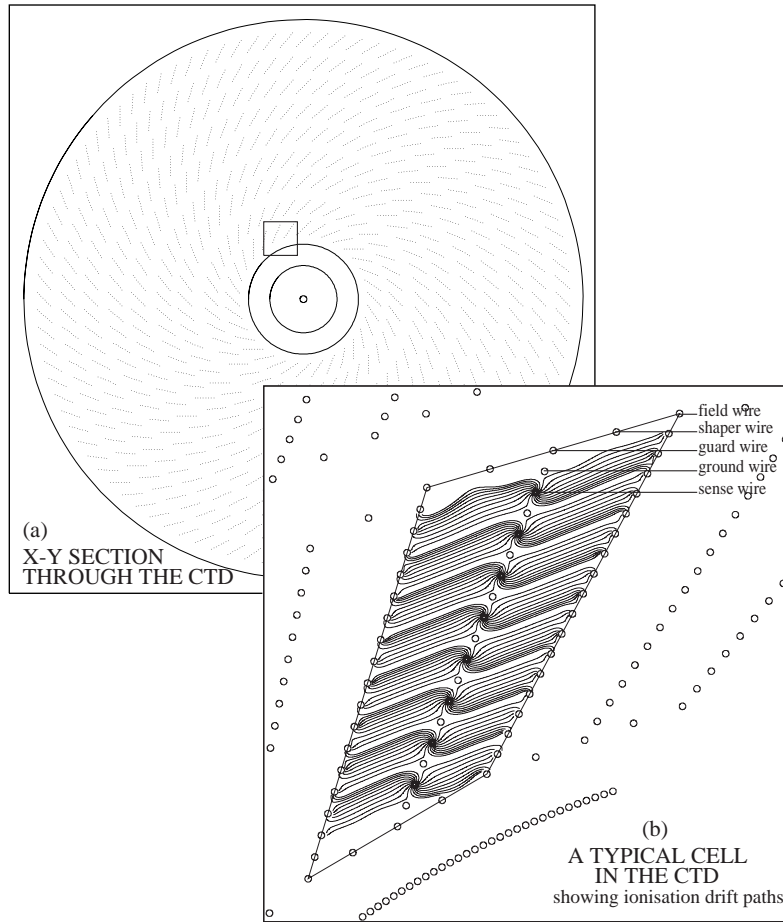
Figure 3.5: *(a) xy view through the CTD and (b) a typical cell layout.*

$15° < \theta < 164°$ and was filled with a mixture of argon, CO_2 and ethane bubbled through ethanol. Particle identification is possible using a measurement of the mean energy loss, $\frac{dE}{dx}$, of charged particles in the active volume. The transverse momentum resolution for tracks in the combined CTD-MVD system is discussed in chapter 5.

The odd-numbered (axial) superlayers contained drift wires which ran parallel to the z axis. The remaining even-numbered (stereo) superlayers contained wires which ran at a small stereo angle ($\pm 5°$) with respect to the z axis. This arrangement

of wires allowed accurate measurement of $r\phi$ and z coordinates. The position resolution for the CTD for tracks which pass through all 9 superlayers is $\sim 180~\mu$m in $r\phi$ and ~ 2 mm in z. The inner three superlayers of the CTD incorporated a z-by-timing system which provided a measurement of the z position of a hit. As the name implies this was achieved by measuring the difference in arrival time of a signal at opposite ends of the same wire. This method has a relatively coarse resolution of ~ 4 cm but has the advantage of being comparatively rapid and so was mainly used for triggering purposes.

3.2.3 The uranium calorimeter

Calorimetry at ZEUS used a high resolution uranium compensating calorimeter (CAL) covering 99.7% of the possible 4π solid angle. The CAL was split into three sections: forward (FCAL), barrel (BCAL) and rear (RCAL). A schematic of the CAL and its separate sections can be seen in figure 3.6. Each CAL section was further divided into towers consisting of both electromagnetic (EMC) and hadronic (HAC) cells. The layout of a barrel tower can be seen in figure 3.7. The dimensions of the front a CAL tower were 20 cm $\times$ 20 cm with the EMC section consisting of four 5 cm $\times$ 20 cm cells and the HAC section consisting of two 20 cm $\times$ 20 cm cells. Apart from their differing dimensions the EMC and HAC cells were identical in design; both had alternating layers of depleted uranium (3.3 mm of absorber) and plastic scintilator (2.6 mm of active material). Photons emitted in the active material of a cell were channelled via light guides and wavelength shifters positioned on each side of the cell to two photomultiplier tubes (PMT) at the rear of the tower. The differing signals from each PMT give positional information within the cell. The EMC sections had a depth of 1 interaction length and the combined HAC sections had depths of 6, 4 and 3 interaction lengths in the FCAL, BCAL and RCAL respectively.
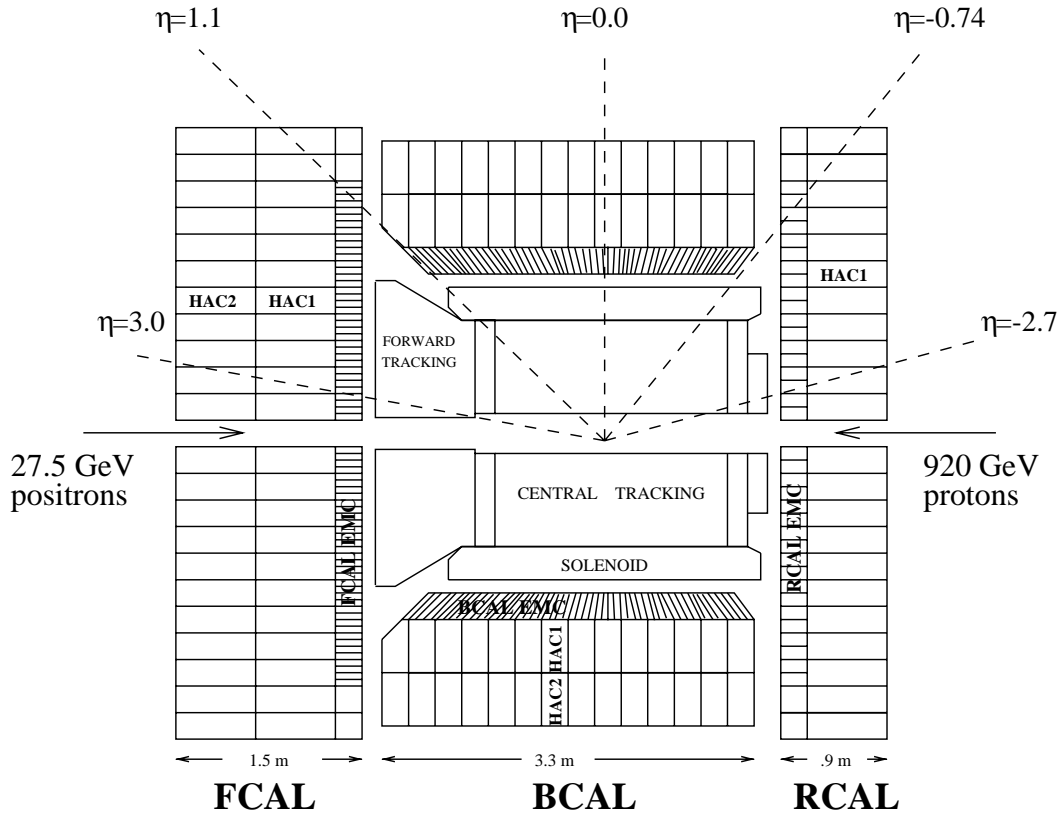
Figure 3.6: *Schematic of the ZEUS uranium calorimeter (xz plane).*

As mentioned the CAL was a compensating calorimeter meaning its response to both electromagnetic and hadronic showering was the same. Hadronic showers in a non-compensating calorimeter consist of fewer photons and more neutrons resulting in an unequal response from the active material. The depleted uranium absorber of the ZEUS CAL absorbs the neutrons of the hadronic shower and emits photons resulting in the same number of photons for hadronic and electromagnetic showers. The energy resolution of the CAL as measured under test beam conditions was $\frac{\sigma(E)}{E} = \frac{35\%}{\sqrt{E}}$ for hadrons and $\frac{\sigma(E)}{E} = \frac{18\%}{\sqrt{E}}$ for electrons [30, 31].
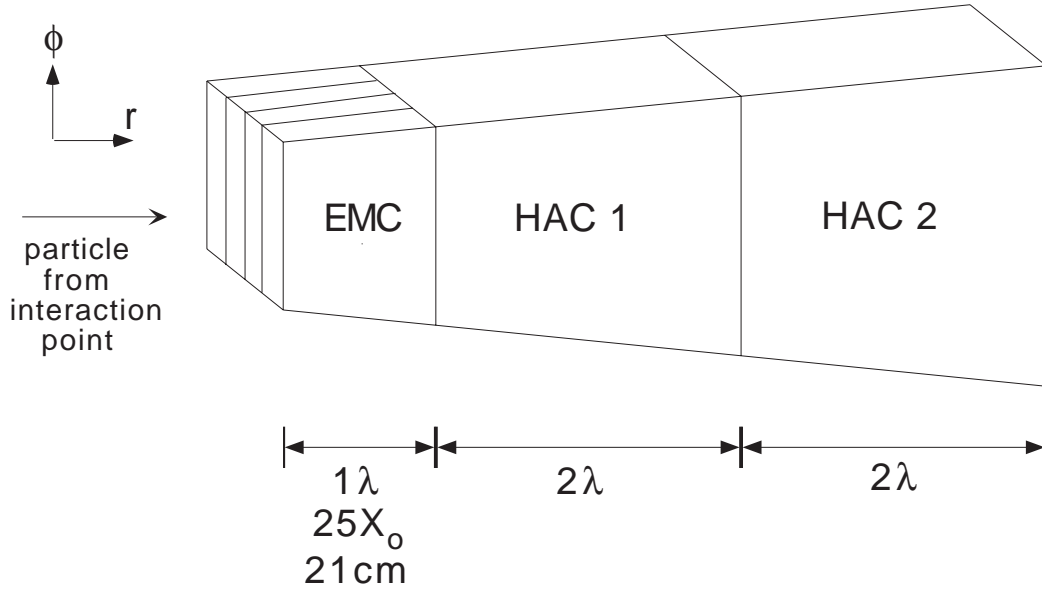
Figure 3.7: *Layout of a BCAL tower.*

3.2.4   The luminosity measurement

An accurate value of the luminosity ($\mathcal{L}$) is required for any cross section measurement. At ZEUS $\mathcal{L}$ was measured using the rate of the Bethe-Heitler process $ep \rightarrow e'p\gamma$ [32]. The cross section for this process at a fixed photon scattering angle (θ_γ) and energy (E_γ) is well known, meaning the luminosity can be extracted using the relation, $\mathcal{L} = \frac{N_\gamma}{\sigma_{\mathrm{BH}}}$ where N_γ is the number of measured photons and σ_{BH} is the calculated cross section for the process.

Two independent systems were used for the determination of $\mathcal{L}$ at ZEUS. In the first system the Bethe-Heitler photons were detected by a lead-scintillator calorimeter placed in the HERA tunnel 107 m from the interaction point in the electron beam direction (figure 3.8). This system was modified from its HERA I configuration [33] by the addition of active filters in order to suppress the increased synchrotron radiation background of the upgraded HERA collider. The second system was a magnetic spectrometer arrangement [34]. A small fraction
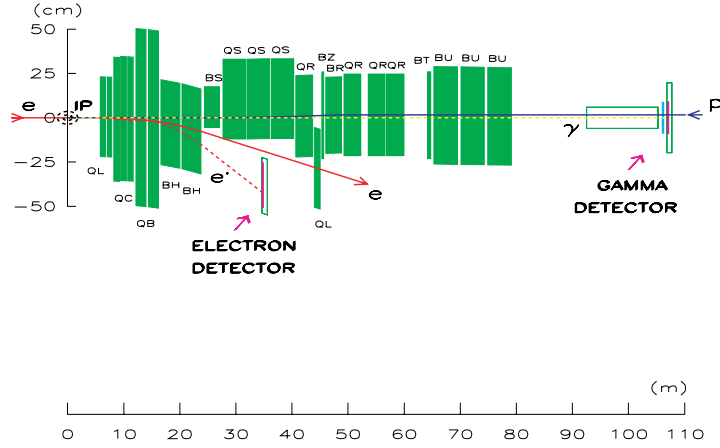
Figure 3.8: *Schematic of the ZEUS lead-scintillator calorimeter luminosity monitor. The nominal interaction point is at (0, 0).*

($\backsim 9\%$) of the small-angle energetic photons from the Bethe-Heitler process converted in the exit window of the vacuum chamber. Electron-positron pairs from the converted photons were bent vertically by a dipole magnet and detected in tungsten-scintillator calorimeters located above and below the photon beam at $z = -104$ m. A schematic of the spectrometer layout is shown in figure 3.9. The spectrometer system did not suffer from pile-up (multiple interactions at high luminosity) and was not sensitive to direct synchrotron radiation, whereas the calorimeter system had higher acceptance. The fractional systematic uncertainty on the measured luminosity is 2.6%.

Figure 3.10 shows the luminosity delivered by HERA and collected by ZEUS in the years 2002 - 2007 as measured by the luminosity monitor. The total ZEUS high energy data sample for this period is 406.7 pb^{-1}.
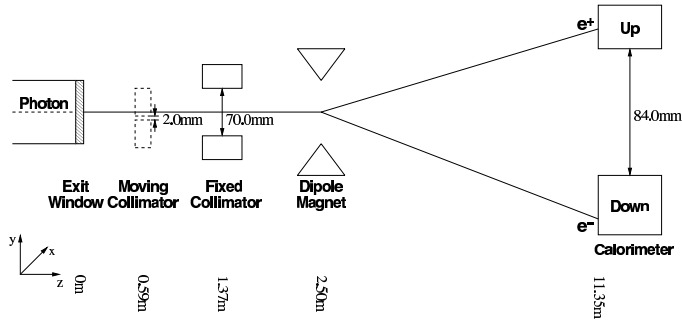
Figure 3.9: *Schematic of the luminosity spectrometer. Note that the exit window is $92.5\ m$ downstream from the nominal interaction point. All distances are shown relative to the centre of the exit window.*
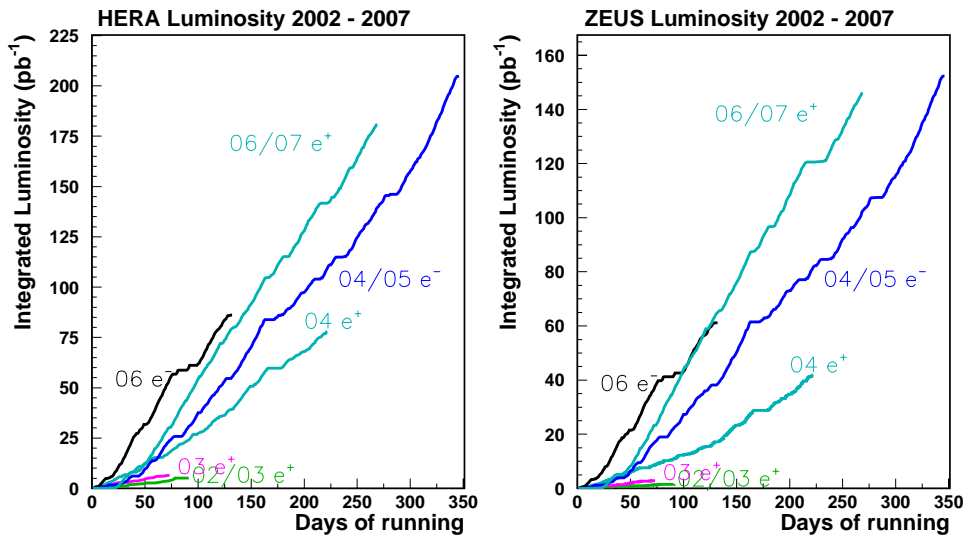
Figure 3.10: *Delivered and gated luminosity for the HERA II high energy running (HER) period 2002-2007.*
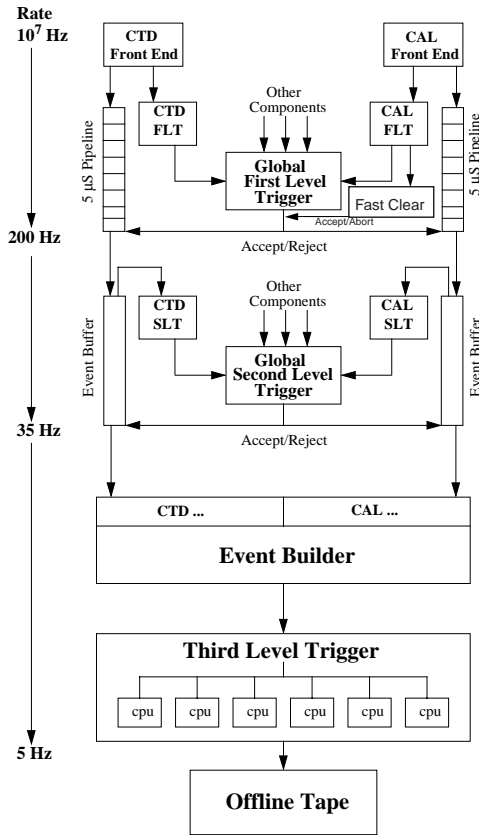
Figure 3.11: *The ZEUS trigger and DAQ system.*

3.2.5 The ZEUS trigger chain

Within the HERA collider a bunch crossing occurred every 96 ns leading to a nominal interaction rate in the ZEUS detector of ~ 10 MHz. This rate is dominated by proton beam interactions with residual gas in the beampipe (10 KHz - 100 KHz) and separating the interesting events from the background is challenging from a data acquisition (DAQ) and triggering point of view. The ZEUS detector incorporated a three level trigger [35, 36] to efficiently select interesting ep events whilst filtering background events.

The first level trigger (FLT) was hardware based and is designed to reduce the rate to ~ 1 KHz. Each component used in the FLT had its own FLT pipeline in

which data is stored awaiting the decision. These pipelines were deadtime free and were of both digital and analogue design depending on the component in question. Each component's decision on an event was passed to the global first level trigger (GFLT) in ~ 2 μm. The global decision was made in ~ 4.4 μm and propagated back to the individual components which passed the event information to the second level trigger (SLT) or cleared the pipeline accordingly. A typical FLT decision was based on the event timing, energy deposits in the CAL and a reasonable primary vertex position.

The SLT is analogous to the FLT in that each component passes on its individual decision to the global second level trigger (GSLT) before the global decision is passed back to the components which respond accordingly. Unlike the FLT the SLT is software based and runs on a network of transputers. The SLT contained triggers for specific event topologies for example leptonic heavy flavour decay and diffraction. After the SLT the rate is further reduced by a factor 10 to ~ 10 Hz and filtered events are passed to an event builder which formats the data ready for the third level trigger (TLT).

The TLT executed a fast version of the full offline reconstruction software in order to obtain the most detailed look yet at the overall event topology and characteristics. This was achieved using a powerful processor farm. Events which passed this final level of the trigger system were written to storage via optical cable at a rate ~ 1 Hz. The total decision time between the bunch crossing and the final event was ~ 0.3 s. A schematic of the ZEUS DAQ and trigger system is shown in figure 3.11.

Chapter 4

Alignment of the ZEUS barrel micro vertex detector

The ZEUS MVD, installed during the 9 month upgrade shutdown of HERA in 2000/2001, is described in detail in section 3 and elsewhere [28]. The aim of its installation was to give ZEUS the capability to tag heavy flavour decays by the reconstruction of displaced secondary vertices. In order for the MVD to be useful in highly resolution dependent analyses a precise knowledge of the sensor positions within the detector was necessary; to achieve this a four step alignment procedure was adopted. This consisted of survey measurements, a laser alignment system installed with the MVD, alignment with cosmic muon tracks and alignment with tracks from ep events. Of these four only the last will be discussed in detail as this was undertaken as part of this thesis.

4.1   Construction survey

This stage consisted of the precise placement of the sensors and ladders into the various support structures. During the construction, measurements were made at
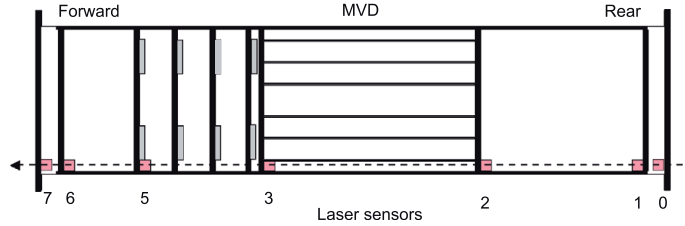
Figure 4.1: *Schematic diagram for one complete straightness monitor. Forward and rear refer to the orientation of the tracking detectors with forward being in the direction of the HERA proton beam.*

various times and the results are reported in [28]. The final precision of the sensor mounting was measured to be of the order 100 μm.

4.2 Laser alignment

The laser alignment system [37] contains four straightness monitors positioned around the perimeter of the MVD support tube. Each monitor consists of a collimated laser beam running parallel to the collider beamline and seven semi-transparent silicon sensors placed along its path. The system is sensitive to movements of the support structure perpendicular to the beamline. A schematic of the design can be seen in figure 4.1. Data collected from the laser alignment system provided evidence that the condition of the MVD may not be identical between luminosity and non-luminosity running and that local alignment could change by up to 100 μm. This led to the conclusion that tracks reconstructed under luminosity type circumstances should be used for the alignment of the MVD.

4.3 Alignment with cosmic muon tracks

The first use of data in the alignment of the MVD involved cosmic muon tracks [28, 38] which have an abundance of MVD measurements involved in

58
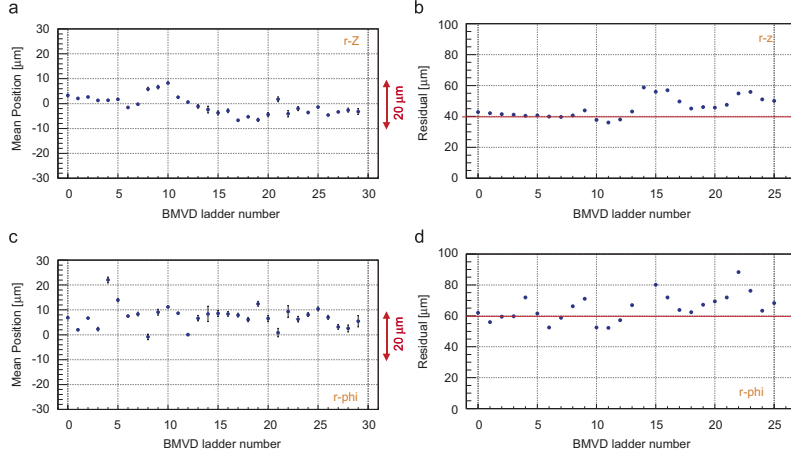
Figure 4.2: *Track residual, mean positions (a) and standard deviations (b) in $r\phi$ and mean positions (c) and standard deviations (d) in rz, after the cosmic alignment procedure [38].*

their reconstruction. Tracks produced in an ep collision will begin at the event vertex and as such can only expect to pass through three layers of the MVD. Cosmic muon tracks on the other hand pass through the entire detector and so are strongly constrained by MVD information. A two step iterative procedure based around a χ^2 minimisation of hit residuals was used to determine both the global displacement of the vertex detector in the ZEUS frame of reference and the internal alignment of sensor ladders relative to each other. A residual in this case is defined as the distance between the MVD cluster and the intersection of the track with the nominal sensor plane projected onto the measurement axis of the sensor. Each iteration of the procedure involved the removal of individual hits from tracks before refitting the track and obtaining a set of alignment constants for the sensor which contained the removed hit. Figure 4.2 shows track residual means and standard deviations for each ladder in the BMVD after the cosmic alignment. It can be seen that the residual distribution means are within about $\pm$ 10 μm of zero. The width of the distributions remains $\approx$ 50 μm, about twice the intrinsic resolution of the MVD. This could be attributed to several factors; the limited

59

number of cosmics available, the poor illumination of the BMVD side regions by cosmic tracks and the fact that the cosmic tracks used in the alignment were not collected during luminosity running conditions.

4.4 Alignment with ep tracks

To complement the cosmic muon alignment a procedure was developed to obtain alignment constants from tracks produced in ep collisions. These tracks intersect the forward and side-barrel regions at near perpendicular angles and hence provide far more aligning power than muon tracks in these regions.

4.4.1 The Millepede program package

The Millepede program package by Blobel [39] is a set of routines designed to perform a linear least squares fit on a specific type of problem. Such problems consist of a very large number of parameters which can be divided into global and local parameters, where local parameters are those which are present only in subsets of the data. In the context of the ep alignment of the MVD each track is described by its own set of track (local) parameters but all tracks will also depend on the alignment (global) parameters of the detector. Normally the direct solution to such a problem would involve the inversion of an enormous matrix with the time for a solution scaling with the cube of the number of parameters. In order to achieve the inversion in a reasonable time scale the Millepede package essentially splits the matrix into sub-matrices and inverts these before a recombination procedure is applied to obtain the final, optimal result for the global and local parameters. The data for a local fit (e.g a track) is transmitted to the routines one data point at a time. Each data point represents a hit residual defined as the difference between the expected hit position and the actual hit position projected
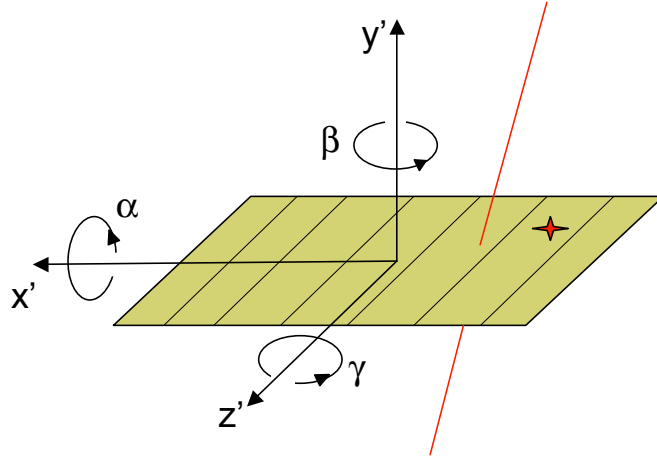
Figure 4.3: *Illustration of the five sensor alignment constants and their relation to the detector wafer.*

along the measurement axis of the sensor. The expectation value for a data point is given by:

$$z = \underbrace{a_1 \cdot d_1 + a_2 \cdot d_2 + \cdots a_n \cdot d_n}_{global\,parameters} + \underbrace{\alpha_1 \cdot \delta_1 + \alpha_2 \cdot \delta_2 + \cdots \alpha_\nu \cdot \delta_\nu}_{local\,parameters}$$

$$z = \sum_{i=1}^{n} a_i \cdot d_i + \sum_{j=1}^{\nu} \alpha_j \cdot \delta_j$$

(4.1)

The factors d_i and δ_j are the derivatives of the expectation value with respect to the coefficients a_i and α_j. Given the parametersation of tracks in ZEUS the coefficients α_j and a_i correspond to the track parameters and the geometry parameters of the BMVD respectively. For the BMVD five global parameters were defined for each sensor giving a total of 3000 alignment constants to be found. The parameters are illustrated in figure 4.3 and correspond to translations along the sensor's x and y axes and rotation about the three coordinate axes. No alignment constant is defined along the sensor z axis due to the strip nature of the detector.

61

4.4.2 The ZEUS parameterisation of tracks

The motion of a charged particle in a uniform magnetic field can be described by a helical track model [40]. Assuming that the ZEUS magnetic field is aligned in the z direction (figure 4.4) then we define the five track parameters: W, T, ϕ_0, D_0 and Z_0. These are illustrated in figure 4.5 and are defined as:

- $W = q/R$ where q is the track charge and R is its radius.

- $\tan \theta_{Dip}$, where $\theta_{Dip} = \theta - 90°$

- ϕ_0 is the direction of the track at the point of closest approach to the nominal interaction point projected on the xy plane

- D_0 is the distance from the origin to the point of closest approach to the nominal interaction point in the xy plane.

- Z_0 is the distance from the origin to the point of closest approach projected onto the z axis.

Given the above definitions the point of closest approach to the origin is given by

$$\vec{D}_0 = \begin{pmatrix} x_0 \\ y_0 \\ z_0 \end{pmatrix} = \begin{pmatrix} D_0 \sin \phi_0 \\ -D_0 \cos \phi_0 \\ Z_0 \end{pmatrix} \tag{4.2}$$

with the trajectory of the track described by

$$\begin{pmatrix} x \\ y \\ z \end{pmatrix} = \begin{pmatrix} D_0 \sin \phi_0 + \frac{1}{W} \cos \phi_0 \sin (W s_\perp) + \frac{1}{W} \sin \phi_0 [1 - \cos (W s_\perp)] \\ -D_0 \cos \phi_0 + \frac{1}{W} \sin \phi_0 \sin (W s_\perp) - \frac{1}{W} \cos \phi_0 [1 - \cos (W s_\perp)] \\ Z_0 + T s_\perp \end{pmatrix} \tag{4.3}$$

with $s_\perp = s \sin \theta$, and s defined as the distance along the trajectory from the point of closest approach.
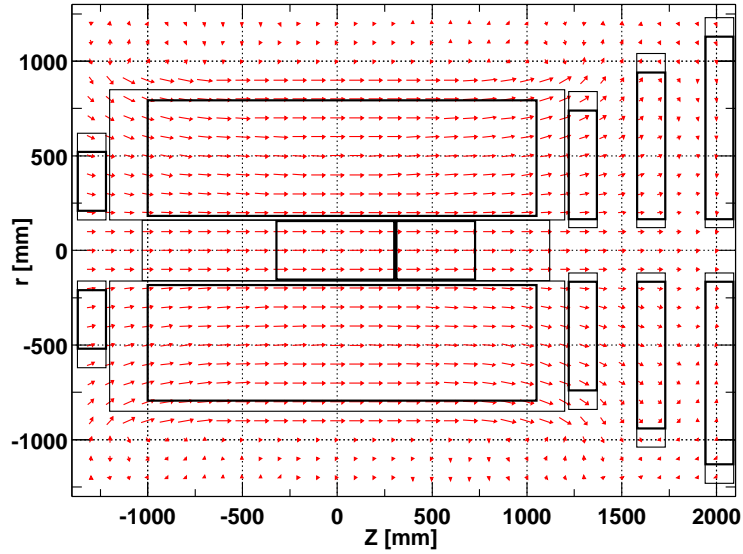
Figure 4.4: *The magnetic field in the ZEUS central detector. The length of the arrows shows the relative field strength in that region.*
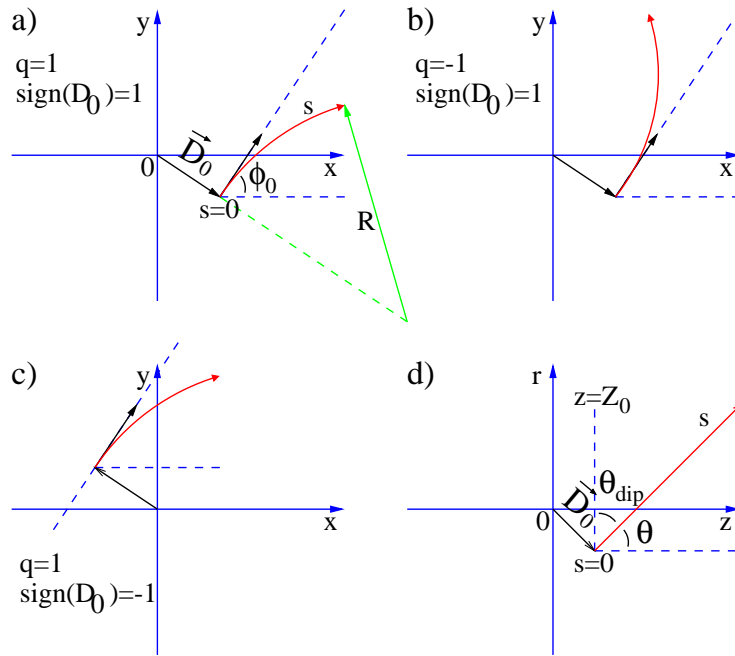
Figure 4.5: *A charged track in a uniform magnetic field projected on the xy and rz planes. (a) and (d) illustrate the track parameters where (b) and (c) are used to illustrate tracks with negative charge and negative D_0 respectively [40].*

4.4.3 Global and local coordinate frames

Just as there are global and local parameters there exists a definition of global and local coordinate frames [41]. For the purposes of the ep alignment of the ZEUS BMVD the global coordinate frame is that of the ZEUS coordinate system, a right handed cartesian with origin at the nominal interaction point, the z axis pointing in the direction of the proton beam and the x axis pointing toward the centre of HERA. This definition gives the unit vectors

$$\vec{e}_x = \begin{pmatrix} 1 \\ 0 \\ 0 \end{pmatrix}, \qquad \vec{e}_y = \begin{pmatrix} 0 \\ 1 \\ 0 \end{pmatrix}, \qquad \vec{e}_z = \begin{pmatrix} 0 \\ 0 \\ 1 \end{pmatrix} \qquad (4.4)$$

The local coordinate frame depends upon the track and hit in question and is defined by the nominal sensor plane in which a given hit lies, with origin at the centre of the sensor. The unit vectors are then given by the measurement direction of the sensor, $\vec{e}_x'$, the normal to the sensor plane, $\vec{e}_y'$, and the direction of the strips in the sensor, $\vec{e}_z'$.

Given these two coordinate frames it is possible to transform the intersection of a track with a sensor from one to the other using the relation

$$\vec{D} = R(\vec{r} - \vec{c}) \qquad (4.5)$$

where $\vec{D}$ is the intersection in the local frame, $\vec{r}$ is the intersection in the global frame, $\vec{c}$ is the origin of the sensor in question and R is the rotation matrix

$$R = \left(\vec{e}_x', \vec{e}_y', \vec{e}_z' \right) \qquad (4.6)$$

4.4.4 Track parameter derivatives

Given the definitions

$$\vec{b} = \begin{pmatrix} \cos\phi_0 \cos(Ws_\perp) + \sin\phi_0 \sin(Ws_\perp) \\ \sin\phi_0 \cos(Ws_\perp) - \cos\phi_0 \sin(Ws_\perp) \\ T \end{pmatrix} \tag{4.7}$$

$$\vec{a}_W = \begin{pmatrix} -\frac{1}{W^2}\left(\cos\phi_0 \sin(Ws_\perp) + \sin\phi_0 \left[1 - \cos(Ws_\perp)\right]\right) + \frac{s_\perp}{W} b_x \\ -\frac{1}{W^2}\left(\sin\phi_0 \sin(Ws_\perp) - \cos\phi_0 \left[1 - \cos(Ws_\perp)\right]\right) + \frac{s_\perp}{W} b_y \\ 0 \end{pmatrix} \tag{4.8}$$

$$\vec{a}_T = \begin{pmatrix} 0 \\ 0 \\ s_\perp \end{pmatrix} \tag{4.9}$$

$$\vec{a}_{\phi_0} = \begin{pmatrix} D_0 \cos\phi_0 - \frac{1}{W}\left(\sin\phi_0 \sin(Ws_\perp) - \cos\phi_0 \left[1 - \cos(Ws_\perp)\right]\right) \\ D_0 \sin\phi_0 + \frac{1}{W}\left(\cos\phi_0 \sin(Ws_\perp) + \sin\phi_0 \left[1 - \cos(Ws_\perp)\right]\right) \\ 0 \end{pmatrix} \tag{4.10}$$

$$\vec{a}_{D_0} = \begin{pmatrix} 0 \\ 0 \\ 1 \end{pmatrix} \tag{4.11}$$

the derivatives of track intersection $\vec{r}$ with respect to the track parameters can be written in the form:

$$\frac{\partial \vec{r}}{\partial \alpha_i} = \vec{a}_i + \frac{\partial s_\perp}{\partial \alpha_i} \vec{b} \tag{4.12}$$

where $\alpha_i = W$, T, ϕ_0, D_0 and Z_0 and the second term ensures that the derivative remains in the supposed plane of the sensor. The values for $\frac{\partial s_\perp}{\partial \alpha_i}$ can be calculated using the constraint

65

$$\frac{\partial D_y}{\partial \alpha_i} = \vec{e}'_y \cdot \frac{\partial \vec{D}}{\partial \alpha_i} = \vec{e}'_y \cdot R \frac{\partial \vec{r}}{\partial \alpha_i} = 0 \qquad (4.13)$$

$$\implies \frac{\partial s_\perp}{\partial \alpha_i} = -\frac{\vec{e}'_y \cdot R\vec{a}_i}{\vec{e}'_y \cdot R\vec{b}} \qquad (4.14)$$

Given the nature of a single BMVD sensor the measurement of an intersection point is defined in the $\vec{e}'_x$ direction only. This gives the derivatives of the sensor measurement with respect to the track variables as

$$\delta_{\alpha_i} = \frac{\partial D_x}{\partial \alpha_i} = \vec{e}'_x \cdot \frac{\partial \vec{D}}{\partial \alpha_i} = \vec{e}'_x \cdot R \frac{\partial \vec{r}}{\partial \alpha_i} = \vec{e}'_x \cdot \left(R\vec{a}_i - R\vec{b}\frac{\vec{e}'_y \cdot R\vec{a}_i}{\vec{e}'_y \cdot R\vec{b}} \right) \qquad (4.15)$$

The impact of the track parameters on the expected measurement for a given MVD sensor is then

$$\delta D_x = \delta_W \cdot \Delta W + \delta_T \cdot \Delta T + \delta_{\phi_0} \cdot \Delta \phi_0 + \delta_{D_0} \cdot \Delta D_0 + \delta_{Z_0} \cdot \Delta Z_0 \qquad (4.16)$$

where the δ signifies that it is the difference between the initial track parameters and those in the aligned MVD. This is a linear equation in direct correspondence to the local parameters from eq. 4.1.

4.4.5   Alignment parameter derivatives

In order to use millipede we must not only know the derivatives of the measurements with respect to the local track parameters but also with respect to the global alignment constants. The intersection vector of the trajectory with the supposed sensor plane is given by:

$$\vec{D}_0 = \begin{pmatrix} D_{x_0} \\ 0 \\ D_{z_0} \end{pmatrix} \qquad (4.17)$$

with $D_{y0} = 0$ by definition at the intersection point. Upon application of the local alignment the intersection point will change. This can be expanded as:

$$\vec{D}(\lambda) = \vec{D}_0 + \lambda \vec{t} \tag{4.18}$$

Using the constraint that $\vec{e}_y' \cdot \vec{D}'(\lambda_s) = 0$ we get:

$$\vec{e}_y' \vec{D}'(\lambda_s) = \vec{e}_y' \left[\left(\vec{D}_0 - \vec{c} \right) + \lambda_s R \vec{t} \right] \tag{4.19}$$

$$\lambda_s = -\frac{\vec{e}_y'(\vec{D}_0 - \vec{c})}{\vec{e}_y' R \vec{t}} \tag{4.20}$$

This leads to an expectation value for the measurement of

$$D_{x0}' = \vec{e}_x' \left[R(\vec{D}_0 - \vec{c}) - \frac{\vec{e}_y' R(\vec{D}_0 - \vec{c})}{\vec{e}_y' R \vec{t}} R \vec{t} \right] \tag{4.21}$$

Here the unit vectors are in the rotated coordinate system, hence $\vec{e}_x' = (1, 0, 0)^T$ and $\vec{e}_y' = (0, 1, 0)^T$. The rotation matrix can be parameterised by 3 small angles α, β and γ which describe small rotations about x, y and z axes respectively. It is assumed that these angles are small and that the approximations $\sin \alpha \approx \alpha$ and $\cos \alpha \approx 1$ are valid. In the case of small angles iteration is not required as higher orders can be ignored and we obtain a symmetric expression:

$$R = \begin{pmatrix} 1 & \gamma & \beta \\ -\gamma & 1 & \alpha \\ -\beta & -\alpha & 1 \end{pmatrix} \tag{4.22}$$

If eq. 4.21 is differentiated with respect to the global parameters $C_x, C_y, C_z, \alpha, \beta$ and γ at $\vec{c} = 0$ and $R = 1$ the following expressions are obtained.

$$\frac{\partial \vec{D}_x'}{\partial C_x} = -1 \tag{4.23}$$

$$\frac{\partial \vec{D}_x'}{\partial C_y} = \frac{t_x}{t_y} \tag{4.24}$$

67

$$\frac{\partial \vec{D}_x{}'}{\partial C_z} = 0 \tag{4.25}$$

$$\frac{\partial \vec{D}_x{}'}{\partial \alpha} = -\frac{t_x}{t_y} D_{z0} \tag{4.26}$$

$$\frac{\partial \vec{D}_x{}'}{\partial \beta} = D_{z0} \tag{4.27}$$

$$\frac{\partial \vec{D}_x{}'}{\partial \gamma} = \frac{t_x}{t_y} D_{x0} \tag{4.28}$$

The impact of our alignment parameters on the expected measurement for a given MVD sensor is then

$$\delta D_x = -1 \cdot C_x + \frac{t_x}{t_y} \cdot C_y - \frac{t_x}{t_y} D_{z0} \cdot \alpha + D_{z0} \cdot \beta + \frac{t_x}{t_y} D_{x0} \cdot \gamma \tag{4.29}$$

This is a linear equation in direct correspondence to the global parameters from eq. 4.1.

4.4.6 Additional track infomation

In addition to measurements from the MVD sensors themselves information from the CTD and the precisely known position of the elliptical interaction region in the xy plane, or beam spot, can be used in the Millepede fit. A full discussion of the beam spot can be found in section 5.3.5.

Track information from the central tracking detector

By using the CTD, measurements of the track parameters can be obtained which are independent of the MVD. In this case the differences between the parameters in the CTD only determination of the track and those obtained from the MVD and CTD combined are used as the expected measurements. For such data points all

global terms in eq. 4.1 disappear and the local derivatives are all zero except that corresponding to the parameter being measured which is set to unity. The main benefit of this additional information is to constrain the track parameters to remain within the window given by the CTD resolution. This prevents any large scale shifting of the MVD with respect to the CTD.

Beam spot information

The beam spot is another source that can provide information for the alignment. The beam spot is an accurate measurement of the position of the interaction point determined by combining a large number of reconstructed primary vertices (section 5.3.5). This can be used to stabilise the track in the transverse plane. With appropriate event selection to reduce background the impact parameter with respect to the beam spot provides another data point. The impact parameter is given by

$$D_{\text{bsp}} = \sqrt{(x_{\text{bsp}} - x_c)^2 + ((y_{\text{bsp}} - y_c)^2} - |QR| \qquad (4.30)$$

where x_{bsp} and y_{bsp} are the beam spot position and the coordinates of the helix centre, x_c and y_c, are defined as

$$x_c = QD_H \sin \phi_H \qquad (4.31)$$

$$y_c = -QD_H \cos \phi_H \qquad (4.32)$$

The sign convention for D_{bsp} is such that it is positive when the beam spot lies outside of the circle projected from the helix. The derivatives of the impact parameter with respect to the relevant track parameters are

$$\frac{\partial D_{\text{bsp}}}{\partial D_H} = \frac{(x_c - x_{\text{bsp}}) \sin \phi_H - (y_c - y_{\text{bsp}}) \cos \phi_H}{\sqrt{(x_c - x_{\text{bsp}})^2 + (y_c - y_{\text{bsp}})^2}} \qquad (4.33)$$

$$\frac{\partial D_{\text{bsp}}}{\partial Q/R} = (QR)^2 \frac{(x_c - x_{\text{bsp}}) \sin \phi_H + (y_c - y_{\text{bsp}}) \cos \phi_H}{\sqrt{(x_c - x_{\text{bsp}})^2 + (y_c - y_{\text{bsp}})^2}} + Q \qquad (4.34)$$

$$\frac{\partial D_{\text{bsp}}}{\partial \phi_H} = \frac{(QD_H + QR)\left[(x_c - x_{\text{bsp}}) \cos \phi_H + (y_c - y_{\text{bsp}}) \sin \phi_H\right]}{\sqrt{(x_c - x_{\text{bsp}})^2 + (y_c - y_{\text{bsp}})^2}} \qquad (4.35)$$

The known value of the beam spot can be treated as a measurement of the impact parameter whose value is zero, and whose error is

$$\sigma_D = \sqrt{(\sigma_x \cos \phi_{\text{bsp}})^2 + (\sigma_y \sin \phi_{\text{bsp}})^2} \qquad (4.36)$$

Here ϕ_{bsp} is the track direction in the transverse plane at the point of closest approach to the beam spot according to

$$\tan \phi_{\text{bsp}} = -\frac{x_{\text{bsp}} - x_c}{y_{\text{bsp}} - y_c} \qquad (4.37)$$

and σ_x and σ_y are the width parameters of the beam spot. The beam spot residual is then zero minus the impact parameter expectation from the track parameters.

4.5   Track selection

Approximately 0.8 million tracks from the 2005 data set which passed the following cuts were used for the initial ep alignment of the BMVD:

- The z position of the reconstructed primary vertex must be within 20 cm of the nominal interaction point;

- The position of the reconstructed primary vertex must be within 1.2 cm of the beam spot in the xy plane;

- Tracks must be fitted to the primary vertex;
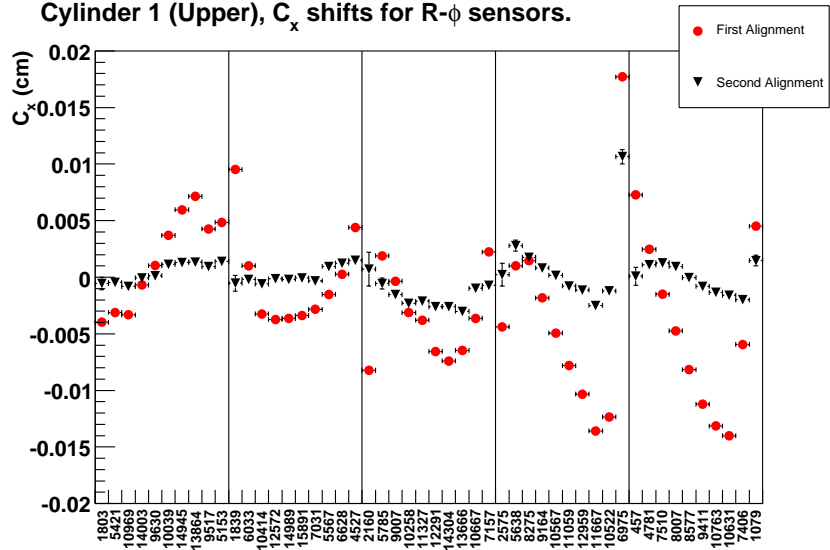
Figure 4.6: *Alignment constants describing the offset in the measurement direction for the $r\phi$ sensors on 5 ladders in the upper half of the middle cylinder. The circles represent the constants determined by the ep alignment as applied after cosmic alignment. The numbers on the x axis represent the number of tracks used to determine the constants. The black triangles represent the results of a second pass of the ep alignment.*

- Track momentum, p, must be greater than 2 GeV;

- The track should have at least 2 $r\phi$ and 2 $z\phi$ associated hits in the BMVD;

- The transverse momentum, p_T, must be greater than 1 GeV;

- The track must reach at least superlayer 5 in the CTD.

All tracks were reconstructed using the a Kalman Filter program (section 5.3.1).

4.6   Results of the alignment

4.6.1   Correlations of alignment constants

It is expected that the MVD ladders are rigid and that the sensors themselves are precisely mounted on these ladders. Thus we would expect the alignment

71
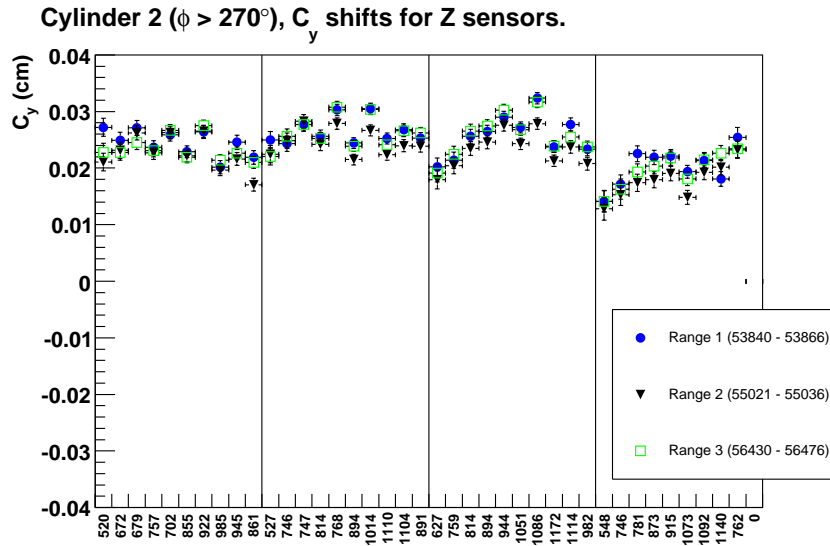
Figure 4.7: *Alignment constants describing the offset in the direction normal to the sensor plane for $z\phi$ sensors on 4 ladders in the $\phi > 270°$ region of the outer cylinder. Constants extracted from 3 independent track samples obtained at different times during 2005 running are shown. The numbers on the x axis represent the number of tracks used to determine the constants for the first run range only.*

parameters to be correlated between sensors on the same ladder. These correlations would most easily be seen in the translational alignment parameters C_x and C_y. Such correlations can be seen in figure 4.6 which shows the C_x constants for $r\phi$ sensors on five ladders in the upper half of cylinder 1. The alignment results of a second ep alignment pass are also shown for comparison and found to be much smaller indicating the success of the first pass and consistency of the alignment procedure.

4.6.2 Time dependence

In order to investigate the possibility of time dependent alignment constants the procedure was performed using track samples from three distinct periods of the 2005 data set. Figure 4.7 shows the C_y constants obtained from these track samples
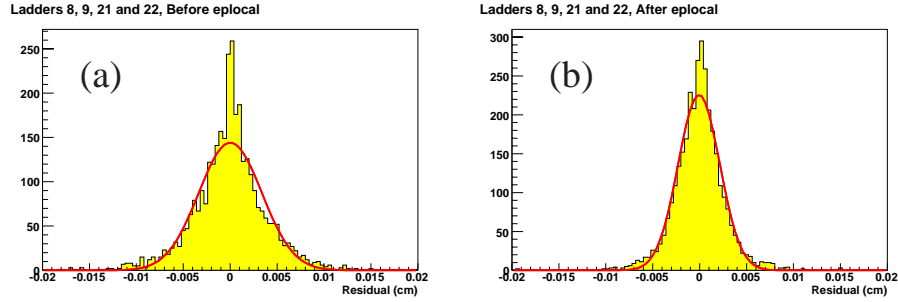
Figure 4.8: *Residual distributions for 80 sensors mounted on 4 ladders about the $\phi = 180^\circ$ region. (a) shows the distribution after cosmic but before ep alignment and (b) shows the distribution after both alignments have been applied.*

for $z\phi$ sensors on four ladders found in the $\phi > 270°$ region of the outer BMVD layer. It can be seen that the constants are consistent between samples and as such that the alignment of the BMVD is stable with respect to time during luminosity running.

4.6.3 Sensor residual distributions

It is expected that a well aligned sensor will have a narrow Gaussian residual distribution centred about zero. Figure 4.8 shows residual distributions from 4 complete ladders, containing 40 $r\phi$ sensors, located in the region about $\theta = 180°$ after (a) cosmic alignment and (b) ep alignment . Due to their orientation and position on the side of the BMVD the hit residuals of ladders in this region would be expected to benefit from the alignment with ep tracks. The width of a Gaussian function fitted to the residual distribution decreases from 34 μm before ep alignment to 22 μm afterwards indicating improved knowledge of the sensor positions.

73
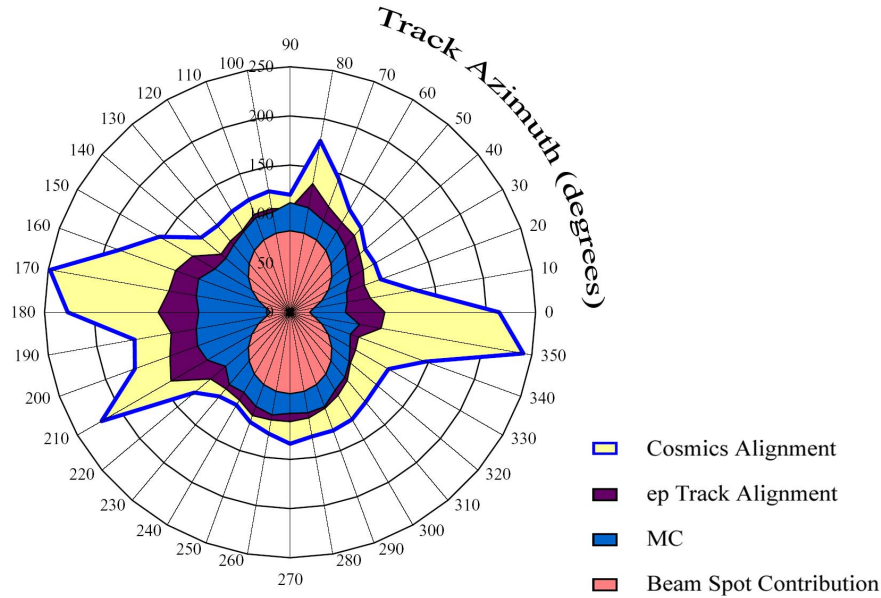
Figure 4.9: *The impact parameter resolution (µm) in regions of the azimuthal angle φ at different stages in the alignment procedure compared to the Monte Carlo prediction.*

4.6.4 Impact parameter resolution

A variable of direct interest to heavy quark analyses is the impact parameter (IP); this is defined as the distance of closest approach of a track to the primary interaction point. The variation of the impact parameter resolution, σ_{IP}, in different ϕ regions can provide information about the alignment of the MVD. Figure 4.9 shows σ_{IP} after cosmic and ep alignment compared to MC which by design has perfect alignment. After the cosmic alignment σ_{IP} is seen to be good in the vertical regions of ϕ but, as expected, still poor around the $\phi = 0°$ and $180°$ regions. Once the corrections from the ep alignment have been applied σ_{IP} lies closer to the MC prediction in all regions but the improvement is most pronounced in the previously poor $\phi = 0°$ and $180°$ areas. The remaining discrepancy between the data and MC can be ascribed to the presence of non-functioning portions of the MVD which at the time of the study were not simulated in the MC.

74
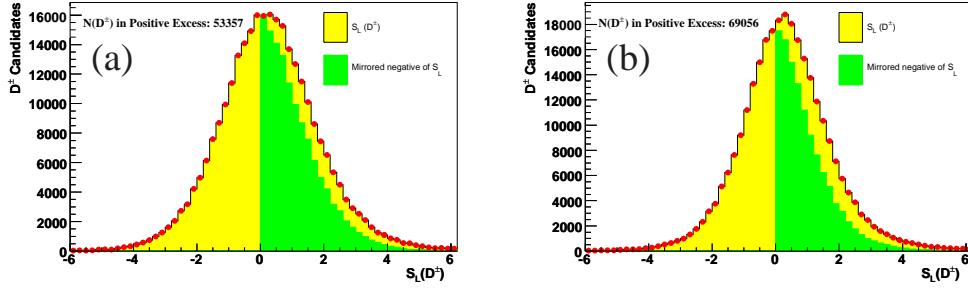
Figure 4.10: *The decay length significance distribution of $D^{\pm}$ data candidates before and after ep alignment corrections are applied to the BMVD. The number of candidates in the positive excess increases by $\smile 30\%$ indicating the improved background rejection power of this variable.*

4.6.5 D mesons and decay length significance

The main purpose of the MVD is to enable identification of heavy meson decays by their long lifetimes. The decay length significance, σ_l, is defined as the distance between the primary vertex and the decay vertex divided by the error on this distance and can be a powerful tool for background rejection. The rejection power of σ_l was improved after the alignment procedure. This is seen in figure 4.10 which shows an increase in the positive significance excess for reconstructed $D^{\pm}$ mesons.

4.7 Summary

In this chapter the different stages of the BMVD alignment were detailed with special focus on the alignment with ep tracks. The mathematics underlying the alignment procedure were detailed along with the Millepede program used for production of the alignment constants. Results were shown from real physics events to show the effectiveness of the procedure and the improved condition of the BMVD after the alignment.

Chapter 5

Event reconstruction and selection

This chapter will deal with the reconstruction and selection of DIS events and the $D^{\pm}$ and D^0 candidates used for production cross section measurements and the extraction of the open charm contribution, $F_2^{c\bar{c}}$, to the proton structure function, F_2.

5.1   Trigger selection

The DIS events used for the analyses were selected by requiring particular triggers to have been fired at the first, second and third levels of the ZEUS trigger system. At the third level one of two inclusive DIS slots was required to have been fired; each of these triggers implicitly requires the firing of triggers at the SLT and by extension the FLT. The logic of the two TLT slots is given below.

Slot 1 (SPP02)

- Significant calorimeter energy deposits and $\sum E - p_z > 30$ GeV at SLT;

- $30 < E - p_z < 100$ GeV;

- $E_{e'} > 4\,\text{GeV}$, where $E_{e'}$ is the scattered electron energy;

- Impact point (x, y), of the scattered electron on the surface of the RCAL must lie outside the region (12 cm, 12 cm) centred on (0, 0).

Slot 2 (HFL02)

- Heavy flavour meson candidate reconstructed at third level trigger;

- $E - p_z > 30\,\text{GeV}$;

- $E_{e'} > 4\,\text{GeV}$, where $E_{e'}$ is the scattered electron energy;

- Impact point (x, y), of the scattered electron on the surface of the RCAL must lie outside the region (12 cm, 12 cm) centred on (0, 0).

These two TLT slots involve a total of twenty three triggers at the FLT. Of these, eleven have some form of track requirement with the other twelve using calorimeter quantities only. These triggers provide a good overlap with little reliance on individual trigger slots; this is shown by the highest unique trigger rate being 3.5% (FLT30). If the FLT slots are separated into those with and without tracking requirements we find that the unique trigger rates for the two groups are 0.5% and 10% respectively.

5.2 Reconstruction of kinematic variables

A DIS event is characterised by any two of the Lorentz invariant variables defined in section 1. These variables are reconstructed at ZEUS using a combination of the scattered electron energy, $E_{e'}$, its polar angle, θ_e, and the longitudinal and transverse momentum of the hadronic final state. Several different methods exist for the calculation of the kinematic variables each one using a different
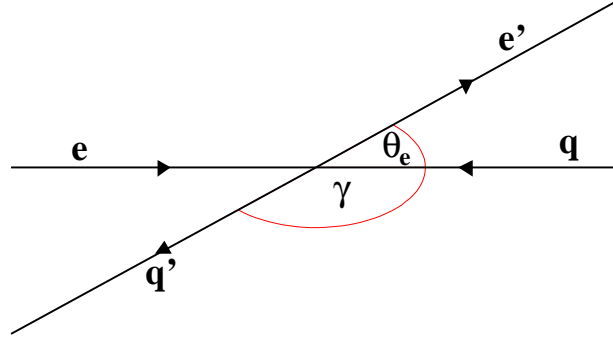
Figure 5.1: *Illustration of the electron and hadronic scattering angles θ_e and γ in relation to the electron proton beamlines. The direction of the quark, q, is approximate to the proton direction.*

combination of the above. The three methods described below were used in the D meson analyses, with one used as the main method of reconstruction for the kinematic variables and the other two used for cleaning cuts.

5.2.1 The electron method

As its name implies the electron (el) method uses information from the scattered electron to reconstruct the required variables and so implicitly requires excellent identification and measurement of the scattered electron. This method is sensitive to initial and final state radiation as it assumes that the energy of the incoming electron is that of the beam and that the scattered electron did not radiate between its emission of the virtual photon in the hard scatter and its detection. In the electron method y and Q^2 are given by

$$y_{\mathrm{el}} \;=\; 1 - \frac{E_{e'}}{2E_e}\left(1 - \cos\theta_e\right) \tag{5.1}$$

$$Q^2_{\mathrm{el}} \;=\; 2E_e E'_e \left(1 + \cos\theta_e\right) \tag{5.2}$$

78

where the polar angle, θ_e, is defined as the angle between the scattered electron and the z axis (figure 5.1). The electron method is used in the D meson analyses to reject fake electrons from photoproduction. Such fake signals are caused by hadronic activity and result in a high y_{el} value and so a cut of $y_{\text{el}} < 0.95$ is imposed.

5.2.2 The Jacquet-Blondel method

The Jacquet-Blondel (JB) method [42] is the hadronic analogue to the electron method. However, as it is impossible to directly measure the angle and energy of the scattered quark the variable is reconstructed using the entire hadronic final state. In the D meson analyses only y_{JB} is used:

$$y_{\text{JB}} = \frac{\sum_i (E_i - p_{z,i})}{2E_e} \tag{5.3}$$

The sum runs over all hadronic activity in the calorimeter cells; the scattered electron is removed from the sum. This reconstruction method is sensitive to the hadronic energy scale and requires that the hadronic activity of the event is fully contained and measured. In the D meson analyses a cut on $y_{\text{JB}} > 0.02$ is imposed to reject events with insufficient hadronic activity to be properly reconstructed with the double angle method.

5.2.3 The double angle method

Appropriate to its name the double angle (DA) method uses both the scattering angle of the electron and the hadronic angle, γ, an estimator of the scattering angle of the struck quark. In the DA method y and Q^2 are given by

$$y_{\text{DA}} = \frac{\tan \gamma/2}{\tan \gamma/2 + \tan \theta_e/2} \tag{5.4}$$

$$Q^2_{\text{DA}} = 4E_e^2 \frac{\cot \theta_e/2}{\tan \gamma/2 + \tan \theta_e/2} \tag{5.5}$$

with γ defined by

$$\cos\gamma = \frac{\sum_i p_{\perp,i}^2 - \sum_i (E_i - p_{z,i})^2}{\sum_i p_{\perp,i}^2 + \sum_i (E_i - p_{z,i})^2} \qquad (5.6)$$

Once again the sum runs over the hadronic deposits in the calorimeter. The DA method is used to reconstruct the variables which define the kinematic region in which D meson production is measured. This method was chosen as it has superior resolution over the kinematic region and is less sensitive to energy scales and radiative corrections than the other methods [43].

5.3 Track and vertex reconstruction

Several tools and methods exist for tracking at ZEUS. Those relevant to the analyses detailed in this thesis will now be described.

5.3.1 Track reconstruction

The offline track reconstruction is performed in two distinct stages. The first stage, pattern recognition, is carried out by the VCTRACK package [44]. This consists of a multi-pass algorithm which combines information from the tracking detectors in order to produce initial trajectories. These trajectories can then be used to find additional compatible hits. In the first passes only tracks with good CTD and MVD constraints are recognised before CTD-only and MVD-only tracks are found later in the procedure. This has the effect of extending the acceptance beyond that of the CTD alone.

After the pattern recognition, information assigned to a track by VCTRACK is then passed to the Kalman filter based track fitting package known as KFFIT [40]. The track fit determines accurate track parameters and their covariances taking the

structure of the tracking detectors into account. Energy losses from ionisation, scattering effects and outlier rejection are also treated at this point.

5.3.2 p_T resolution of reconstructed tracks
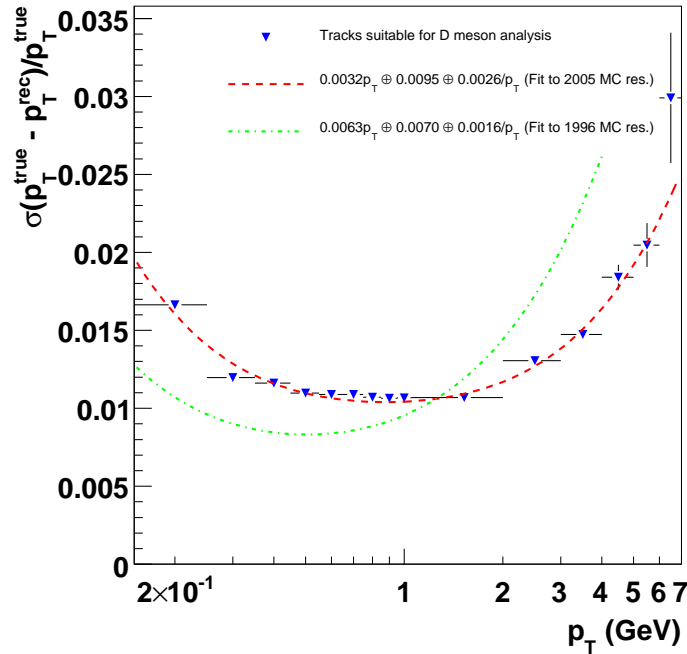
Figure 5.2: *The p_T resolution, σ_{p_T}, as a function of p_T. The blue points represent the σ of the Gaussian fits with the red and green lines showing the resolution parameterisation for this study and the original study during HERA I respectively.*

The momentum resolution of reconstructed tracks is dependent upon many variables. For example, if one were to require a minimum of 4 MVD hits per track the resolution obtained would differ from that obtained if only 2 were required. Previous studies have been performed at ZEUS in order to measure the p_T resolution [45] and their methods are broadly followed here.

A selection of MC events are processed and the reconstructed tracks are matched to the initial "true" tracks using a prediction of the hits that a true track

81

should produce, thus providing a measure of the resolution. In order to make such a study as relevant as possible to the analysis contained in this thesis, the requirements placed upon the tracks are identical to those imposed on the tracks used for the reconstruction of D meson candidates. The only exception is the relaxing of the p_T cut to 0.15 GeV. Resolution distributions are then created for a range of p_T bins and fitted using a Gaussian function with the σ value of the fitted function taken as the p_T resolution in that bin. Figure 5.2 shows the results of the study with the resolution function parameterised as

$$\frac{\sigma(p_T)}{p_T} = a_0 p_T \oplus a_1 \oplus \frac{a_2}{p_T} \tag{5.7}$$

where the parameters a_0, a_1 and a_2 are associated with measured hit precision, multiple scattering in the CTD and multiple scattering between the interaction vertex and the CTD respectively. The symbol $\oplus$ signifies that the terms are added in quadrature. The parameter values found from the study were:

$$\frac{\sigma(p_T)}{p_T} = 0.0032 p_T \oplus 0.0095 \oplus \frac{0.0026}{p_T}. \tag{5.8}$$

This can be compared to the HERA I result;

$$\frac{\sigma(p_T)}{p_T} = 0.0063 p_T \oplus 0.00070 \oplus \frac{0.0016}{p_T}, \tag{5.9}$$

with p_T in GeV. As can be seen a_0 has almost halved showing the much improved tracking precision provided by the MVD. However, this must be balanced with the extra multiple scattering due to the increase in material, as expected a_1 and a_2 increase accordingly. The net effect is that the p_T resolution for low p_T tracks is degraded compared to HERA I but that the resolution for high p_T tracks is improved.

5.3.3 The hit efficiency of the BMVD

The hit efficiency of the MVD is integral to any consideration of the track reconstruction. In this case hit efficiency refers to the frequency with which a

82
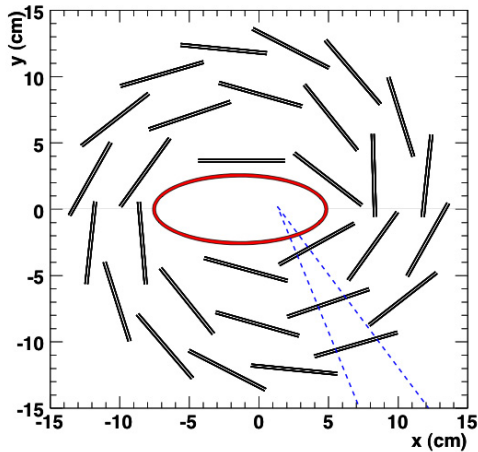
Figure 5.3: *Cross section of the BMVD showing sensor ladders, beampipe and ϕ region chosen for the hit efficiency study.*

track traversing an individual MVD detector wafer will produce a hit which is subsequently associated with the reconstructed track. In order to investigate this each track must have a well known expected number of hits. Due to the geometry of the MVD this requires that all tracks used be found in a specific region of the azimuthal angle, ϕ, and that they be of sufficiently high p_T to be straight. Figure 5.3 shows the region chosen for the study. It passes through three ladders with no overlap between neighbouring ladders and as each ladder contains two layers of silicon detectors the expected number of MVD hits per track is six. The results of the study are given in table 5.1. The hit efficiency is found to be $(96.1 \pm 0.3)\%$ in data with essentially the same value in MC.

5.3.4   Vertex reconstruction

The proper reconstruction of both the primary and secondary vertex is of the utmost importance to the D meson analyses. Analogous to the method for reconstructing a track, the vertex pattern recognition is performed by the VCTRACK package before a more refined vertex reconstruction is performed at a later time.

Event Type	N(Tracks)	N(Hits)	N(Hits)/N(Tracks)	Hit Eff. (%)
Data	131050	755338	5.76	96.1 ± 0.3
MC	129779	751394	5.79	96.5 ± 0.3

Table 5.1: *Results of the BMVD hit efficiency study.*

Initially it is assumed that a primary vertex should be found along the proton beam line; this serves as a soft constraint on the vertex position. Track pairs compatible with both a common vertex and the soft constraint are combined with other track pairs and a vertex is chosen based on the overall χ^2 of the best combination. Once the primary vertex and the associated tracks have been identified a deterministic annealing filter [46] is applied to remove outliers before the final determination of the vertex [47].

In the case of the secondary vertices of D mesons the vertex is fitted using the same algorithm as the primary but with the beam line constraint excluded. The tracks associated to the secondary vertex are chosen by the compatibility of their invariant mass with that of the D meson in question.

5.3.5 The ZEUS beam spot

The beam spot is the region of space within which all primary vertices are expected to be found and is defined by the overlap region of the colliding beams. If the knowledge of this position is sufficiently precise it may provide a better estimate of an event's primary vertex than the explicit reconstruction of the vertex itself.

The width of the ZEUS beam spot has been measured by examining the impact parameter correlations of track pairs in the same event [48]. Figure 5.4 illustrates the general principle. The displacement of the interaction point from the centre of the beam spot is common to all tracks in a given event leading to
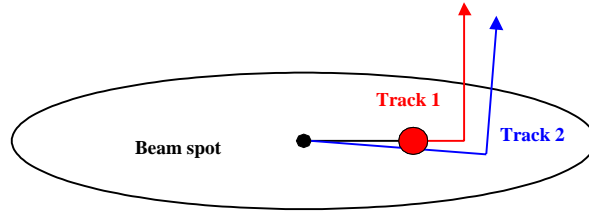
Figure 5.4: *Illustration of the cause of the impact parameter correlation between track pairs from the same event.*

a correlation between the relevant impact parameters. This correlation is free of tracking resolution effects and so is an effective measure of the beam spot. Using this method the ZEUS beam spot was found to be an ellipse of the following dimensions:

$$\sigma_{x,\mathrm{bsp}} = 83.1\,\mu\mathrm{m} \pm 1.2\,\mu\mathrm{m}(\mathrm{stat.}) \pm 8\,\mu\mathrm{m}(\mathrm{syst.})$$

$$\sigma_{y,\mathrm{bsp}} = 19.7\,\mu\mathrm{m} \pm 5.9\,\mu\mathrm{m}(\mathrm{stat.}) \pm 20\,\mu\mathrm{m}(\mathrm{syst.})$$

The position of the ZEUS beam spot is determined by reconstructing the primary vertex of thousands of events and then fitting a Gaussian curve to the resulting distributions. In order to ensure that only vertices from physics events are used in the beam spot determination the following cuts were applied; $\delta > 10$ GeV, $E_T > 5$ GeV, $p_T < 5$ GeV in addition to a timing cut from the calorimeter systems. Here δ, E_T and p_T are the summed $E - p_z$, scalar summed transverse energy and vector summed transverse momentum of the event respectively. A minimum of 5 tracks must have been used to fit the vertex. An example of a Gaussian fit to the x, y and z position can be seen in figure 5.5. Naively, the natural interval for the beam spot determination would be once per luminosity run. However, such runs can vary in length from a few minutes to several hours and as such
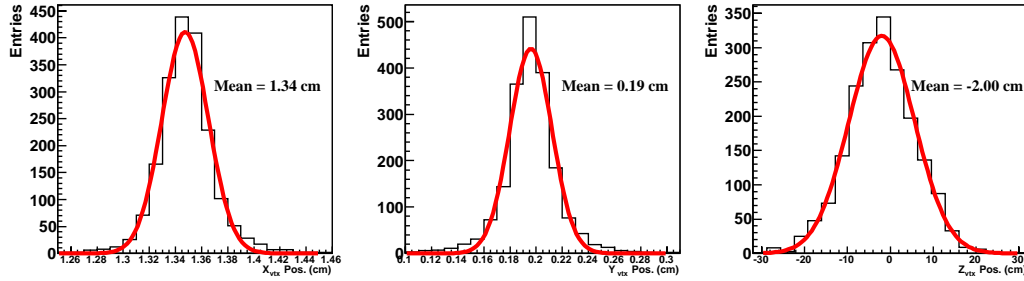
Figure 5.5: *Primary vertex distributions in x, y and z fitted with a Gaussian function.*

there is no guarantee that the beam spot position will be stable over this period. The optimal solution is to determine the beam spot position every n good events over the course of a running period. Figure 5.6 shows the x position of the beam spot as determined every 1000, 2000, 3000, 4000, 5000 and 6000 events during a single proton fill of the HERA storage ring. Significant variations in the beam spot position can be seen. As would be expected the uncertainty associated with the Gaussian fit decreases as the number of fitted vertices grows but this is at the cost of fine detail in the position. For the purposes of the final beam spot determination a frequency of 2000 events was chosen as an optimal balance between precision and granularity.

5.4 D meson candidate reconstruction

Although the exact method of reconstruction for a D meson candidate is dependent upon the decay chain under investigation, the underlying principle is identical. Combinations of tracks with the proper charges are fitted to a common secondary vertex using the same fitting package as used for the primary vertex. These tracks are then designated as "pion" or "kaon" in the proper combination for the decay of interest and the invariant mass of the vertex is found accordingly. If this invariant mass is found to be consistent with a D meson then this combination is accepted
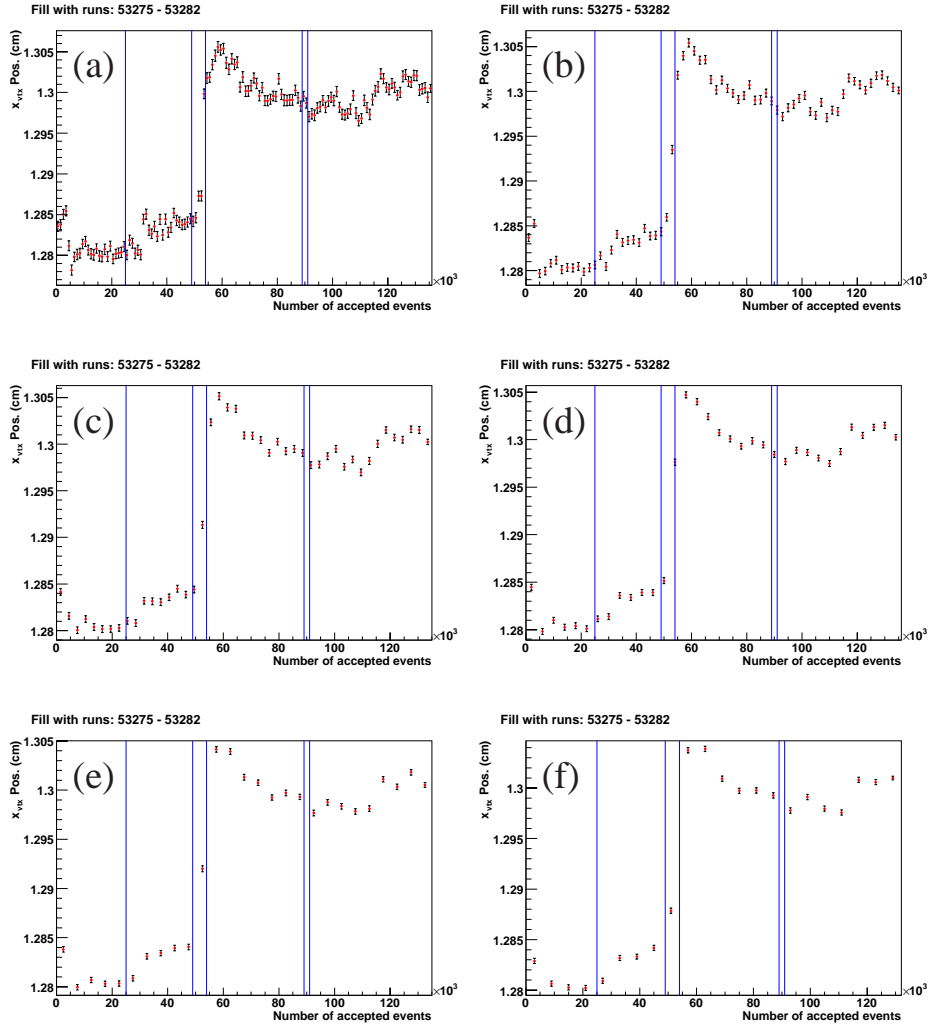
Figure 5.6: *The x position of the ZEUS beam spot during a single proton fill. The position has been measured every (a) 1000, (b) 2000, (c) 3000, (d) 4000, (e) 5000 and (f) 6000 events.*

as a candidate [49].

5.5 Lifetime tags: decay lengths and significance

The relatively long lifetime of a D meson can result in a decay vertex that is spatially separated from the primary interaction point. This property can be used to improve the statistical precision of the signal by reducing the combinatorial background. The decay length of a secondary vertex is defined as the vector between the point of origin of the meson (in the D meson analyses this is the beam spot) and the secondary vertex projected onto the momentum vector of the decayed meson. For the purposes of the analyses contained within this thesis the decay length in the xy plane was used.

$$l_{xy} = \frac{(\vec{S}_{xy} - \vec{B}_{xy}) \cdot \vec{p}^D}{p_T^D} \tag{5.10}$$

where $\vec{S}_{xy}$ is the position of the decay vertex in the transverse plane, $\vec{B}_{xy}$ is the point of origin of the meson, $\vec{p}^D$ is the momentum vector of the D meson candidate and p_T^D is the transverse momentum of the meson. The point of creation of the meson is taken to be the beam spot. The sign of the decay length is defined by the dot product between the D meson momentum vector and the $\vec{S}_{xy} - \vec{B}_{xy}$ vector. In a perfect detector with perfect track reconstruction this sign convention would result in the decay length of all real heavy flavour decays being positive and those of half of the combinatorial background being negative. Resolution effects in a real detector result in a distribution such as that shown in figure 5.7 with some heavy flavour decays smeared into the negative region. The error on the decay length contains information about the resolution of the detector and is defined as a composite variable comprising the uncertainty of the secondary vertex, $\sigma_{l,xy}^{\text{trk}}$, and the beam spot width, σ_{bsp}.

$$\sigma_l = \sqrt{\left(\sigma_{l,xy}^{\text{trk}}\right)^2 + (\sigma_{x,\text{bsp}} \cos\phi)^2 + (\sigma_{y,\text{bsp}} \sin\phi)^2} \tag{5.11}$$
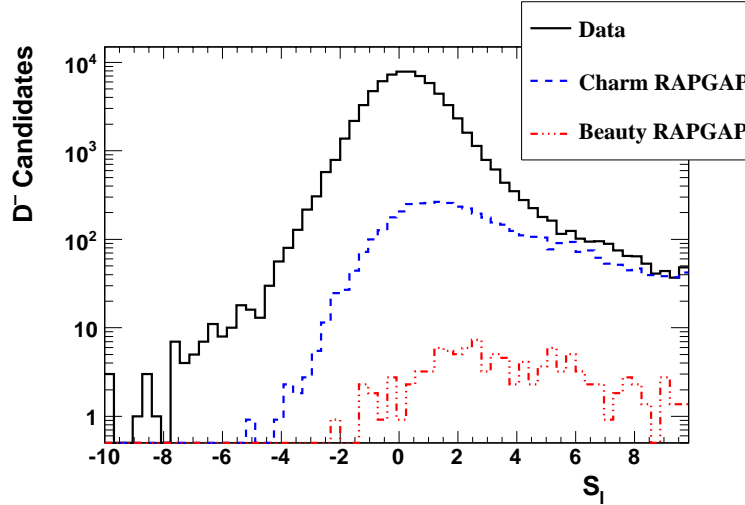
Figure 5.7: *Illustration of the decay length significance, S_l, distribution of $D^{\pm}$ candidates from data, charm MC and beauty MC events. The heavy flavour decays have predominantly positive values of S_l whilst the data distribution which contains combinatorial background from light flavours has significant negative contributions.*

The decay length significance is defined as the decay length divided by the error on the decay length and provides a powerful distinguishing variable for separating combinatorial background from real D meson decays.

$$S_l = \frac{l_{xy}}{\sigma_l} \tag{5.12}$$

The effectiveness of a significance cut is clearly seen in figure 5.8 which shows the invariant $K\pi\pi$ mass distributions for the 1998-2000 and 2005 ZEUS data sets. In this case the number of reconstructed $D^{\pm}$ mesons is not directly comparable as signal (a) represents a slightly different kinematic range to those shown in (b) and (c). However, it can still be clearly seen that the combinatorial background on top of which the signal sits is considerably reduced by application of a significance cut in figure (c). In the case of the 2005 data sets this results in a decrease in the statistical uncertainty from $\approx 8\%$ to $\approx 4\%$.
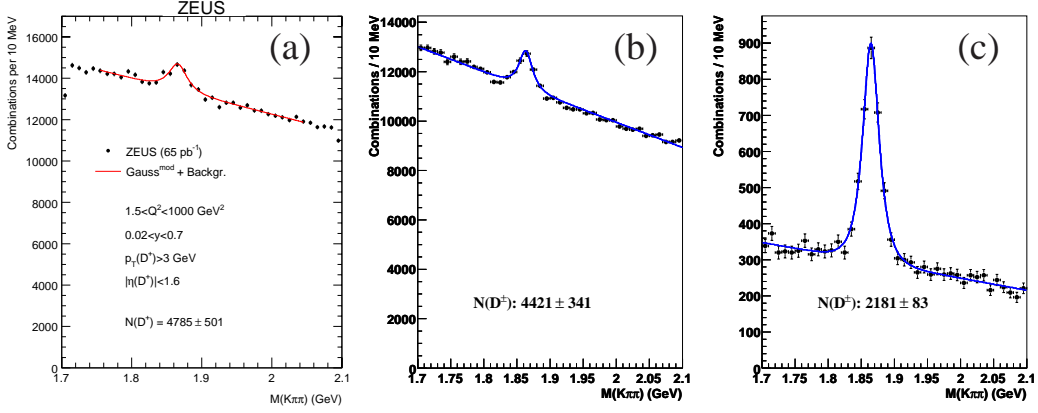
Figure 5.8: $D^\pm$ signals for (a) 98-00 data [20], (b) 2005 data without S_l cut and (c) 2005 data with $S_l > 3$ cut.

5.6 Extraction of D meson signals

By its nature the method used to construct the D meson candidates also creates a large amount of meaningless background. This background can be significantly reduced by making use of lifetime tags such as the decay length significance but nonetheless background remains. In the case of the $D^\pm$ meson there are 15 background candidates for every D meson extracted from the signal.

A fitting procedure was used to extract the meson signals from the mass distributions. Figure 5.9 illustrates a fitted $K\pi\pi$ distribution for the $D^\pm$ meson. The function used for the extraction was a modified Gaussian, eq. 5.13, on top of a background. In the case of the $D^\pm$ the background was parameterised as a straight line, eq. 5.14, with a 2nd order polynomial, eq. 5.15, used in the D^0 analysis.
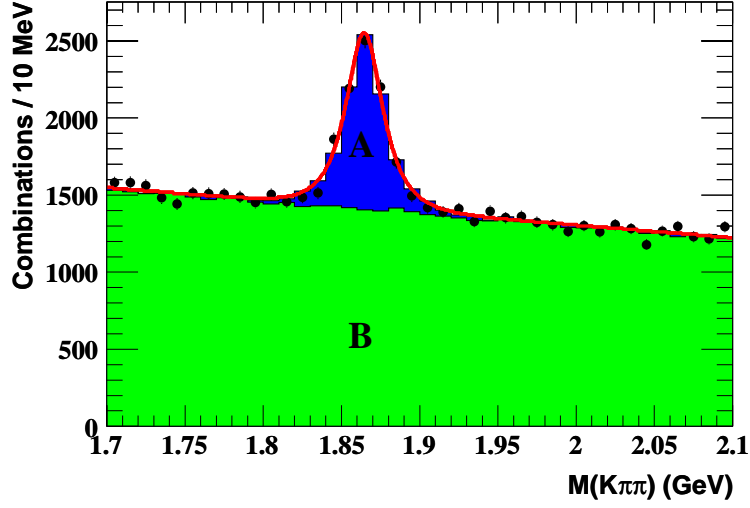
Figure 5.9: *$K\pi\pi$ mass distribution for $D^{\pm}$ mesons separated into signal (blue) and background (green) contributions.*

$$G^{\mathrm{mod}}(x; p_1, p_2, p_3) \;=\; \frac{p_1}{\sqrt{2\pi}\cdot p_3} \exp\left(-\frac{1}{2}X^{1+\frac{1}{1+0.5X}}\right) \tag{5.13}$$

$$B_{D^{\pm}}(x; p_4, p_5) \;=\; p_4 + p_5\cdot x \tag{5.14}$$

$$B_{D^0}(x; p_4, p_5, p_6) \;=\; p_4 + p_5\cdot x + p_6\cdot x^2 \tag{5.15}$$

where $X = |\frac{x-p_2}{p_3}|$, $p_1...p_6$ are the free parameters and x is the invariant mass. The number of D mesons extracted is then $N(D) = \frac{p_1}{\Delta x} \times G_0$ where Δx is the bin width of the mass distribution histogram and G_0 is the normalisation factor of the modified Gaussian found numerically by eq. 5.16.

$$\int_{-\infty}^{\infty} dx\, G^{\mathrm{mod}} = 1.218 \tag{5.16}$$

In the case of the D^0 meson the signal extraction was complicated by the need to remove a reflected signal produced by the incorrect assignment of the kaon and

91

pion masses to the candidate tracks. The shape of the reflected signal was found by reversing the mass assignment of a "tagged" D^0 sample which is consistent with a $D^{*\pm} \to D^0\pi$ decay. The signal reflection was then iteratively normalised to the ratio of tagged to untagged D^0 mesons as found from the fit. In addition the tagged and untagged D^0 meson signals were fitted simultaneously with identical means and widths resulting in greater precision.

5.7   Summary

This chapter detailed the procedures and techniques used to reconstruct events and D meson candidates used for the measurement of $D^\pm$ and D^0 DIS production cross sections and $F_2^{c\bar{c}}$.

Chapter 6

Monte Carlo simulation

No detector is perfect and it is unreasonable to assume that all particles in a given event will be reconstructed with absolute precision. As such, the responses and workings of the ZEUS detector must be thoroughly understood in order to correct for inefficiencies and mis-reconstructions before any measurements can be made. To achieve this understanding, Monte Carlo (MC) techniques are utilised to simulate physics processes and the corresponding detector response.

6.1   Anatomy of a Monte Carlo event

The simulation of a MC event proceeds in several distinct stages; these are depicted in figure 6.1.

- *The initial state* - Consisting, in HERA type events, of a proton and an electron/positron. This stage may also entail simulation of initial state radiation depending on the program used.

- *The hard scattering process* - Simulates the interaction of the boson and the partons of the proton. This process is usually calculated using the leading
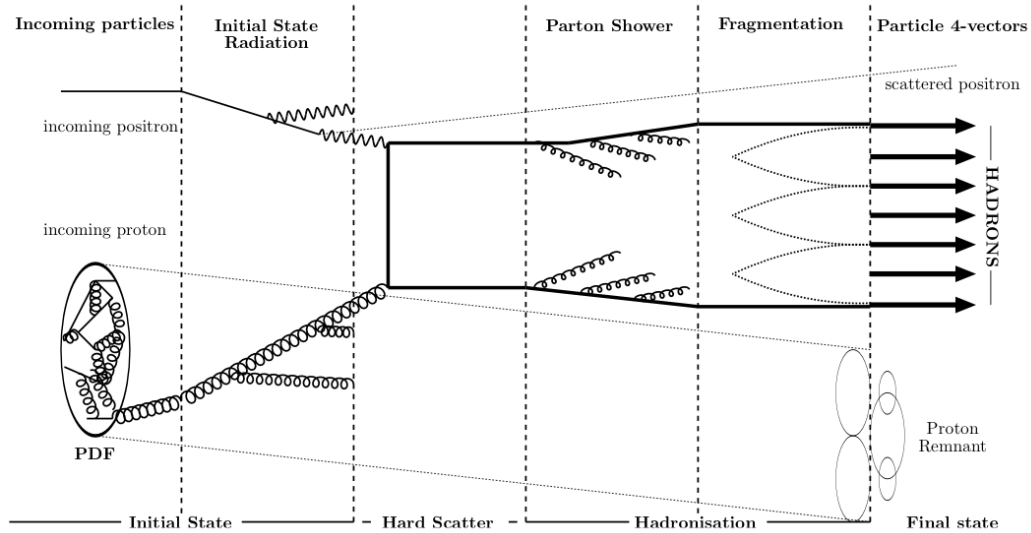
Figure 6.1: *A representation of the stages in the generation of a Monte Carlo event.*

order matrix elements, although in the future this will naturally evolve to next-to-leading order.

- *The fragmentation and hadronisation processes* - These are governed by soft physics that cannot be calculated using the methods of pQCD. Phenominalogical models are used to describe the processes in this stage.

In order for any comparison between data and MC to be valid both must be reconstructed and analysed in the same way. To achieve this the final state particles pass through a simulation of the ZEUS detector produced using the GEANT 3.21 package [50]. This contains the best current knowledge of the state of the detector and simulates the expected signals from particles traversing the numerous sub-detectors. The ZEUS trigger system is then simulated before the MC events are passed through the same reconstruction as those algorithms used for the real data. This finally results in a simulated event that can be analysed in exactly the same way as normal data, but where the true state of the event is also known.

94
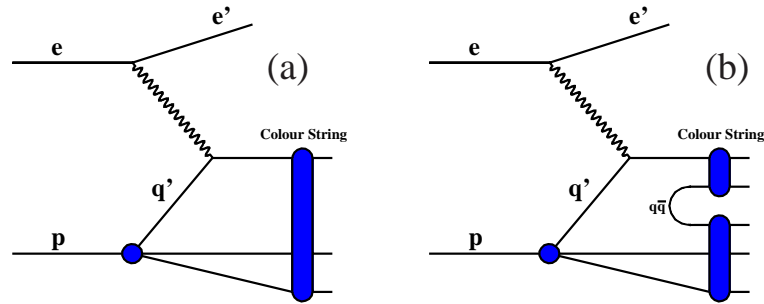
Figure 6.2: *Illustration of the Lund String Concept. A colour string in (a) has produced a $q\bar{q}$ pair leading to two separate shorter colour strings in (b).*

6.2 The RAPGAP MC package

The MC program used for validation and efficiency correction in the analyses was RAPGAP 3.00 [51]. This package was initially designed to describe diffractive events at HERA, although it is also suitable for use in photoproduction and DIS analyses. Heavy flavour production is simulated entirely through the leading order boson gluon fusion (BGF) process (figure 2.1). The proton PDF GRV94 [52] was used for the description of the proton, with the colour dipole model [53] and Lund string fragmentation [54] used to evolve the final state hadrons from the initial hard scatter.

6.2.1 The colour dipole model

The colour dipole model treats the emission of gluons as radiation from the dipole between coloured quarks and gluons as opposed to emission from an individual parton. The three types of dipoles present in the model are $q\bar{q}$, qg and gg.

6.2.2 Lund string fragmentation

The Lund string method uses QCD confinement as its central premise. It models the phenomena as a string of colour force between any coloured partons which is allowed to stretch and break according to input parameters in the model. The breaking of such a string results in the formation of a $q\bar{q}$ pair. This new pair will in turn be linked to the original parton pair by colour strings and the process begins again; figure 6.2 illustrates the concept. Each iteration of the string will be of lower energy than the last and once a pre-determined cut off has been reached the process will halt resulting in coloured partons bound together by vibrating strings forming colourless hadrons.

6.3 Comparison of data and MC

In order for MC to be used for any analyses it must first be shown to describe the data to a satisfactory level. The RAPGAP MC sample used for the D meson analyses was validated by the use of control plots, several of which are shown in figures 6.3 and 6.4 along with the corresponding χ^2/dof values defined by;

$$\chi^2 = \sum_i \frac{(N_{i,\text{data}} - N_{i,\text{MC}})^2}{\sigma_{i,\text{data}}} \qquad (6.1)$$

Each bin corresponds to a fitted D meson signal (section 5.6) with the uncertainty on the data point coming from the quality of the fit. In this way the control plot compares the meson distributions alone whilst removing background. In all variables the MC does a reasonable job of describing the data validating its use for the analyses.
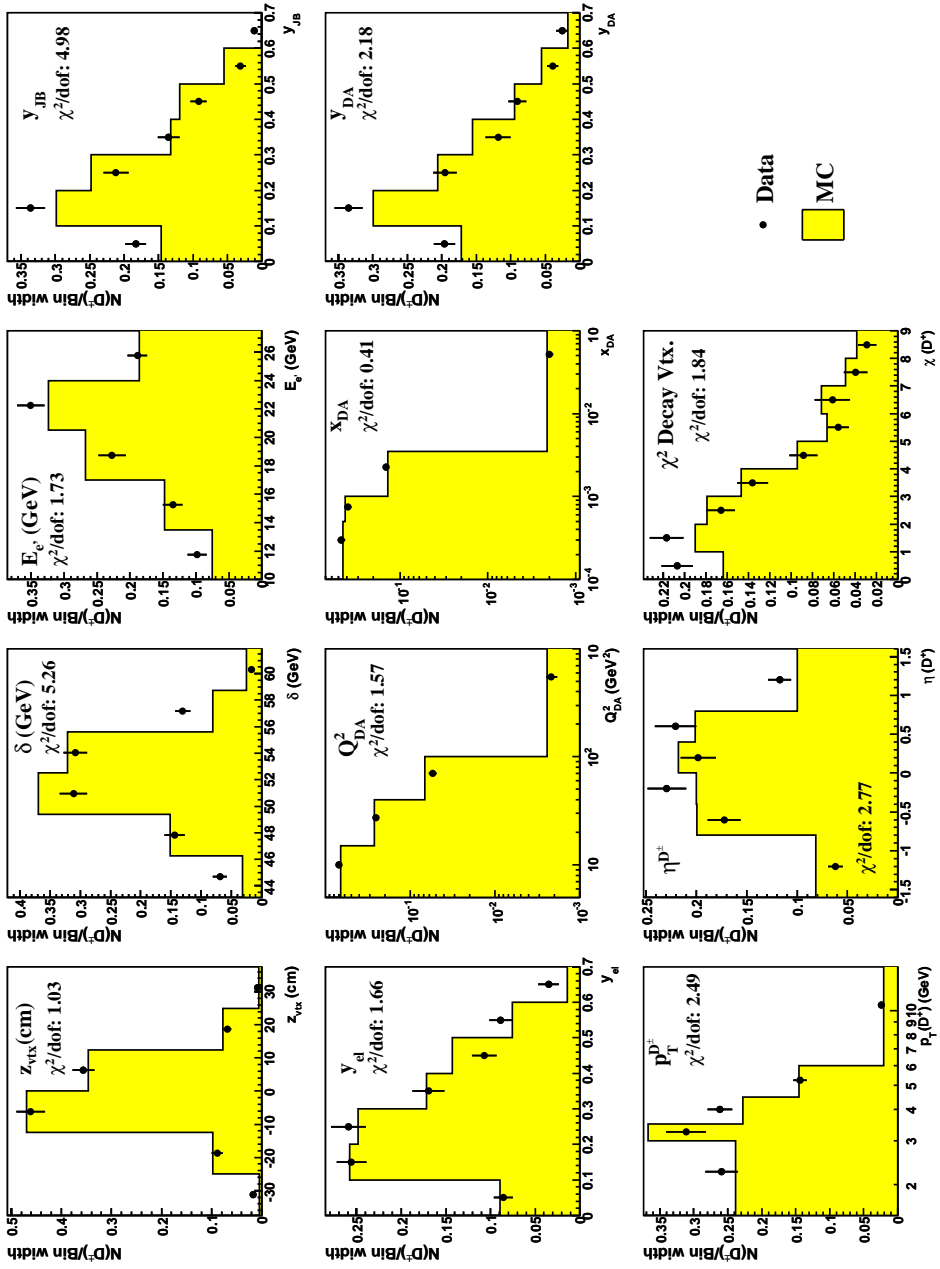
Figure 6.3: $D^{\pm}$ control plots. The χ^2/dof value is shown for each plot as an indication of the agreement between data (points) and MC (shaded).
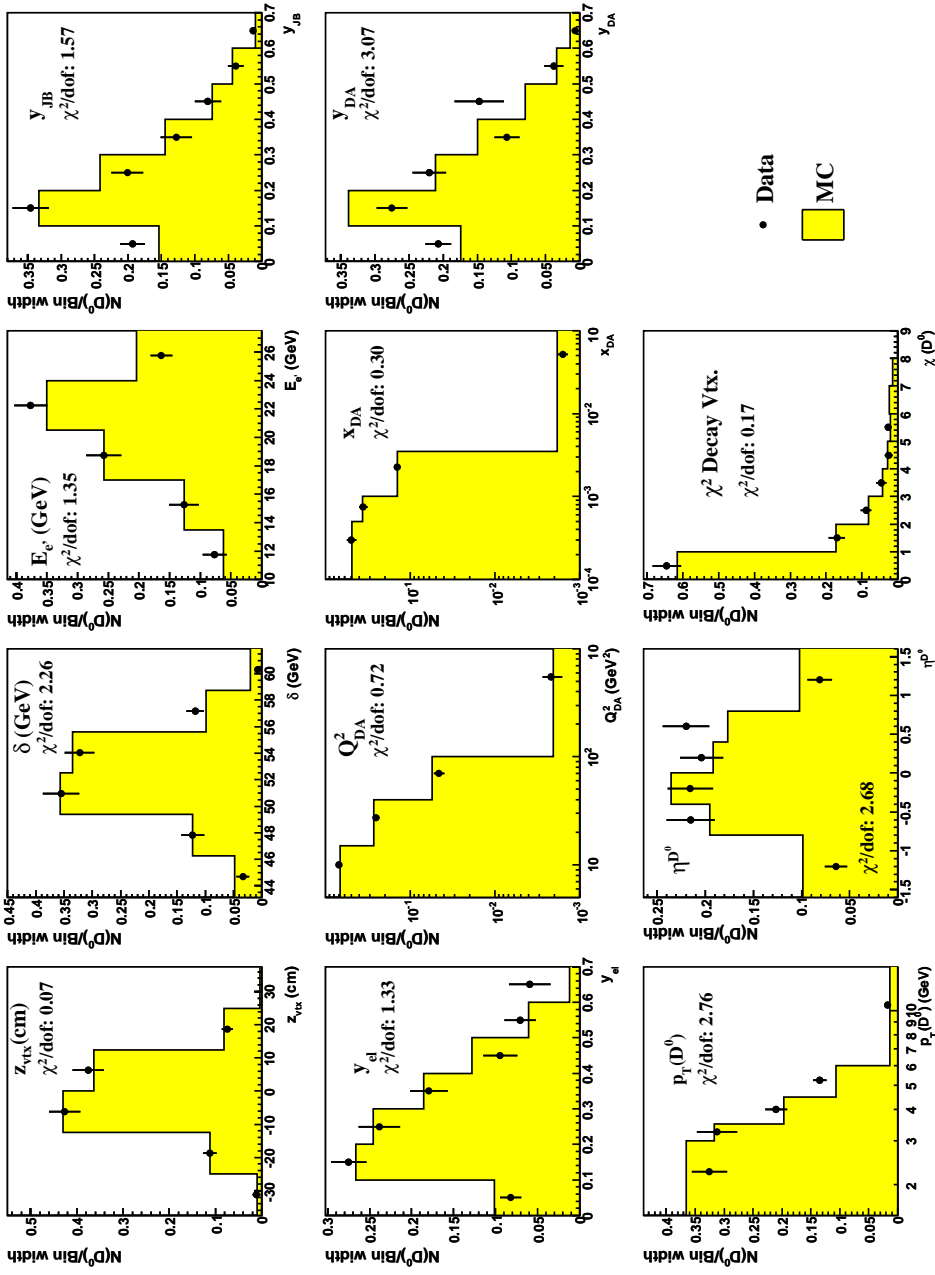
Figure 6.4: D^0 control plots. The χ^2/dof value is shown for each plot as an indication of the agreement between data (points) and MC (shaded).
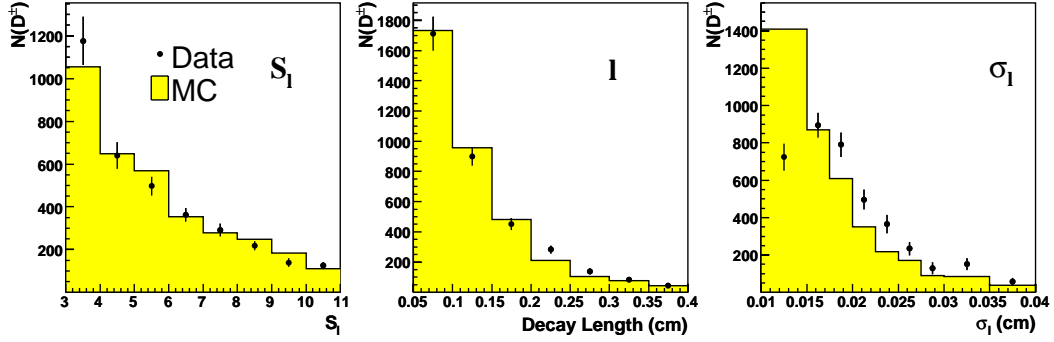
Figure 6.5: *Significance, decay length and decay length error control plots for $D^{\pm}$ mesons. Each bin corresponds to a fitted signal peak in the $K\pi\pi$ invariant mass distribution.*
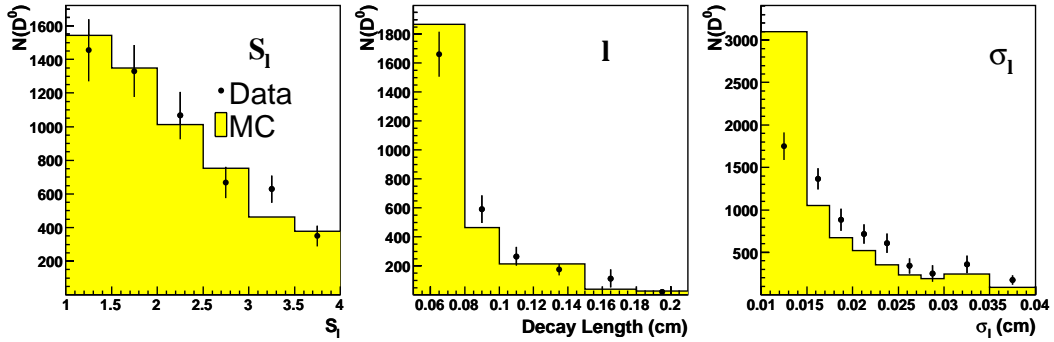
Figure 6.6: *Significance, decay length and decay length error control plots for D^0 mesons. Each bin corresponds to a fitted signal peak in the $K\pi$ invariant mass distribution.*

6.3.1 Decay length error description

One of the strongest cuts applied in the analysis is that on the decay length significance, S_l, so it is imperative that this is properly described in the MC. As defined in section 5.5, S_l is a composite quantity and therefore its contributing variables should also be well described. As can be seen in figures 6.5 and 6.6 this is not the case. Where the significance and decay length distributions for data are well reproduced by the MC in both the $D^{\pm}$ and D^0 cases the decay length error, σ_l, is well described in neither.

At this point it must be remembered that σ_l is itself a composite variable and
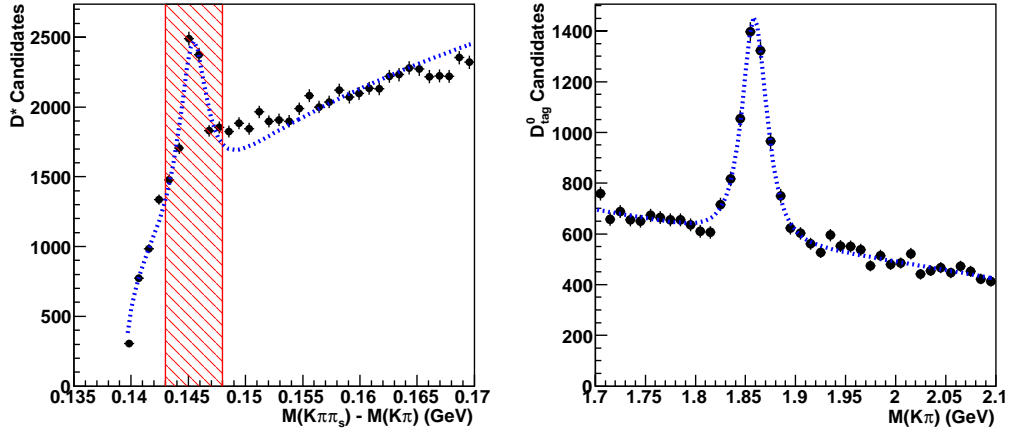
Figure 6.7: D^* and D^0_{tag} signals used for the σ_l study. The shaded area shows the region of the mass tag.

any investigation of the discrepancy between data and MC must take this into account. The decay length error is defined in section 5.5 but is shown again here for completeness.

$$\sigma_l = \sqrt{\left(\sigma^{\text{trk}}_{l,xy}\right)^2 + \left(\sigma_{x,\text{bsp}}\cos\phi\right)^2 + \left(\sigma_{y,\text{bsp}}\sin\phi\right)^2} \qquad (6.2)$$

The values of σ_{bsp} are initial inputs to the MC and as such are known to match the data. This leaves us with the $\sigma_{l,xy}$ term.

$$\sigma_{l,xy} = \sqrt{\cos^2\phi\cdot\text{Cov}^2_x + 2\sin\phi\cdot\cos\phi\cdot\text{Cov}_{xy} + \sin^2\phi\cdot\text{Cov}^2_y} \qquad (6.3)$$

where ϕ is the azimuthal angle of the D meson momentum vector. This definition is intuitive when one considers that the Cov_x term should have zero contribution to the overall uncertainty when the meson is travelling entirely in the y direction. The MC description of the decay vertex covariance was investigated using a sample of tagged D^0 mesons. This sample contains D^0 meson candidates that, when combined with a third track which could be the "slow" pion, π_s, in a $D^* \rightarrow D^0\pi_s$ decay, have $\Delta M = M(K\pi\pi_s) - M(K\pi)$ in the range $0.143 < \Delta M < 0.148$ GeV. Tagged D^0 mesons are independent of the analysis sample and produce a clean

100
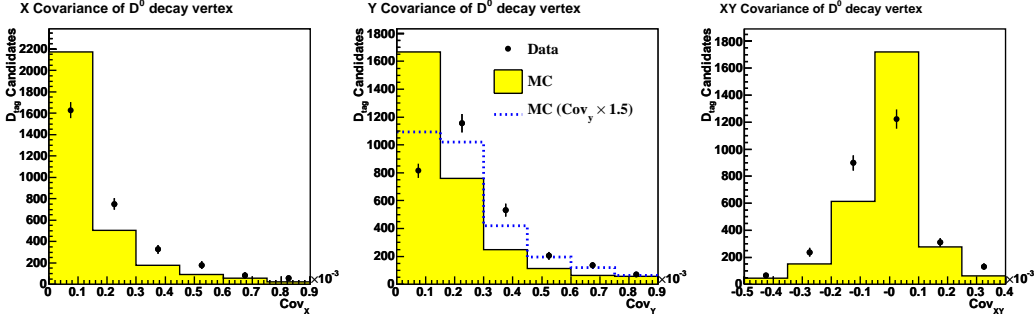
Figure 6.8: *Comparison of the decay vertices x, y and xy covariance for data and MC using tagged D^0 mesons*

signal without the need for a lifetime cut to reduce the combinatorial background (figure 6.7).

Figure 6.8 shows the comparison of data and MC for the decay vertex covariance terms. The MC does not reproduce the shape of the data, particularly for the Cov_y term ($\chi^2/dof \approx 40$). However, by increasing the value of Cov_y by 150 % the description is markedly improved ($\chi^2/dof \approx 5$). Figure 6.9a shows the MC description of the data for σ_l after the factor is applied. It can be seen that further tuning of the MC is necessary in order to achieve a satisfactory description. This is achieved by assigning a weight to each D meson candidate defined by a function fitted to the ratio of the data to MC for the tagged D^0 decay length error plot.

$$R(\sigma_l; p_1, p_2) = p_1 \cdot \tan^{-1}(p_1 (\sigma_l - 0.01)) \tag{6.4}$$

The weights applied to the MC candidates are calculated by considering both the central value of the fitted parameters and their uncertainties resulting in a spread of weighting values about the central function (figure 6.9).

It is a requirement of the weighting procedure that the number of D mesons, $N(D)$, reconstructed in a given analysis bin, i, before the application of a significance cut is independent of the weighting procedure. Figure 6.10 shows

101
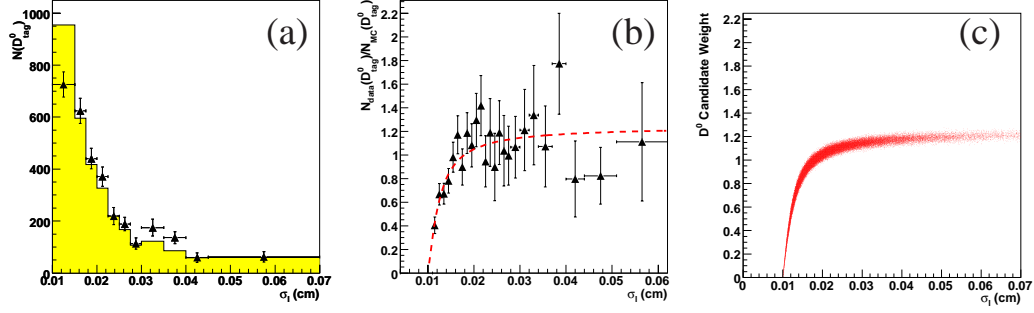
Figure 6.9: *(a)* σ_l *distribution for* D^0_{tag} *mesons, (b) ratio of data to MC and (c) weights applied to MC candidates.*

that this number is not independent and so a correction factor given by

$$S = \frac{N(D)_{\text{unweighted}}}{N(D)_{\text{weighted}}} = \frac{a}{b} \tag{6.5}$$

must be applied on a bin-by-bin basis. The uncertainty on the correction factor takes the correlation between $N(D)_{\text{unweighted}}$ and $N(D)_{\text{weighted}}$ into account and is given by

$$\left(\frac{\sigma_S}{S}\right)^2 = \left(\frac{\sigma_a}{a}\right)^2 + \left(\frac{\sigma_b}{b}\right)^2 - 2\left(\frac{\sigma_a}{a}\right)\left(\frac{\sigma_b}{b}\right)\rho_{ab} \tag{6.6}$$

where ρ_{ab} is the correlation coefficient of a and b.

The effectiveness of the weighting procedure can be assessed by examining the MC description of the efficiency as a cut on S_l or σ_l is introduced and raised. The efficiency in this case is defined as the fraction of D mesons remaining above a given value of the cut variable. Figure 6.11 shows the efficiency curve for S_l and σ_l in the D^0 analysis with the weighted MC providing a much improved description of the data. The same distribution for the $D^\pm$ analysis (figure 6.12 a & b) shows that the MC describes the shape of the S_l data efficiency curve well but that the two are offset. This can be resolved by the addition of 20 μm to the decay length uncertainty and 1 to the decay length significance in the MC (figure 6.12 c & d). The relative ineffectiveness of the weighting correction for the $D^\pm$ compared to the
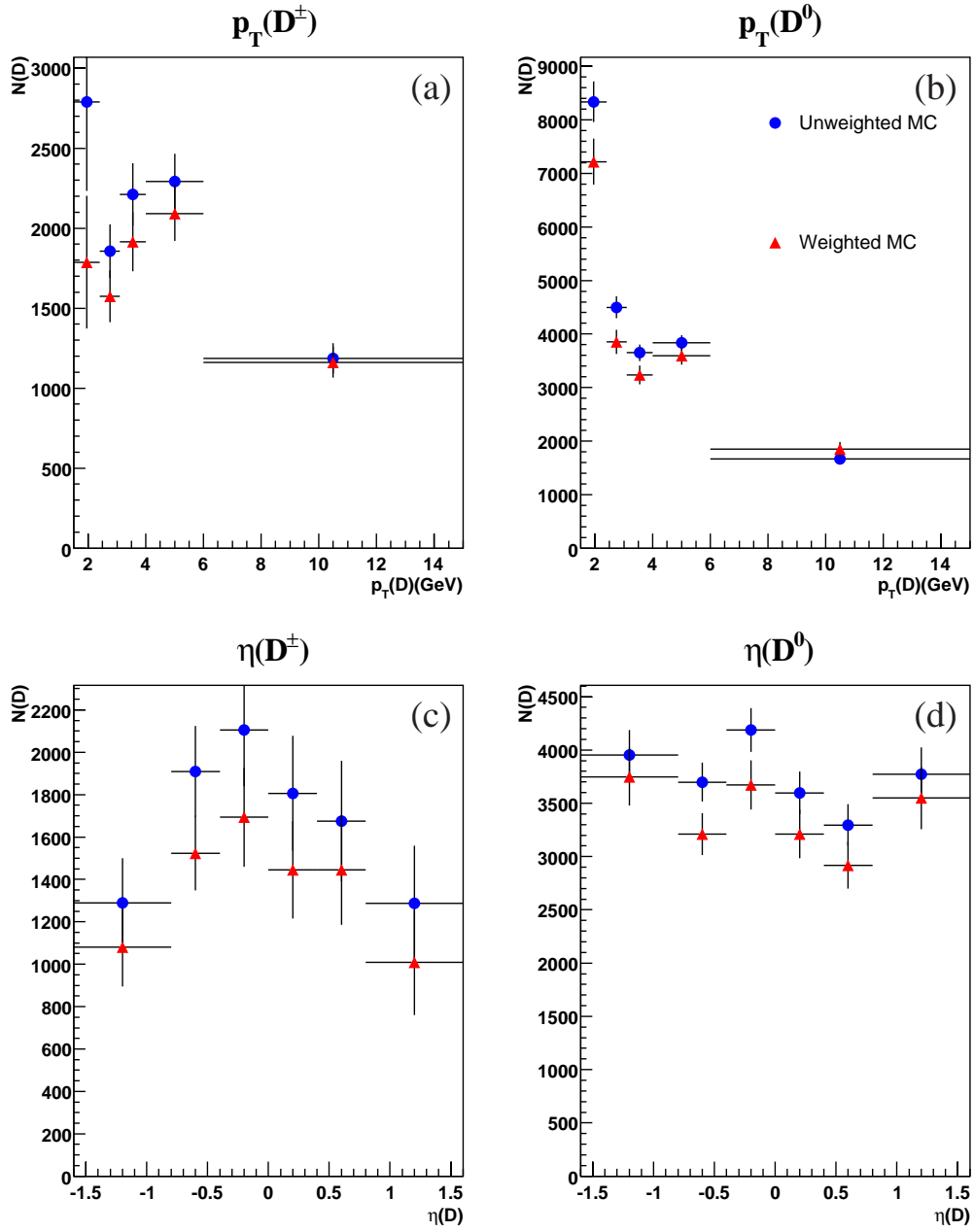
Figure 6.10: *Number of $D^{\pm}$ (a & c) and D^0 (b & d) mesons reconstructed from the weighted and un-weighted MC samples in $p_T(D)$ and $\eta(D)$ bins.*
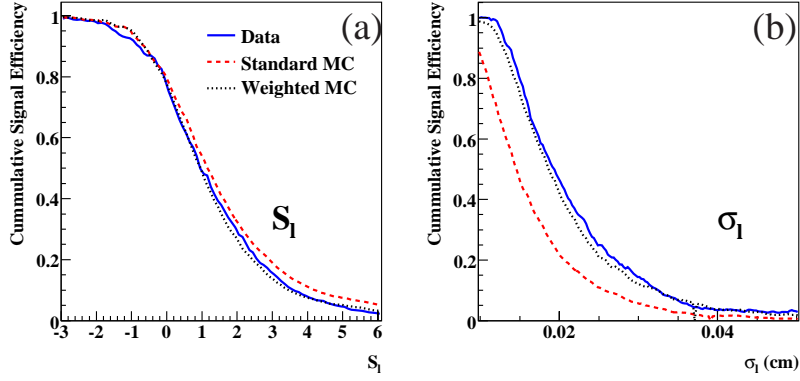
Figure 6.11: *Efficiency of (a) S_l and (b) σ_l cuts for D^0 mesons.*
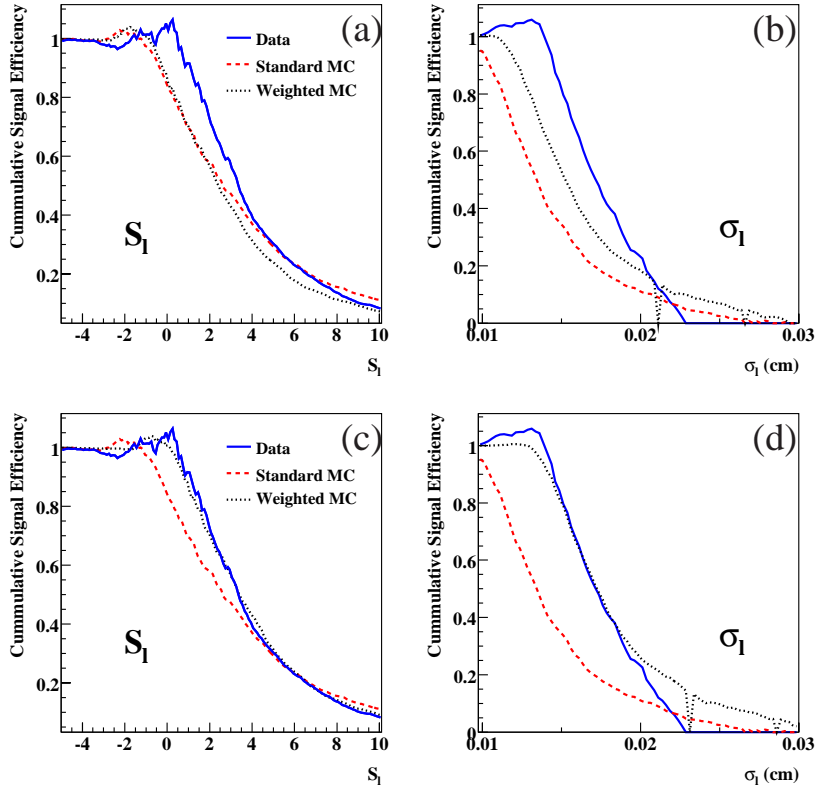
Figure 6.12: *Efficiency of (a & c) S_l and (b & d) σ_l cuts for $D^{\pm}$ mesons. Figures c & d show the efficiency curves after the addition of 1 and 20 μm to S_l and σ_l respectively in the weighted MC.*
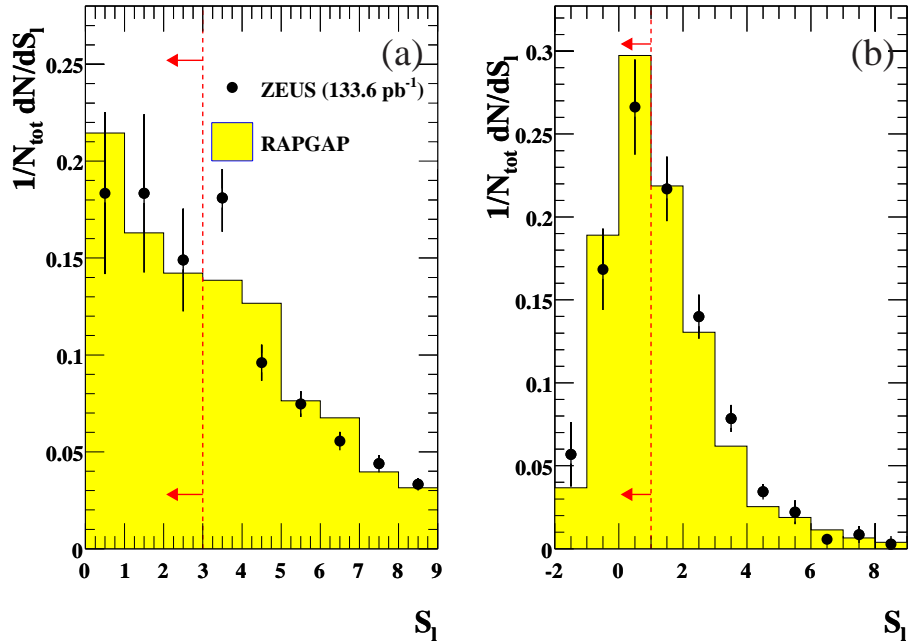
Figure 6.13: *MC description of data as a function of S_l for (a) $D^{\pm}$ and (b) D^0 mesons with the analysis cuts at 3 and 1 shown by the red line.*

D^0 is attributed to the fact that the weighting function is derived from the tagged D^0 sample. Figure 6.13 shows the final description of the data by the MC for S_l.

This procedure corrects for the MC description of the decay length uncertainty by dealing with composite variables such as covariance. The root cause of this discrepancy is the MC description of tracks in the detector. Any future analyses will benefit from more advanced and realistic simulation of the ZEUS detector by the MC, reducing or removing the need for such a weighting procedure.

6.4   MVD dead strip simulation

During any given running period a percentage of the MVD strips was inactive or in some way faulty. Within ZEUS faulty strips were assigned one of four states;
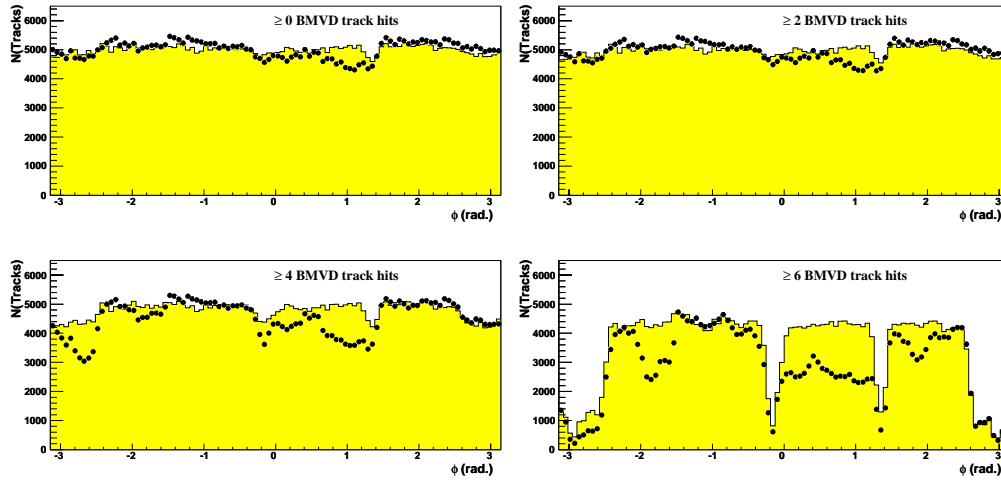
Figure 6.14: *The ϕ distributions of data (points) and MC (shaded) tracks with 0, 2, 4 and 6 associated BMVD hits.*

lazy, noisy, super-noisy and dead. Lazy and noisy were strips treated in the same way as good strips while super-noisy and dead strips[1] were masked and prevented from contributing to an MVD hit cluster during the reconstruction of an event. The default MC simulation of the MVD assumed a perfect detector which had no dead strips and as such did not properly describe the real state of the MVD. This can be seen in figure 6.14 which shows the ϕ distribution of data and MC tracks with 0, 2, 4 and 6 associated hits in the BMVD. The MC distributions are nomalised such that the data and MC distributions have the same area when 0 hits are required, with the same factor then being applied to each of the subsequent distributions. It can be seen that as an increasing number of hits are required the description of the data by the MC deteriorates. This can be attributed to the lack of dead strips in the MC producing too many hits in comparison to the data.

The method used to simulate the effects of dead strips in the MC is summarised below:

---

[1]From this point forward "dead strips" will be taken to mean those which are super-noisy or dead.
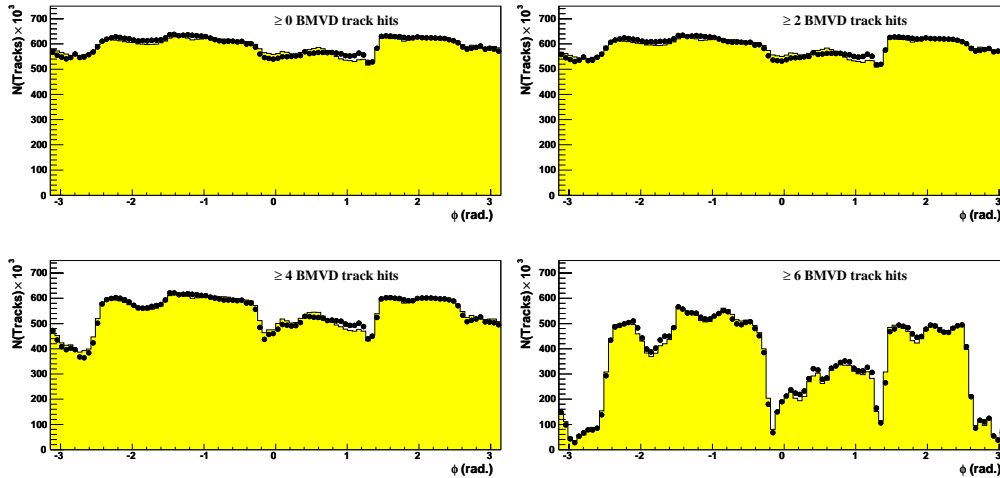
Figure 6.15: *The ϕ distributions of data (points) and MC (shaded) tracks with 0, 2, 4 and 6 associated BMVD hits with dead strip simulation included in the MC.*

- The probability of each strip being dead is found by taking the number of runs for which a strip was in that state divided by the total number of runs in a period. This information is then stored for use in the MC reconstruction;

- Before the point in the MC reconstruction where the simulated signals from several strips are combined to form a hit cluster a random number is generated for each module in the MVD;

- This random number is compared to the probability of each strip being dead;

- If the number is less than the probability of the strip being dead then the signal on that strip is set to zero.

The effectiveness of the dead strip simulation is shown in figure 6.15 where ϕ distributions are shown comparing data with the modified MC.

6.5 Acceptance, purity and efficiency corrections

Monte Carlo events were used to evaluate the efficiency, $\mathcal{E}$, and purity, $\mathcal{P}$, for analyses containing discrete bins, i, which are given by;

$$\mathcal{E}_i = \frac{N_i^{\text{Gen}} \cap N_i^{\text{Rec}}}{N_i^{\text{Gen}}} \tag{6.7}$$

$$\mathcal{P}_i = \frac{N_i^{\text{Gen}} \cap N_i^{\text{Rec}}}{N_i^{\text{Rec}}} \tag{6.8}$$

where N_i^{Rec} and N_i^{Gen} are the number of events reconstructed and generated in bin i respectively. Using this definition the numerator of each expression represents the number of events in bin i which are both generated and reconstructed in that bin. Efficiency can therefore be interpreted as the fraction of events generated in bin i which are also reconstructed in the same bin. Similarly, purity can be seen as the fraction of events reconstructed in bin i which were generated in that bin. The value of $\mathcal{E}_i$ gives an indication of the extent to which a measurement is reliant on the MC simulation, with high values corresponding to the reconstruction of most of the generated events and therefore a smaller reliance on MC based corrections. High values of $\mathcal{P}_i$ imply low levels of migrations from neighbouring bins and therefore the suitability of the chosen bin widths for the detector resolution.

Cuts were made to ensure clean reconstructed signals for the analysis, leading to inefficiencies in the reconstruction of events. This inefficiency is compensated for with the correction factor, $\mathcal{C}_i$, given by;

$$\mathcal{C}_i = \frac{\mathcal{P}_i}{\mathcal{E}_i} = \frac{N_i^{\text{Gen}}}{N_i^{\text{Rec}}}. \tag{6.9}$$

The differential cross section $\frac{d\sigma_i}{dY}$, is calculated from the number of D mesons extracted using the fitting procedure, $N_i(D)$, for a given integrated luminosity, $\mathcal{L}$
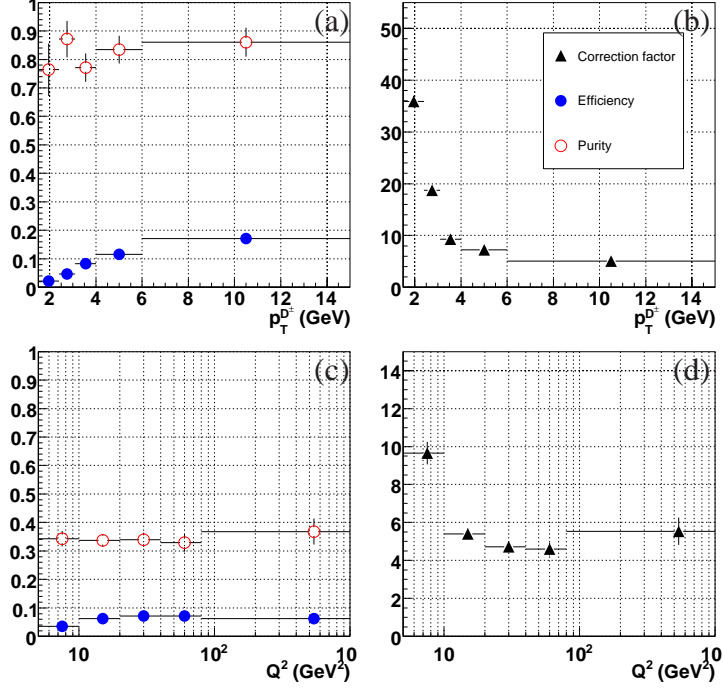
Figure 6.16: *Purity, efficiency and correction factor as a function of $p_T^{D^{\pm}}$ for the $D^{\pm}$ analysis (a & b) and Q^2 for the D^0 analysis (c & d).*

using the relation;

$$\frac{d\sigma_i}{dY} = \frac{N_i(D) \cdot \mathcal{C}_i}{\mathcal{L} \cdot \Delta Y \cdot \mathcal{B}}. \tag{6.10}$$

Where ΔY is the bin width and $\mathcal{B}$ is the branching ratio of the decay process. The effects of QED initial state radiation are taken into account in the calculation of $\mathcal{C}_i$.

Figure 6.16 shows the correction factor, efficiency and purity as a function of $p_T^{D^{\pm}}$ for $D^{\pm}$ and Q^2 for the D^0 analyses respectively; the full selection of such figures relevant to the analyses are contained in Appendix A. As a function of $p_T^{D^{\pm}}$ the purity is of the order 100% which can be ascribed to both the exceptional momentum resolution of reconstructed tracks preventing bin-to-bin migrations and the background rejection power of the S_l cut. The correction factor shows a strong dependence on p_T with 2% and 20% of generated $D^{\pm}$ mesons being reconstructed in the different bins. This feature is due to both the difficulty in reconstructing

very low momentum tracks and the use of a decay length measured in the xy plane only. D mesons with momentum vectors mainly along the z axis will have a much foreshortened decay length once projected onto the xy plane, resulting in their likely rejection by any lifetime cut. The significant feature of the Q^2 plots is the decreasing correction factor with increasing values of Q^2 and the consistently lower purity. The behaviour of the correction factor is a result of both the S_l cut and the difficulty in reconstructing a scattered electron at lower values of Q^2. The comparatively low purity can be ascribed to the looser S_l cut used in the D^0 analysis, which is itself a consequence of the lifetime of the D^0 meson being roughly $\frac{1}{3}$ that of the $D^\pm$. A comparison can be drawn between the acceptances of the analyses in this thesis and the ZEUS $D^{*\pm}$ analysis which was conducted in a similar kinematic range [55]. The use of the S_l cut increases the correction factor by four and two times the $D^{*\pm}$ value for the $D^\pm$ and D^0 analyses respectively.

Chapter 7

Analysis method for $D^{\pm}$ and D^0 production in deep inelastic scattering

The production of $D^{\pm}$ and D^0 mesons has been measured with the ZEUS detector at HERA II using an integrated luminosity of $133.6\,\mathrm{pb}^{-1}$. The measurements cover the kinematic range

$$
\begin{aligned}
5 < Q^2 &< 1000\,\mathrm{GeV}^2 \\
0.02 < y &< 0.7 \\
1.5 < p_T^D &< 15\,\mathrm{GeV} \\
|\eta^D| &< 1.6
\end{aligned}
$$

The $D^{\pm}$ and D^0 meson lifetimes are extracted and total, single and double differential cross sections are measured and compared to the NLO prediction from HVQDIS. The open charm contribution, $F_2^{c\bar{c}}$, to the proton structure function, F_2, is extracted and compared to the predictions from the ZEUS FFN fit and previous ZEUS results.

Figure 7.1: *RAPGAP generator level distribution of $D^{\pm}$ mesons in the range $5 < Q^2 < 1000 \text{ GeV}^2$ and $0.02 < y < 0.07$.*

7.1 Extrapolation factors at lower p_T^D

Figure 7.1 shows the generator level p_T^D and η^D distribution from RAPGAP for $D^{\pm}$ mesons in the range $5 < Q^2 < 1000 \text{ GeV}^2$ and $0.02 < y < 0.7$ range. It can be seen that the chosen p_T^D and η^D range encompasses $\approx 37\%$ of the available phase space. Previous analyses involving the $D^{\pm}$ and D^0 mesons at ZEUS [20] have been limited to a range of $p_T^D > 3$ GeV. This was primarily due to the exponential increase in combinatorial background as decay tracks of increasingly lower p_T are considered. With the lifetime tagging afforded by the MVD this background can be brought under control and useful results extracted in this region. Figure 7.2 shows the $D^{\pm}$ signal in the range $1.5 < p_T^{D^{\pm}} < 3.0$ GeV before and after the application of significance cut of $S_l > 3$. In this range the statistical precision of the fit improves by a factor ≈ 2.5 from the application of the S_l cut.

In order to provide the most rigorous test of theoretical predictions it is necessary to conduct measurements in as inclusive a kinematic region as possible. In the case of the extraction of $F_2^{c\bar{c}}$ the extension to lower p_T^D is even more
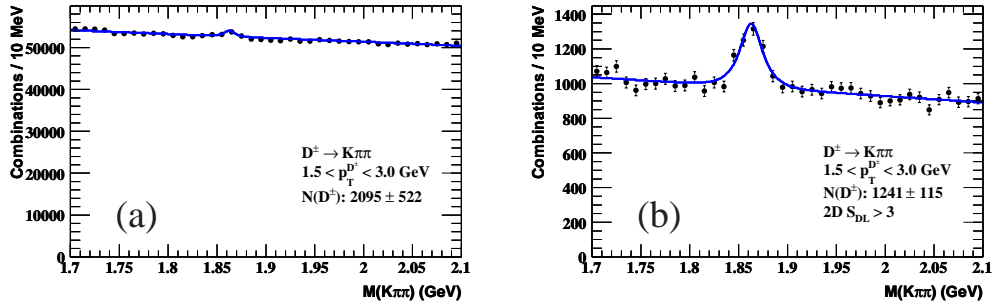
Figure 7.2: *The $M(K\pi\pi)$ distribution for $D^\pm$ mesons in the range $1.5 < p_T^{D^\pm} < 3.0$ GeV (a) before and (b) after the application of a significance cut of $S > 3$.*

important. In order to extract $F_2^{c\bar{c}}$ the charm cross sections must be extrapolated to the full p_T^D and η^D phase space using a factor given by the ratio of the predicted visible cross section in the measured kinematic range to that in the full phase space. The magnitude of this extrapolation factor is therefore inversely proportional to the size of the kinematic range in which the original cross section was measured. Thus a larger initial kinematic range will result in less reliance on the theoretical prediction in the extracted $F_2^{c\bar{c}}$ value. Extrapolation factors are shown in table 7.1 for a range of $F_2^{c\bar{c}}$ extraction points and it can be seen that the extension in the kinematic range has the largest impact at low Q^2 where the extrapolation factor decreases to approximately 20% of its previous value.

7.2 Candidate selection

The photon virtuality Q^2, the Bjorken scaling variable, x, and the fraction of the electron energy transferred to the proton in its rest frame, y, were reconstructed using the double angle (DA) method (section 5.2.3) which relies on the angles of the scattered electron and the hadronic energy flow.

Events were selected offline with the following requirements.

- HFL02 or SPP01 at third level;

113

Q^2 (GeV^2)	y range	Extrapolation Factor $3 < p_T^D < 15$ GeV	Extrapolation Factor $1.5 < p_T^D < 15$ GeV
	0.02 - 0.12	15.4	3.1
7.0	0.12 - 0.30	8.3	2.3
	0.30 - 0.7	7.9	3.2
	0.02 - 0.12	6.5	2.4
20.0	0.12 - 0.30	4.6	1.8
	0.30 - 0.7	5.2	2.5
	0.02 - 0.12	3.3	2.4
110.0	0.12 - 0.30	2.1	1.5
	0.30 - 0.7	2.3	1.7

Table 7.1: *Extrapolation factors for kinematic ranges with a lower p_T^D limit of 3 GeV and 1.5 GeV.*

- $E_{e'} > 10$ GeV, where $E_{e'}$ is the energy of the scattered electron. The electron was identified using an algorithm which uses a combination of calorimeter and tracking information to differentiate DIS electrons from background;

- $y_{\mathrm{el}} < 0.95$, where y_{el} is determined with the electron method (section 5.2.1). This condition removes events where fake electrons are found in the FCAL;

- $y_{\mathrm{JB}} > 0.02$ This condition rejects events where the hadronic system cannot be measured precisely;

- $40 < \delta < 65$ GeV, where $\delta = \sum E_i(1 - \cos(\theta_i))$ and E_i is the energy of the ith energy–flow object (EFO) [56]. EFOs are estimators of particle states constructed from charged tracks as measured in the CTD and MVD, and energy clusters measured in the CAL. The sum i runs over all EFOs;

- $|z_{\mathrm{vtx}}| < 50$ cm, where z_{vtx} is the primary vertex position determined from
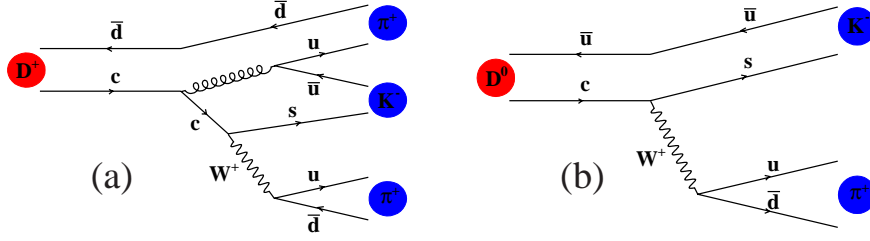
Figure 7.3: *Decay chains used for the reconstruction of (a) $D^\pm$ and (b) D^0 mesons.*

tracks;

- the impact point (x, y), of the scattered electron on the surface of the RCAL must lie outside the region (15 cm, 15 cm) centred on (0,0).

Electron candidates in the regions between the barrel, forward and rear calorimeters were rejected due to the poor energy reconstruction in these areas. The angle of the scattered electron was determined using either its impact position on the CAL inner face or a reconstructed track. When available, SRTD and HES were also used. The energy of the scattered electron was corrected for non-uniformity due to geometric effects caused by cell and module boundaries.

The selected kinematic region was $5 < Q^2 < 1000 \,\mathrm{GeV}^2$ and $0.02 < y < 0.7$. The production of $D^\pm$ and D^0 charm mesons was measured in the range of transverse momentum $1.5 < p_T^D < 15 \,\mathrm{GeV}$ and pseudorapidity $|\eta^D| < 1.6$. The decay length significance, S_l, as defined in section 5.5 was used to reduce the combinatorial background to the $D^\pm$ and D^0 signals.

The $D^\pm$ meson was reconstructed in the decay channel $D^\pm \rightarrow K^\mp \pi^\pm \pi^\pm$ (figure 7.3a). In each event all track pairs with equal charges were combined with a third track with opposite charge to form a $D^\pm$ candidate. The pion mass was assigned to the tracks with equal charges and the kaon mass was assigned to the remaining track. These were then fitted to a decay vertex and the invariant

115
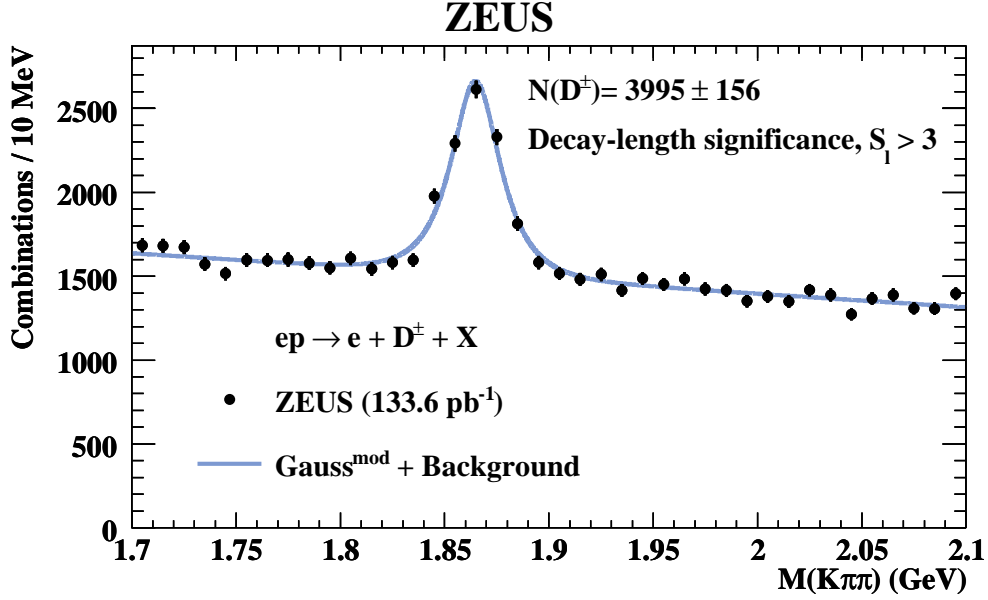
Figure 7.4: *The $M(K\pi\pi)$ distribution for the $D^{\pm}$ candidates (dots). The solid curve represents a fit to the sum of a modified Gaussian function and a linear background function.*

mass, $M(K\pi\pi)$, was calculated. The tracks were required to have transverse momentum $p_T^{\pi} > 0.25\,\text{GeV}$ and $p_T^{K} > 0.5\,\text{GeV}$ for the pion and kaon tracks, respectively. To ensure that all tracks used were well reconstructed they were required to have passed through 3 superlayers of the CTD and have 2 $r\phi$ and 2 $z\phi$ hits in the BMVD. Background from $D^{*\pm}$ is suppressed by removing one of the pions from the invariant mass calculation and requiring that the mass difference is not in the range $1.43 < \Delta M < 0.148\,\text{GeV}$. Background from the decay $D_s^{\pm} \to \phi\pi$ is suppressed by assuming that one of the tracks identified as a pion is a kaon in a $\phi \to K^+K^-$ decay. Candidates are then rejected if the calculated invariant mass is in the range $1.0115 < M(KK\pi) < 1.0275$. The combinatorial background was reduced by the requirements that the χ^2 of the decay vertex be less than 9 and that the decay–length significance, S_l, be greater than 3. Figure 7.4 shows

ZEUS

N(D$^{\pm}$)= 4383 ± 353

ep → e + D$^{\pm}$ + X

• ZEUS (133.6 pb^{-1})
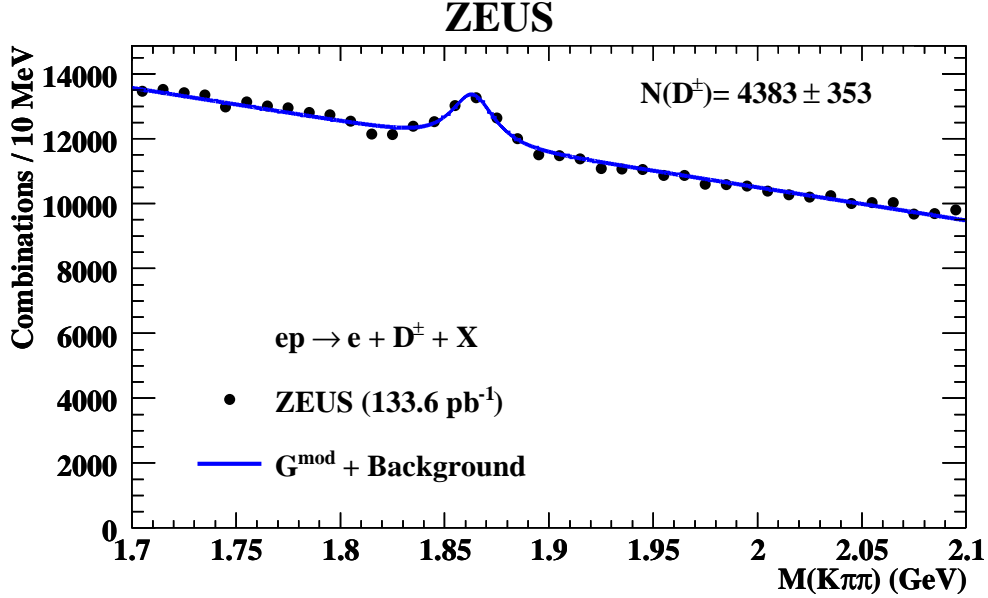
— G^{mod} + Background

Figure 7.5: *The $M(K\pi\pi)$ distribution for the $D^{\pm}$ lifetime candidates (dots). The solid curve represents a fit to the sum of a modified Gaussian function and a linear background function.*

the $M(K\pi\pi)$ distribution for $D^{\pm}$ candidates. In order to extract the number of reconstructed $D^{\pm}$ mesons the $M(K\pi\pi)$ distribution was fitted with the sum of a modified Gaussian function and a linear background function (section 5.6). The number of reconstructed $D^{\pm}$ mesons yielded by the fit was $N(D^{\pm}) = 3995 \pm 156$.

Figure 7.5 shows the $M(K\pi\pi)$ distribution for a sample of $D^{\pm}$ candidates with $p_T^{\pi} > 0.5$ GeV, $p_T^{K} > 0.7$ GeV and $p_T^{D^{\pm}} > 3$ GeV, used to obtain the lifetime of the $D^{\pm}$ meson. The higher p_T cuts were used to obtain a clean signal with no requirements made on the significance of the decay length. The number of reconstructed $D^{\pm}$ mesons yielded by the fit to the data was $N(D^{\pm}) = 4383 \pm 353$.

The D^0 mesons were reconstructed in the decay channel $D^0 \rightarrow K^{\pm}\pi^{\mp}$ (figure 7.3b), with candidates found in a similar manner to the $D^{\pm}$, except that only oppositely charged pairs of tracks were combined together to form the meson

117

candidate. The tracks were required to have transverse momentum $p_T^K > 0.7\,\mathrm{GeV}$ and $p_T^\pi > 0.3\,\mathrm{GeV}$ for the kaon and pion tracks respectively. Due to the difference in lifetime and decay channel compared to the $D^\pm$ meson the χ^2 and S_l cuts were changed to 8 and 1, respectively. After selection the D^0 candidates were separated into two groups; the "ΔM tag" group consists of D^0 candidates which were combined with a third track that could be a "soft" pion (π_s) in a $D^{*\pm} \rightarrow D^0\pi_s^\pm$ decay. The soft pion must have $p_T > 0.12\,\mathrm{GeV}$ and charge opposite to that of the kaon. For D^0 mesons not coming from a $D^{*\pm}$, the incorrect assignment of the pion and kaon masses produces a wider reflected signal. The distribution of this reflection was estimated using the D^0 candidates with a ΔM tag and, after normalising it to the ratio of numbers of D^0 mesons with and without a ΔM tag it was subtracted from the untagged D^0 candidates. Figure 7.6 shows the $M(K\pi)$ distributions for tagged and untagged D^0 candidates. The distributions were fitted simultaneously assuming that both have the same shape and, like the $D^\pm$, were described by a modified Gaussian function. The number of untagged (tagged) D^0 mesons yielded by the fit was $N^{\mathrm{untag}}(D^0) = 6584\pm345$ ($N^{\mathrm{tag}}(D^0) = 1690\pm70$).

Again, a sample of D^0 candidates with $p_T^{\pi,K} > 0.8\,\mathrm{GeV}$ and $p_T^{D^0} > 3\,\mathrm{GeV}$ was used to obtain the lifetime of the D^0 meson; the $M(K\pi)$ distribution is shown in figure 7.7. The higher p_T cuts were used to obtain a clean signal with no requirements made on the significance of the decay length. The number of untagged (tagged) D^0 mesons yielded by the fit was $N^{\mathrm{untag}}(D^0) = 5612 \pm 283$ ($N^{\mathrm{tag}}(D^0) = 1495 \pm 56$).

The reconstructed invariant mass distributions used in the analyses $D^\pm$ and D^0 analysis are included in Appendix B.
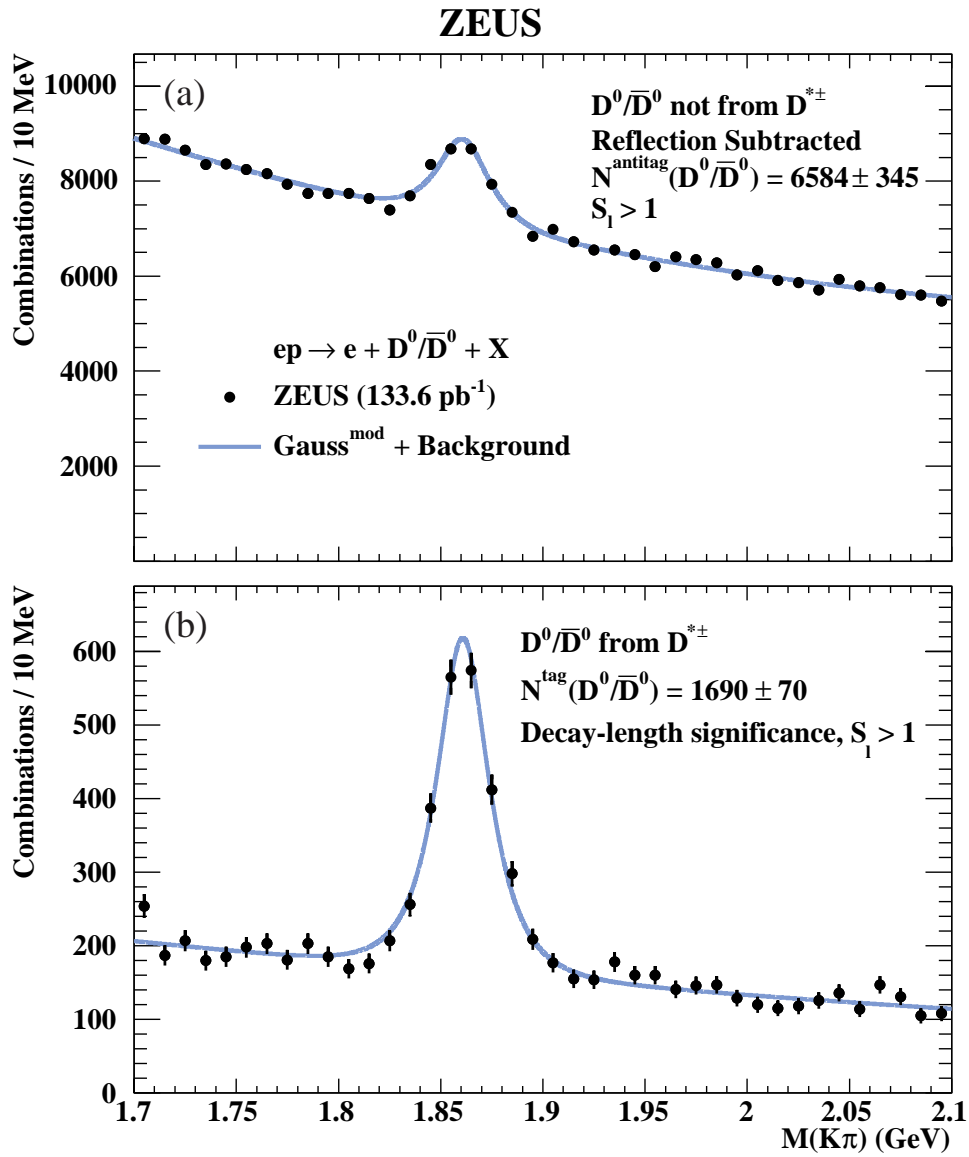
Figure 7.6: *The $M(K\pi)$ distributions (dots) for (a) D^0 candidates without a ΔM tag, obtained after the reflection subtraction (see text) and (b) D^0 candidates with a ΔM tag. The solid curves represent a fit to the sum of a modified Gaussian function and a second order polynomial background function.*
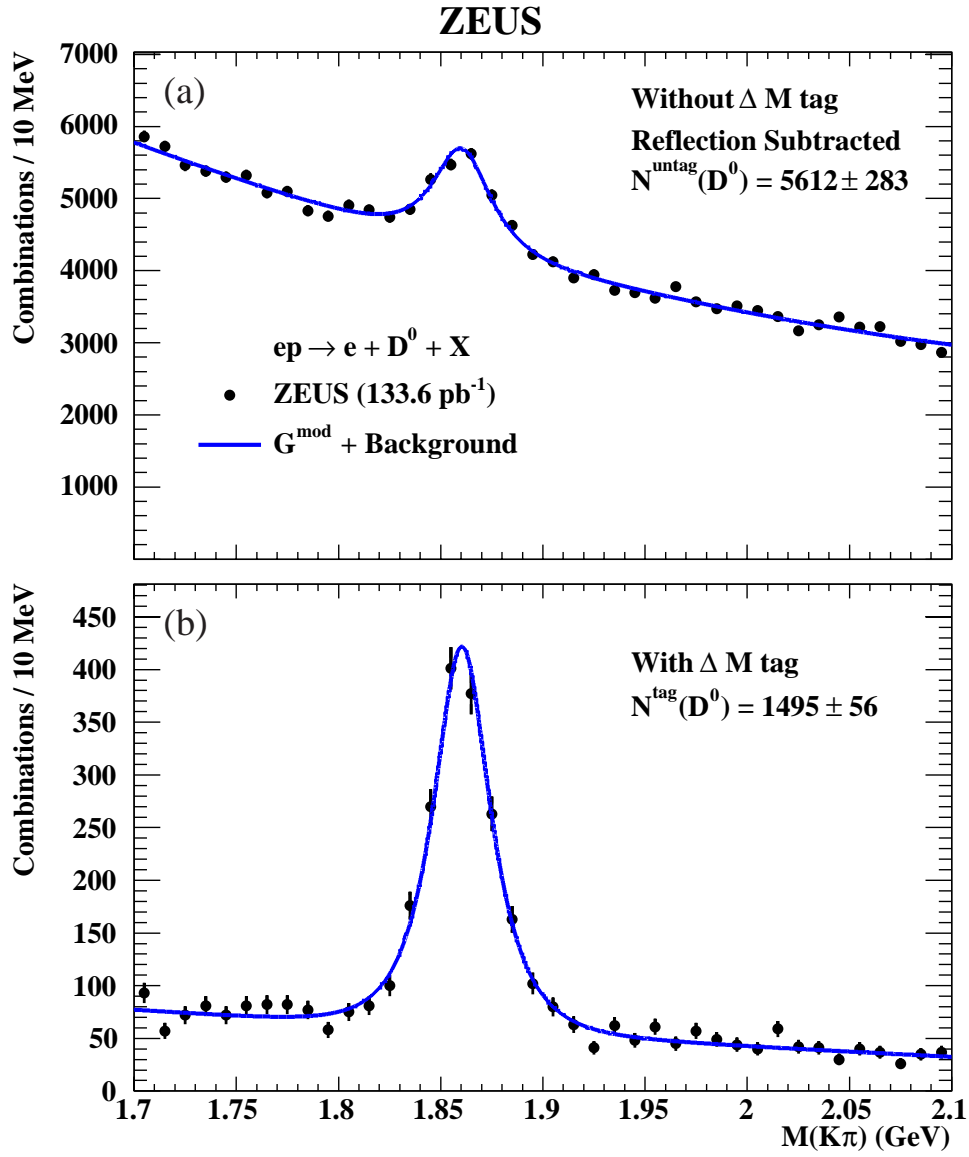
Figure 7.7: *The $M(K\pi)$ distributions (dots) for (a) D^0 lifetime candidates without a ΔM tag, obtained after the reflection subtraction (see text) and (b) D^0 candidates with a ΔM tag. The solid curves represent a fit to the sum of a modified Gaussian function and a second order polynomial background function.*

7.3   Evaluation of systematic uncertainties

7.3.1   Experimental uncertainties

The systematic uncertainties of the measured cross sections were determined by changing the analysis procedure and repeating all calculations. A complete table of systematic uncertainties for all total and differential cross sections can be found in Appendix C. The following possible sources of systematic uncertainty were considered.

EMC scale

The effect of the uncertainty in the EMC scale was evaluated by scaling the energy of the scattered electron by $\pm 2\%$ in the MC. The average effect on the total cross section was $<1\%$.

HAC scale

The effect of the uncertainty in the HAC scale was evaluated by scaling the energy of the hadronic system by $\pm 3\%$ in the MC. The average effect on the total cross section was $<1\%$.

y_{el} description

The uncertainty from the MC description of y_{el} was evaluated by varying the cut by ± 0.04 from the nominal 0.95 value. The average effect on the total cross section was $<1\%$.

y_{JB} description

The uncertainty from the MC description of y_{JB} was evaluated by varying the cut by $^{+0.04}_{-0.02}$ from the nominal 0.02 value. The average effect on the total cross section

was $^{+0.3\%}_{-3.0\%}$.

$E - p_z$ description

The uncertainty from the MC description of $\delta = E - p_Z$ was evaluated by varying the width of the allowed range by ± 6 GeV from the nominal $40 < \delta < 65$ GeV range. The average effect on the total cross section was $<1\%$.

z_{vtx} description

The uncertainty from the MC description of the primary vertex z position, z_{vtx}, was evaluated by varying the allowed range by ± 5 cm from the nominal $|z_{\mathrm{vtx}}| < 50$ cm. The average effect of the total cross section was $<1\%$.

$E_{e'}$ description

The uncertainty from the MC description of the scattered electron energy, $E_{e'}$, was evaluated by varying the cut by ± 1 GeV from the nominal 10 GeV value. The average effect on the total cross section was $^{+1.1\%}_{-0.6\%}$.

Description of scattered electron position in the RCAL

The uncertainty from the MC description of the scattered electron position was evaluated by varying the size of the allowed region in the RCAL by ± 1 cm in the x and y directions. The average effect on the total cross section was $<1\%$.

b quark contribution to MC sample

The uncertainty from the MC b component was evaluated by increasing and decreasing the size of this component by a factor 2 in the reference MC sample. The average effect on the total cross section was $^{+1.3\%}_{-1.7\%}$.

Simulation of track reconstruction

The uncertainty from the simulation of the track reconstruction was found by varying the momenta of all tracks by $\pm$ 0.3 %, which corresponds to the uncertainty in the magnetic field, and by changing the track momentum and angular resolutions by $^{+20\%}_{-10\%}$ of their values. The asymmetric variations were used since MC signals typically had narrower widths than those observed in data. The average effect on the total cross section from these sources combined was $\pm$ 1%.

Description of MVD hit efficiency

The uncertainty from the MC description of the MVD hit efficiency was found by evaluating the difference between data and MC efficiencies for tracks to be reconstructed with $2r\phi$ and $2z\phi$ hits associated. Efficiency is used to mean the fraction of tracks remaining from a sample with similar cuts to those used to reconstruct the D meson candidates after the requirement of MVD hits is imposed. The uncertainty of 0.4% per track was added linearly for the number of tracks used for the candidate reconstruction and the average effect on the total cross section was $\pm$ 1%.

S_l description

The uncertainty from the MC description of S_l was evaluated by examining the behaviour of the MC and data as cuts on S_l and σ_l were introduced and gradually raised [57]. Figures 7.8 and 7.9 show the description of the efficiency in the data by the MC along with the relative difference between the data and MC. The dashed lines on the figures represent a reasonable value for the maximum deviation between data and MC before the statistical precision of the measurements becomes a problem at higher values of σ_l. This maximum difference from the σ_l cuts is propagated to the S_l description and used to derive cut variations as shown in
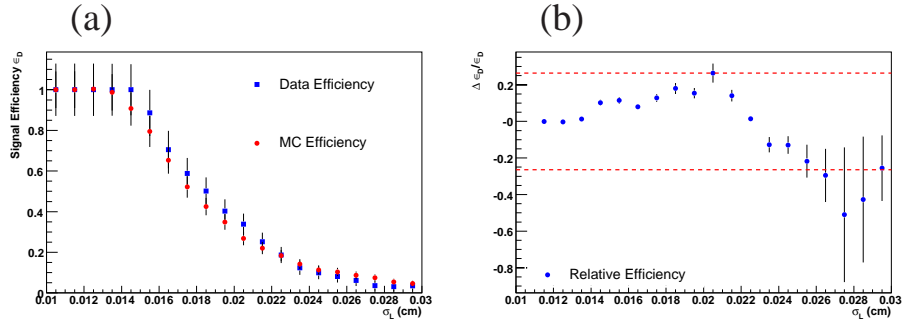
Figure 7.8: $D^\pm$ *meson (a) data and MC values of efficiency for given cuts on σ_l and (b) relative difference between data and MC efficiency.*
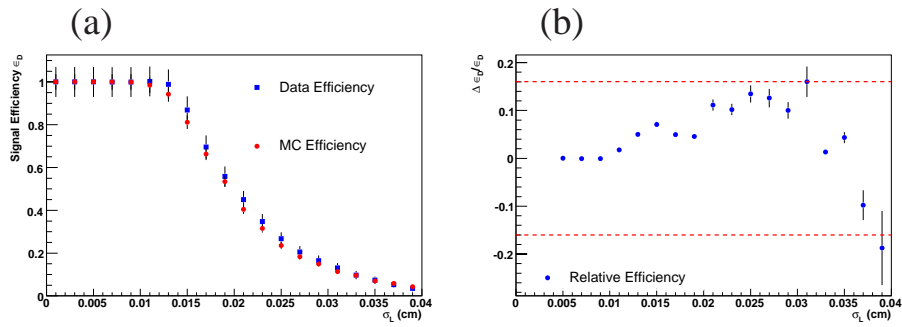
Figure 7.9: D^0 *meson (a) data and MC values of efficiency for given cuts on σ_l and (b) relative difference between data and MC efficiency.*

figure 7.10. The propagation results in the efficiency of the S_l cut being varied by the maximum deviation in the σ_l description. The cut variations obtained with this method were $\pm$ 1 and $\pm$ 0.4 for the $D^\pm$ and D^0 analysis respectively resulting in an average effect on the total cross section of $^{+6\%}_{-7\%}$. In some differential bins the effect from the cut variation is found to be greater than the maximum deviation between data and MC. This is attributed to statistical fluctuations and these bins are assigned an uncertainty equal to the maximum deviation between data and MC for σ_l.
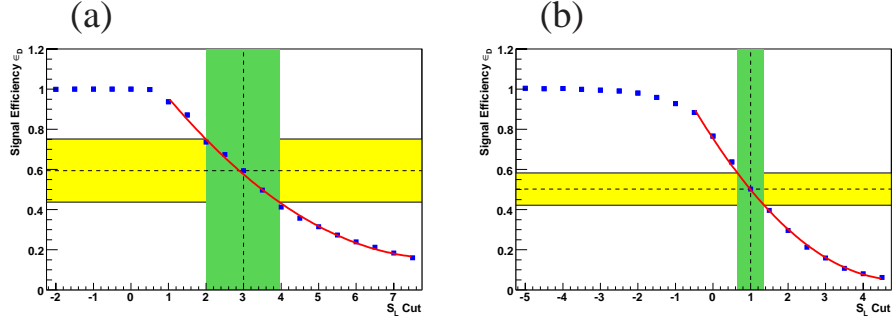
Figure 7.10: *Efficiency of the S_l cut in data (points) for the (a) $D^{\pm}$ and (b) D^0 analyses. The yellow and green shaded bands represent the uncertainty on the σ_q and S_l descriptions respectively. The red line shows a second order polynomial fitted to the data.*

χ^2 description

The uncertainty from the description of the secondary vertex χ^2 was found by evaluating the relative difference between data and MC as the χ^2 cut is gradually increased. This difference is then propagated to obtain cut variations which are used to evaluate the systematic uncertainty. The average effect on the total cross section was $^{+2\%}_{-1\%}$.

p_T^D and η^D description

The uncertainties from the MC description of p_T^D and η^D were evaluated by reshaping the generator level distribution in the MC according to the difference at the reconstructed level between data and MC for the relevant variable. The total number of generated D mesons was kept as a constant and the effect of the reshaping was propagated to the reconstructed level through the known acceptance corrections. As the total number of generated and reconstructed D mesons was a constant the effect on the total cross sections was zero, although there was an average effect in the differential cross sections of 5% for both the p_T^D and η^D cases.

125

Weighting procedure uncertainty

This is the uncertainty from the correction described in section 6.3.1 and as such is associated to the MC correction method. The average effect on the total cross section was found to be <1%.

Background parametrisation

The uncertainty due to the choice of background parametrisation was found by using an exponential in both the $D^\pm$ and D^0 case. The average effect on the total cross section was $\pm$ 5%.

Extraction of $N^{\mathrm{tag}}(D^0)$

This source of uncertainty was considered for the D^0 case only. The wrong charge subtraction method [58] was used to extract the number of tagged D^0 mesons for the purposes of reflection subtraction. The effect on the total cross section was <1%.

7.3.2   Theoretical uncertainties

The NLO predictions from HVQDIS as detailed in section 2.2.1 are subject to theoretical uncertainties and the sources considered are outlined below

The ZEUS PDF uncertainty

The ZEUS PDF uncertainties propagated from the experimental uncertainties were considered by using the upper and lower bound of the PDF fit. The effect on the total cross section was $\pm$5%. The change in the cross section was independent of the kinematic region.

126

Charm quark mass, m_c

The uncertainty in the charm quark mass was evaluated by changing the charm mass by $\pm 0.15\,\text{GeV}$ consistently in the PDF and HVQDIS. The effect on the total cross section was $\mp 8\%$.

Renomalisation and facorisation scale, μ

The uncertainty from the choice of μ was evaluated by varying the HVQDIS input value to $2\sqrt{Q^2 + 4m_c^2}$ and $\sqrt{Q^2/4 + m_c^2}$. The effect on the total cross section was $^{+7\%}_{-0\%}$.

Peterson parameter, ϵ

The uncertainty from the choice of ϵ was evaluated by varying the HVQDIS input value by $^{+0.035}_{-0.015}$ from the central value of 0.035. The larger upward variation is used in order to ensure consistency with as yet unpublished ZEUS results [59].The effect on the total cross section was $^{+5\%}_{-7\%}$.

7.4 D meson lifetimes

Lifetimes for the $D^{\pm}$ and D^0 mesons were calculated using reconstructed D meson signals in the kinematic region $5 < Q^2 < 1000\,\text{GeV}^2$, $0.02 < y < 0.7$, $3 < p_T^D < 15\,\text{GeV}$ and $|\eta^D| < 1.6$. No MC-based unfolding procedure is necessary as the detector acceptance is uniform with respect to the displacement of the secondary vertex and the normalisation of the lifetime distribution is irrelevant. The number of D mesons in a given bin of proper time, $c\tau$, was extracted and the distribution fitted with the function;

$$f(ct) = \frac{1}{2\lambda} e^{-\left(\frac{ct}{\lambda} - \frac{\sigma^2}{2\lambda^2}\right)} \int_{u_{\min}}^{\infty} e^{-u^2}\, du \tag{7.1}$$

127

where $u_{\min} = (-ct/\sigma + \sigma/\lambda)$, λ is the lifetime and σ is the proper time resolution. This function represents an exponential decay convoluted with a Gaussian resolution. The spatial resolution of the ZEUS tracking was found to be 120 μm with the tagged D^0 sample. This value was then used as an input to the fitting function used to extract the lifetimes.

The fitted $c\tau$ distributions for $D^\pm$ and D^0 mesons are shown in figure 7.11 and the extracted values for the lifetimes were:

$$
\begin{aligned}
c\tau(D^\pm) &= 326 \pm 21\,(\text{stat.})\,\mu\text{m} \\
c\tau(D^0) &= 132 \pm 7\,(\text{stat.})\,\mu\text{m}
\end{aligned}
$$

The systematic uncertainties are significantly smaller than the statistical uncertainty as the measurment has only a small dependence on the details of the MC simulation. The values are consistent with the world average values of $311.8 \pm 2.1\,\mu$m and $122.9 \pm 0.5\,\mu$m [19] for the $D^\pm$ and D^0, respectively.
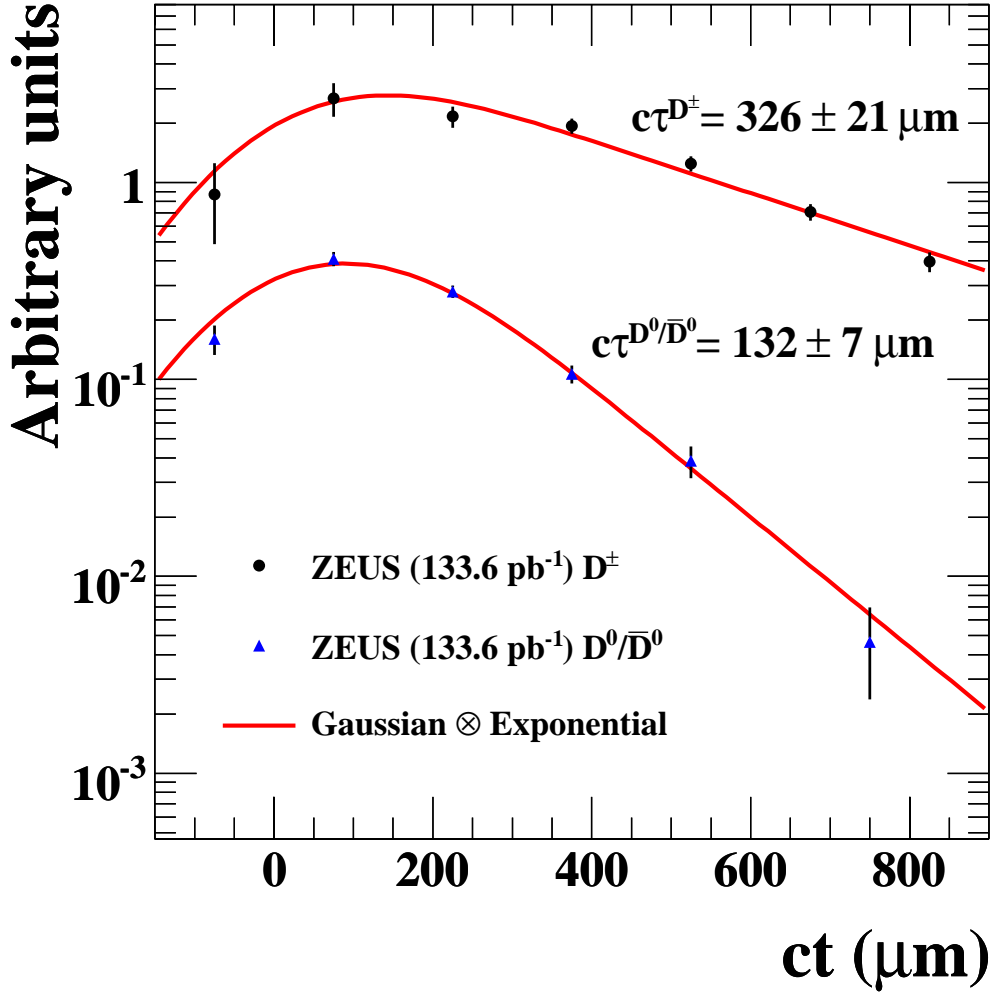
Figure 7.11: *The distribution of reconstructed $D^\pm$ (circle) and D^0 (triangle) mesons extracted in bins of proper time, $c\tau$, shown on a logarithmic scale. Both histograms are fitted with functions described by a Gaussian convoluted with an exponential decay. The $D^\pm$ and D^0 distributions are normalised such that they are visually separated.*

Chapter 8

Results

8.1 Total cross sections

Charm–meson cross sections for the process $ep \to eDX$ were calculated using the reconstructed $D^\pm$ and D^0 signals in the kinematic region $5 < Q^2 < 1000\,\mathrm{GeV}^2$, $0.02 < y < 0.7$, $1.5 < p_T^D < 15\,\mathrm{GeV}$ and $|\eta^D| < 1.6$.

The following cross sections were measured:

- The production cross section for $D^\pm$ mesons is:

$$\sigma(D^\pm) = 4.67 \pm 0.26 \,(\text{stat.}) \,^{+0.38}_{-0.56}\,(\text{syst.}) \pm 0.17(\text{br.}) \pm 0.12(\text{lumi.})\ \mathrm{nb}$$

- The production cross section for D^0 mesons not originating from the $D^{*\pm} \to D^0 \pi_s$ decays, hereafter referred to as untagged D^0 mesons, is:

$$\sigma^{\text{untag}}(D^0) = 7.49 \pm 0.46 \,(\text{stat.}) \,^{+0.98}_{-0.58}\,(\text{syst.}) \pm 0.14(\text{br.}) \pm 0.20(\text{lumi.})\ \mathrm{nb}$$

The corresponding predictions from the HVQDIS program are:

$$\sigma(D^\pm) \quad = \quad 4.42\,^{+0.86}_{-0.62}\,(\text{syst.}) \,^{+0.42}_{-0.60}\,(\text{had.})\ \mathrm{nb}$$

$$\sigma^{\text{untag}}(D^0) \quad = \quad 9.25\,^{+1.79}_{-1.29}\,(\text{syst.}) \,^{+0.52}_{-0.96}\,(\text{had.})\ \mathrm{nb}$$

where "had." represents the uncertainty on the NLO prediction due to the uncertainty of the hadronisation fraction $f(c \rightarrow D)$. The HVQDIS predictions are in agreement with the data. The predictions used the default parameter settings as discussed in section 2.2.1 and employ the hadronisation fractions previously measured at ZEUS [20]. The quadratic sum of the uncertainties of these predictions is shown with the "syst" label, and is dominated by the change of the charm quark mass. A small contribution ($\sim 2\%$) to the total cross sections arises from D mesons produced in $b\bar{b}$ events. Therefore, all NLO predictions include a $b\bar{b}$ contribution calculated in each bin with the HVQDIS program as described in section 2.2.1.

8.2 Differential cross sections

The differential $D^{\pm}$ and D^0 cross sections as a function of Q^2, x, p_T^D and η^D are shown in Figs. 8.1 and 8.2 and given in Tables 8.1 and 8.2. The cross sections in Q^2 and x both fall by about three orders of magnitude in the measured region. The cross section in p_T^D falls by about two orders of magnitude and there is no significant dependence on η^D. Double differential $D^{\pm}$ and D^0 cross sections as a function of p_T^D and η^D are shown in figure 8.3 and given in Table 8.3. The cross section falls by two orders of magnitude in the kinematic region measured. In all cross sections the NLO prediction describes the data well.

8.3 Extraction of $F_2^{c\bar{c}}$

The open charm contribution, $F_2^{c\bar{c}}$, to the proton structure function, F_2, can be defined in terms of the inclusive double–differential $c\bar{c}$ cross section in x and Q^2

Q^2 bin (GeV^2)	$d\sigma/dQ^2$	Δ_{stat}	Δ_{syst}
	(nb/GeV^2)		
5, 10	0.35	± 0.04	$^{+0.04}_{-0.05}$
10, 20	0.13	± 0.01	$^{+0.01}_{-0.01}$
20, 40	0.048	± 0.005	$^{+0.012}_{-0.005}$
40, 80	0.013	± 0.002	$^{+0.001}_{-0.002}$
80, 200	0.0020	± 0.0004	$^{+0.0002}_{-0.0006}$
200, 1000	0.00010	± 0.00004	$^{+0.00004}_{-0.00005}$
x bin	$d\sigma/dx$	Δ_{stat}	Δ_{syst}
	(nb)		
0.00008, 0.0004	3773	± 566	$^{+581}_{-775}$
0.00040, 0.0016	1643	± 136	$^{+184}_{-129}$
0.0016, 0.005	327	± 33	$^{+40}_{-42}$
0.005, 0.01	55	± 11	$^{+9}_{-19}$
0.01, 0.1	1.5	± 0.5	$^{+0.2}_{-0.5}$
$p_T^{D^\pm}$ bin (GeV)	$d\sigma/dp_T^{D^\pm}$	Δ_{stat}	Δ_{syst}
	(nb/GeV)		
1.5, 2.4	2.63	± 0.50	$^{+0.59}_{-0.87}$
2.4, 3.1	1.37	± 0.17	$^{+0.10}_{-0.20}$
3.1, 4.0	0.73	± 0.07	$^{+0.06}_{-0.04}$
4.0, 6.0	0.32	± 0.03	$^{+0.03}_{-0.03}$
6.0, 15.0	0.032	± 0.003	$^{+0.003}_{-0.003}$
$\eta^{D^\pm}$ bin	$d\sigma/d\eta^{D^\pm}$	Δ_{stat}	Δ_{syst}
	(nb)		
-1.6, -0.8	1.05	± 0.16	$^{+0.32}_{-0.11}$
-0.8, -0.4	1.35	± 0.17	$^{+0.18}_{-0.17}$
-0.4, 0.0	1.76	± 0.22	$^{+0.24}_{-0.22}$
0.0, 0.4	1.37	± 0.17	$^{+0.22}_{-0.19}$
0.4, 0.8	1.70	± 0.23	$^{+0.22}_{-0.40}$
0.8, 1.6	1.62	± 0.27	$^{+0.29}_{-0.40}$

Table 8.1: *Measured $D^\pm$ cross sections as a function of Q^2, x, $p_T^{D^\pm}$ and $\eta^{D^\pm}$ for $5 < Q^2 < 1000$ GeV^2, $0.02 < y < 0.7$, $1.5 < p_T^{D^\pm} < 15$ GeV and $|\eta^{D^\pm}| < 1.6$. The statistical and systematic uncertainties are shown separately. The cross sections have further uncertainties of 3.5% from the $D^\pm \to K^\mp \pi^\pm \pi^\pm$ branching ratio, and 2.6% from the uncertainty in the luminosity measurement.*

Q^2 bin (GeV^2)	$d\sigma/dQ^2$	Δ_{stat}	Δ_{syst}
	(nb/GeV^2)		
5, 10	0.52	$\pm\,0.07$	$^{+0.08}_{-0.04}$
10, 20	0.23	$\pm\,0.02$	$^{+0.02}_{-0.02}$
20, 40	0.067	$\pm\,0.008$	$^{+0.007}_{-0.008}$
40, 80	0.021	$\pm\,0.003$	$^{+0.003}_{-0.003}$
80, 1000	0.0010	$\pm\,0.0003$	$^{+0.0003}_{-0.0002}$
x bin	$d\sigma/dx$	Δ_{stat}	Δ_{syst}
	(nb)		
0.00008, 0.0004	4697	$\pm\,824$	$^{+769}_{-743}$
0.00040, 0.0016	2896	$\pm\,254$	$^{+235}_{-225}$
0.0016, 0.005	527	$\pm\,54$	$^{+41}_{-55}$
0.005, 0.1	10	$\pm\,2$	$^{+4}_{-2}$
$p_T^{D^0}$ bin (GeV)	$d\sigma/dp_T^{D^0}$	Δ_{stat}	Δ_{syst}
	(nb/GeV)		
1.5, 2.4	2.90	$\pm\,0.45$	$^{+0.26}_{-0.26}$
2.4, 3.1	2.49	$\pm\,0.31$	$^{+0.29}_{-0.32}$
3.1, 4.0	1.35	$\pm\,0.15$	$^{+0.14}_{-0.17}$
4.0, 6.0	0.53	$\pm\,0.05$	$^{+0.03}_{-0.02}$
6.0, 15.0	0.058	$\pm\,0.007$	$^{+0.012}_{-0.009}$
η^{D^0} bin	$d\sigma/d\eta^{D^0}$	Δ_{stat}	Δ_{syst}
	(nb)		
-1.6, -0.8	1.42	$\pm\,0.29$	$^{+0.25}_{-0.23}$
-0.8, -0.4	2.87	$\pm\,0.39$	$^{+0.41}_{-0.37}$
-0.4, 0.0	2.36	$\pm\,0.30$	$^{+0.30}_{-0.43}$
0.0, 0.4	2.68	$\pm\,0.36$	$^{+0.42}_{-0.16}$
0.4, 0.8	3.18	$\pm\,0.42$	$^{+0.34}_{-0.36}$
0.8, 1.6	1.81	$\pm\,0.33$	$^{+0.35}_{-0.27}$

Table 8.2: *Measured cross sections for D^0 not coming from a D^* as a function of Q^2, x, $p_T^{D^0}$ and η^{D^0} for $5 < Q^2 < 1000$ GeV^2, $0.02 < y < 0.7$, $1.5 < p_T^{D^0} < 15$ GeV and $|\eta^{D^0}| < 1.6$. The statistical and systematic uncertainties are shown separately. The cross sections have further uncertainties of 1.9% from the $D^0 \to K^\mp\pi^\pm$ branching ratio, and 2.6% from the uncertainty in the luminosity measurement.*

$\eta^{D^\pm}$ bin	$p_T^{D^\pm}$ bin (GeV)	$d\sigma/dp_T^{D^\pm}d\eta^{D^\pm}$	Δ_{stat}	Δ_{syst}
		(nb/GeV)		
	1.5, 4.0	0.44	$\pm\,0.05$	$^{+0.04}_{-0.08}$
$\eta < 0$	4.0, 6.0	0.09	$\pm\,0.01$	$^{+0.02}_{-0.01}$
	6.0, 15.0	0.007	$\pm\,0.001$	$^{+0.001}_{-0.001}$
	1.5, 4.0	0.53	$\pm\,0.07$	$^{+0.05}_{-0.11}$
$\eta > 0$	4.0, 6.0	0.10	$\pm\,0.01$	$^{+0.01}_{-0.01}$
	6.0, 15.0	0.015	$\pm\,0.002$	$^{+0.002}_{-0.003}$
η^{D^0} bin	$p_T^{D^0}$ bin (GeV)	$d\sigma/dp_T^{D^0}d\eta^{D^0}$	Δ_{stat}	Δ_{syst}
		(nb/GeV)		
	1.5, 4.0	0.67	$\pm\,0.07$	$^{+0.07}_{-0.10}$
$\eta < 0$	4.0, 6.0	0.15	$\pm\,0.02$	$^{+0.02}_{-0.02}$
	6.0, 15.0	0.018	$\pm\,0.003$	$^{+0.004}_{-0.004}$
	1.5, 4.0	0.81	$\pm\,0.09$	$^{+0.11}_{-0.05}$
$\eta > 0$	4.0, 6.0	0.18	$\pm\,0.02$	$^{+0.02}_{-0.01}$
	6.0, 15.0	0.020	$\pm\,0.003$	$^{+0.005}_{-0.005}$

Table 8.3: *Measured cross sections for $D^\pm$ and D^0 not coming from a D^* in each of the η^D and p_T^D bins for $5 < Q^2 < 1000$ GeV^2, $0.02 < y < 0.7$, $1.5 < p_T^D < 15$ GeV and $|\eta^D| < 1.6$. The statistical and systematic uncertainties are shown separately. The $D^\pm$ and D^0cross sections have further uncertainties of 3.5% and 1.9% from the $D^\pm \to K^\mp\pi^\pm\pi^\pm$ and $D^0 \to K^\mp\pi^\pm$ branching ratios respectively. The additional uncertainty from the luminosity measurements is 2.6%*

ZEUS
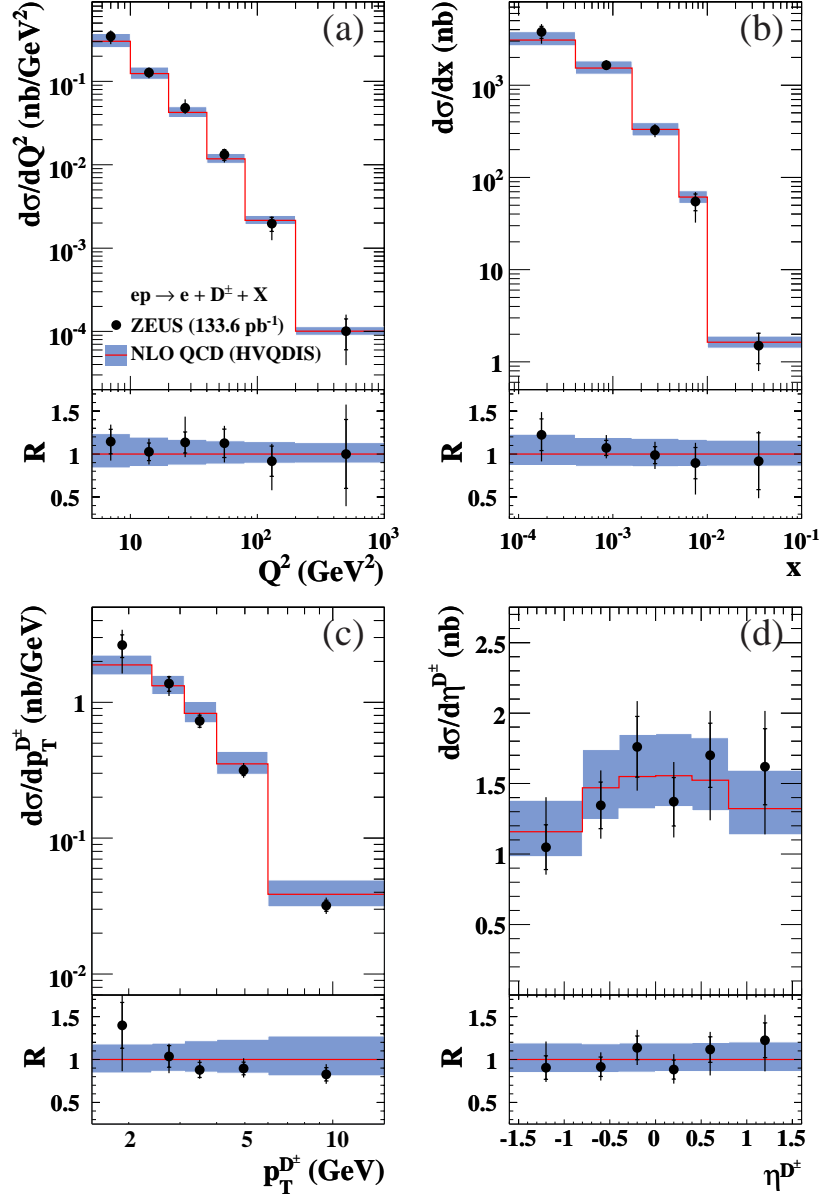
Figure 8.1: *Differential cross sections for $D^\pm$ mesons as a function of (a) Q^2, (b) x, (c) $p_T^{D^\pm}$ and (d) $\eta^{D^\pm}$ compared to the NLO QCD predictions of HVQDIS. Statistical uncertainties are shown by the inner error bars. Statistical and systematic uncertainties added in quadrature are shown by the outer error bars with the shaded region representing the uncertainty of the HVQDIS prediction. The ratios, R, of the cross sections to the central HVQDIS prediction are also shown in the lower section of each plot.*

135

ZEUS
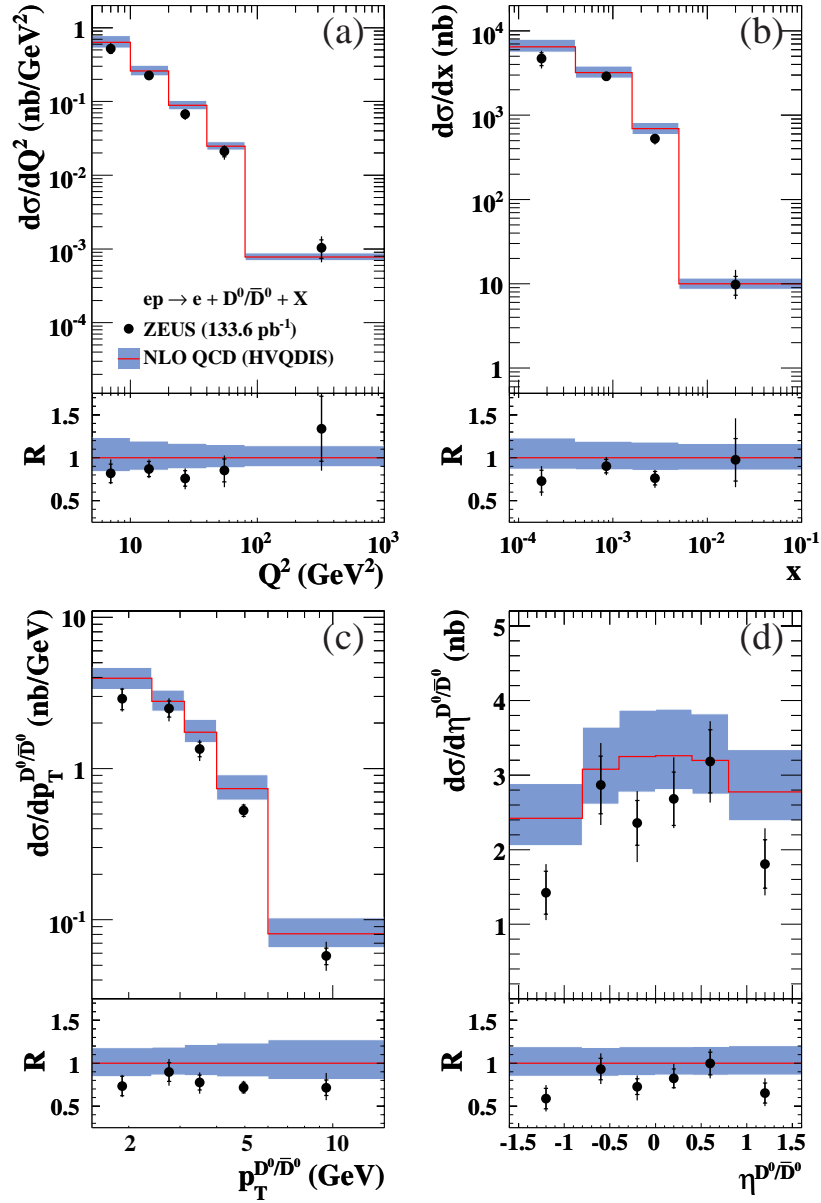
Figure 8.2: *Differential cross sections for $D^0/\bar{D}^0$ mesons not from $D^{*\pm}$ decay as a function of (a) Q^2, (b) x, (c) $p_T^{D^0/\bar{D}^0}$ and (d) $\eta^{D^0/\bar{D}^0}$ compared to the NLO QCD predictions of HVQDIS. Statistical uncertainties are shown by the inner error bars. Statistical and systematic uncertainties added in quadrature are shown by the outer error bars with the shaded region representing the uncertainty of the HVQDIS prediction. The ratios, R, of the cross sections to the central HVQDIS prediction are also shown in the lower section of each plot.*

136

ZEUS
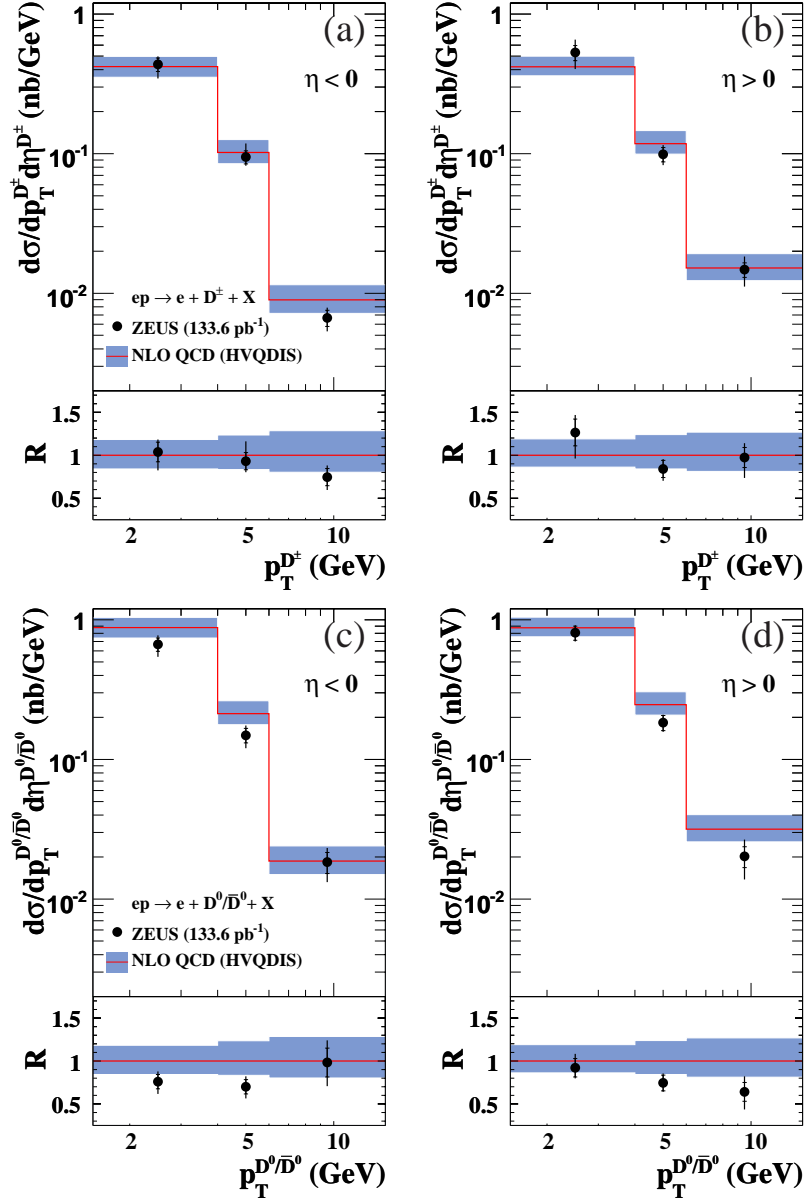
Figure 8.3: *Double-differential $D^{\pm}$ and D^0 cross sections as a function of p_T^D and η^D compared to the NLO QCD predictions of HVQDIS. Statistical uncertainties are shown by the inner error bars. Statistical and systematic uncertainties added in quadrature are shown by the outer error bars with the shaded region representing the uncertainty of the HVQDIS prediction. The ratios, R, of the cross sections to the central HVQDIS prediction are also shown in the lower section of each plot.*

137

by

$$\frac{d^2\sigma^{c\bar{c}}(x, Q^2)}{dxdQ^2} = \frac{2\pi\alpha^2}{xQ^4}\left\{\left[1 + (1 - y)^2\right]F_2^{c\bar{c}}(x, Q^2) - y^2 F_L^{c\bar{c}}(x, Q^2)\right\} \quad (8.1)$$

The $c\bar{c}$ cross section is obtained by measuring the $D^\pm$ and D^0 production cross sections and employing the hadronisation fraction $f(c \to D)$ to derive the total charm cross section. A limited kinematic region is accessible for the measurement of D mesons; therefore a prescription for extrapolating to the full kinematic phase space is needed. Thus, the measured value of $F_2^{c\bar{c}}$ in a bin i is given by:

$$F_{2,\text{meas}}^{c\bar{c}}(x_i, Q_i^2) = \frac{\sigma_{i,\text{meas}}(ep \to eDX)}{\sigma_{i,\text{theo}}(ep \to eDX)}F_{2,\text{theo}}^{c\bar{c}}(x_i, Q_i^2) \quad (8.2)$$

where σ_i is the cross section in bin i for the measured region of p_T^D and η^D. The cross sections $\sigma_{i,\text{meas}}(ep \to eDX)$ were measured in Q^2 and y kinematic bins (Table 8.4) corresponding to the Q^2 and x values shown in Table 8.5 where the $F_2^{c\bar{c}}$ results are also given. The value of $F_{2,\text{theo}}^{c\bar{c}}$ was calculated from the NLO coefficient functions [60]. The functional form of $F_{2,\text{theo}}^{c\bar{c}}$ was used to quote the results for $F_2^{c\bar{c}}$ at convenient values of x and Q^2 close to the centre of gravity of the bin. In this calculation, the same parton densities, charm mass ($m_c = 1.5\,\text{GeV}$), and factorisation and renormalisation scales ($\mu = \sqrt{Q^2 + 4m_c^2}$) were used as for the HVQDIS calculation. The hadronisation was performed using the Peterson fragmentation function. The beauty contribution was subtracted from the data using the value obtained from HVQDIS. The contribution to the total cross section from $F_L^{c\bar{c}}$ calculated using the ZEUS NLO fit is, on average, 1.3% and at most 4.7% [25] and is taken into account in the extraction of $F_2^{c\bar{c}}$. The size of the contribution from F_L is similar to that in other PDFs.

The following uncertainties associated with the method of extrapolation have been evaluated:

- changing the charm mass by $\pm 0.15\,\text{GeV}$ consistently in the HVQDIS

138

calculation and in the calculation of $F^{c\bar{c}}_{2,\text{theo}}$ gives an average difference in the extrapolated result of $\pm 2\%$;

- using the upper and lower predictions given by the uncertainty in the ZEUS NLO PDF fit, propagated from the experimental uncertainties of the fitted data, to perform the extraction of $F^{c\bar{c}}_2$ gives an average difference in the extracted result of $< 1\%$;

- changing the contribution of beauty events subtracted from the data by a factor 2 gives an average difference in the extracted result of $^{+1\%}_{-2\%}$ with up to $^{+3\%}_{-7\%}$ at low x and high Q^2;

- the JETSET fragmentation as implemented in the previous analyses [20, 25, 61] was used instead of the Peterson fragmentation. This gives an average difference in the extracted result of $\pm 7\%$ with up to $\pm 14\%$ seen at high x, low Q^2.

The $F^{c\bar{c}}_2$ values measured from $D^{\pm}$ and D^0 decay are combined using a procedure that accounts for the systematic and point to point correlations between the analyses [62]. The separate and combined values of $F^{c\bar{c}}_2$ obtained from $D^{\pm}$ and D^0 production are shown in figures 8.4 and 8.5; also shown is the ZEUS NLO QCD fit which describes the data well for all Q^2 and x. The uncertainty of the theoretical prediction is that from the charm mass. Due to the improved statistical precision resulting from lifetime tags with the MVD more measurements of $F^{c\bar{c}}_2$ were extracted with a higher precision than was previously possible with $D^{\pm}$ and D^0 mesons at ZEUS. The measured values of $F^{c\bar{c}}_2$ agree with, and improve upon, previous results from ZEUS with these D mesons. At high Q^2 more values of $F^{c\bar{c}}_2$ are extracted and these results are competitive with $D^{*\pm}$ based measurements.

Q^2 bin (GeV^2)	y bin	$\sigma(D^\pm)$	Δ_{stat}	Δ_{syst}
		(nb)		
	0.02, 0.12	0.53	± 0.13	$^{+0.18}_{-0.15}$
5, 9	0.12, 0.30	0.60	± 0.11	$^{+0.08}_{-0.17}$
	0.30, 0.70	0.57	± 0.17	$^{+0.18}_{-0.14}$
	0.02, 0.12	0.95	± 0.10	$^{+0.07}_{-0.13}$
9, 44	0.12, 0.30	0.95	± 0.09	$^{+0.07}_{-0.06}$
	0.30, 0.70	0.74	± 0.12	$^{+0.09}_{-0.20}$
	0.02, 0.12	0.20	± 0.05	$^{+0.01}_{-0.03}$
44, 1000	0.12, 0.30	0.35	± 0.06	$^{+0.05}_{-0.08}$
	0.30, 0.70	0.24	± 0.05	$^{+0.03}_{-0.06}$
Q^2 bin (GeV^2)	y bin	$\sigma(D^0)$	Δ_{stat}	Δ_{syst}
		(nb)		
	0.02, 0.12	0.83	± 0.24	$^{+0.23}_{-0.17}$
5, 9	0.12, 0.30	0.95	± 0.20	$^{+0.13}_{-0.13}$
	0.30, 0.70	0.49	± 0.17	$^{+0.12}_{-0.15}$
	0.02, 0.12	1.65	± 0.18	$^{+0.10}_{-0.13}$
9, 44	0.12, 0.30	1.41	± 0.15	$^{+0.05}_{-0.06}$
	0.30, 0.70	1.25	± 0.24	$^{+0.24}_{-0.18}$
	0.02, 0.12	0.19	± 0.09	$^{+0.06}_{-0.04}$
44, 1000	0.12, 0.30	0.54	± 0.09	$^{+0.06}_{-0.04}$
	0.30, 0.70	0.53	± 0.15	$^{+0.15}_{-0.18}$

Table 8.4: *Measured cross sections for $D^\pm$ and D^0 not coming from a D^* in each of the Q^2 and y bins for $5 < Q^2 < 1000$ GeV^2, $0.02 < y < 0.7$, $1.5 < p_T^D < 15$ GeV and $|\eta^D| < 1.6$. The statistical and systematic uncertainties are shown separately. The $D^\pm$ and D^0 cross sections have further uncertainties of 3.5% and 1.9% from the $D^\pm \to K^\mp \pi^\pm \pi^\pm$ and $D^0 \to K^\mp \pi^\pm$ branching ratios respectively. The additional uncertainty from the luminosity measurements is 2.6%*

Q^2 (GeV^2)	x	$F_2^{c\bar{c}}$	Δ_{stat}	Δ_{syst}	Δ_{extrap}	factor
	0.00022	0.295	± 0.092	$^{+0.091}_{-0.074}$	$^{+0.026}_{-0.022}$	3.2
7.0	0.00046	0.176	± 0.031	$^{+0.023}_{-0.050}$	$^{+0.010}_{-0.008}$	2.3
	0.00202	0.091	± 0.023	$^{+0.031}_{-0.026}$	$^{+0.013}_{-0.014}$	3.1
	0.00065	0.319	± 0.054	$^{+0.037}_{-0.086}$	$^{+0.022}_{-0.020}$	2.5
20.4	0.00134	0.241	± 0.024	$^{+0.017}_{-0.015}$	$^{+0.013}_{-0.013}$	1.8
	0.00588	0.131	± 0.015	$^{+0.010}_{-0.018}$	$^{+0.009}_{-0.009}$	2.4
	0.00356	0.260	± 0.058	$^{+0.030}_{-0.066}$	$^{+0.020}_{-0.025}$	1.7
112.0	0.00738	0.280	± 0.049	$^{+0.039}_{-0.065}$	$^{+0.032}_{-0.033}$	1.5
	0.03230	0.089	± 0.024	$^{+0.005}_{-0.015}$	$^{+0.002}_{-0.002}$	2.4
Q^2 (GeV^2)	x	$F_2^{c\bar{c}}$	Δ_{stat}	Δ_{syst}	Δ_{extrap}	factor
	0.00022	0.116	± 0.042	$^{+0.028}_{-0.035}$	$^{+0.010}_{-0.009}$	3.2
7.0	0.00046	0.131	± 0.029	$^{+0.019}_{-0.017}$	$^{+0.007}_{-0.006}$	2.3
	0.00202	0.068	± 0.020	$^{+0.019}_{-0.014}$	$^{+0.010}_{-0.010}$	3.1
	0.00065	0.252	± 0.051	$^{+0.049}_{-0.037}$	$^{+0.017}_{-0.016}$	2.5
20.4	0.00134	0.169	± 0.019	$^{+0.006}_{-0.007}$	$^{+0.009}_{-0.009}$	1.8
	0.00588	0.109	± 0.012	$^{+0.006}_{-0.009}$	$^{+0.007}_{-0.008}$	2.4
	0.00356	0.280	± 0.086	$^{+0.077}_{-0.096}$	$^{+0.022}_{-0.027}$	1.7
112.0	0.00738	0.203	± 0.037	$^{+0.024}_{-0.016}$	$^{+0.023}_{-0.024}$	1.5
	0.03230	0.040	± 0.019	$^{+0.012}_{-0.008}$	$^{+0.001}_{-0.001}$	2.4

Table 8.5: *The extracted values of $F_2^{c\bar{c}}$ from the production cross sections of $D^{\pm}$ and D^0 not coming from D^* at each Q^2 and x value. The statistical, systematic and extrapolation uncertainties are shown separately. The values of the extrapolation factor used to correct to the full p_T^D and η^D phase space are also shown. The values extracted from $D^{\pm}$ and D^0 have further uncertainties of 3.5% and 1.9% from the $D^{\pm} \to K^{\mp}\pi^{\pm}\pi^{\pm}$ and $D^0 \to K^{\mp}\pi^{\pm}$ branching ratios respectively. The additional uncertainty from the luminosity measurements is 2.6%*

Q^2 (GeV^2)	x	$F_2^{c\bar{c}}$	Δ_{stat}	Δ_{syst}	Δ_{extrap}
	0.00022	0.260	$\pm\,0.062$	± 0.091	$^{+0.007}_{-0.067}$
7.0	0.00046	0.157	$\pm\,0.022$	± 0.031	$^{+0.016}_{-0.035}$
	0.00202	0.088	$\pm\,0.017$	± 0.028	$^{+0.009}_{-0.016}$
	0.00065	0.291	$\pm\,0.038$	± 0.064	$^{+0.020}_{-0.094}$
20.4	0.00134	0.213	$\pm\,0.016$	± 0.014	$^{+0.018}_{-0.040}$
	0.00588	0.126	$\pm\,0.010$	± 0.014	$^{+0.010}_{-0.042}$
	0.00356	0.257	$\pm\,0.046$	± 0.057	$^{+0.020}_{-0.084}$
112.0	0.00738	0.238	$\pm\,0.030$	± 0.039	$^{+0.015}_{-0.041}$
	0.03230	0.086	$\pm\,0.020$	± 0.018	$^{+0.001}_{-0.026}$

Table 8.6: *The combined $F_2^{c\bar{c}}$ values from the production cross sections of $D^{\pm}$ and D^0 not coming from D^* at each Q^2 and x value. The statistical, systematic and extrapolation uncertainties are shown separately. The values of the extrapolation factor used to correct to the full p_T^D and η^D phase space are also shown. The values extracted from $D^{\pm}$ and D^0 have a further uncertainty of 3.3% from the $D^{\pm} \rightarrow K^{\mp}\pi^{\pm}\pi^{\pm}$ and $D^0 \rightarrow K^{\mp}\pi^{\pm}$ branching ratios. The additional uncertainty from the luminosity measurements is 2.6%*
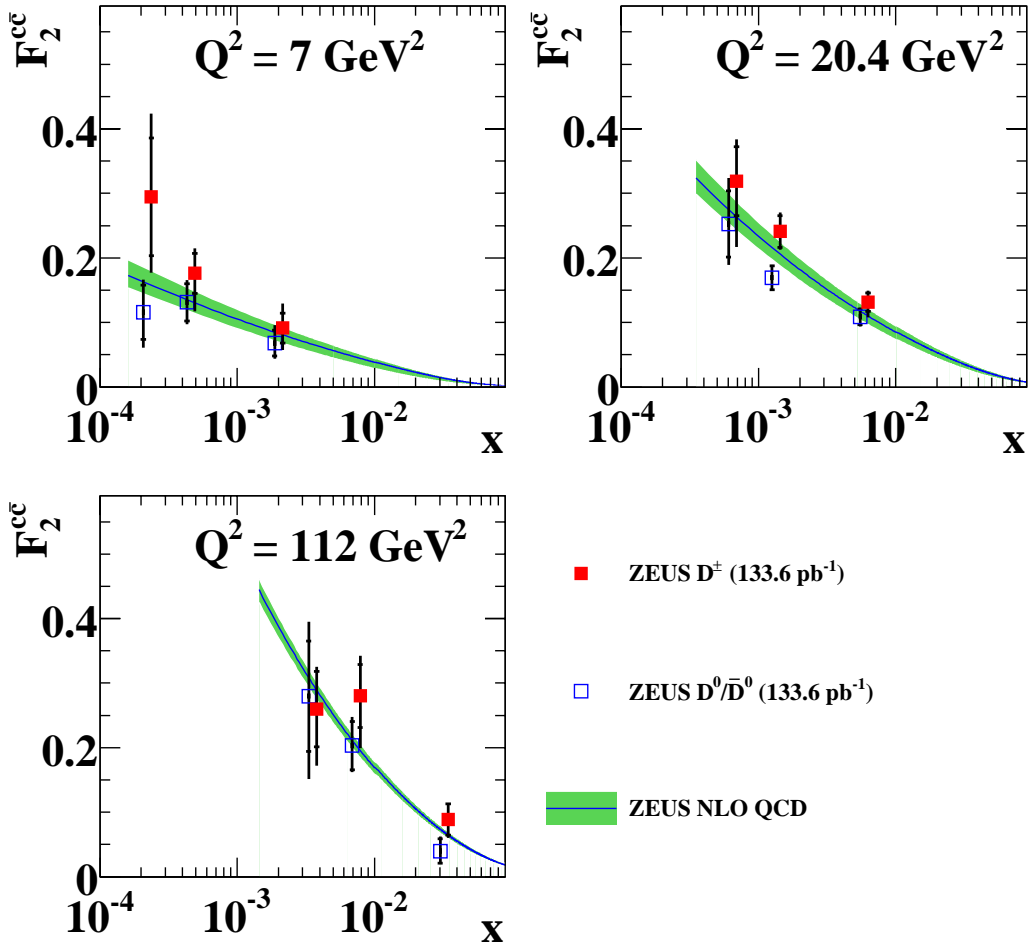
Figure 8.4: *Values of $F_2^{c\bar{c}}$ extracted from $D^{\pm}$ (squares) and D^0 (circles) as a function of x in three bins of Q^2. The data are shown with statistical uncertainties (inner bars) and statistical and systematic uncertainties added in quadrature (outer bars). The data have further uncertainties of 3.5% and 1.9% from the $D^{\pm} \rightarrow K^{\mp}\pi^{\pm}\pi^{\pm}$ and $D^0 \rightarrow K^{\mp}\pi^{\pm}$ branching ratios respectively. The additional uncertainty from the luminosity measurements is 2.6%. The shaded band shows the ZEUS NLO QCD fit charm mass uncertainty.*

ZEUS
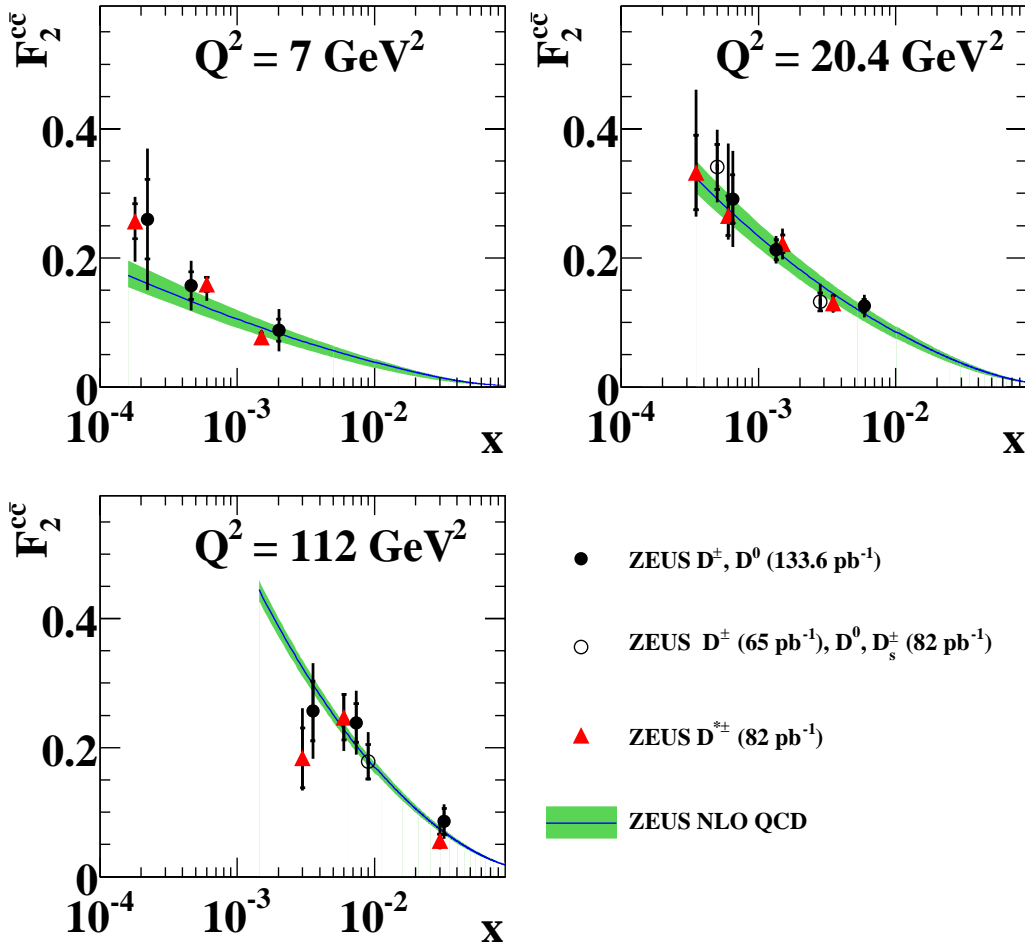
Figure 8.5: *Combined values of $F_2^{c\bar{c}}$ extracted from $D^{\pm}$ and D^0 (circles) as a function of x in three bins of Q^2. The data are shown with statistical uncertainties (inner bars) and statistical and systematic uncertainties added in quadrature (outer bars) and, where possible, are compared to previous ZEUS measurements with these mesons. The measurements have a further uncertainty of 3.3% from the $D^{\pm} \to K^{\mp}\pi^{\pm}\pi^{\pm}$ and $D^0 \to K^{\mp}\pi^{\pm}$ branching ratios. The additional uncertainty from the luminosity measurements is 2.6%. The shaded band shows the ZEUS NLO QCD fit charm mass uncertainty.*

144

8.4 Summary

The production of the charm mesons $D^{\pm}$ and D^0 has been measured with the ZEUS detector in the kinematic range $5 < Q^2 < 1000\,\mathrm{GeV}^2$, $0.02 < y < 0.7$, $1.5 < p_T^D < 15\,\mathrm{GeV}$ and $|\eta^D| < 1.6$. Combinatorial background to the D meson signals was reduced by using the ZEUS micor vertex detector to reconstruct displaced vertices.

The ZEUS micro vertex detector enables the reconstruction of decay vertices displaced from the primary by distance scales of order $100\,\mu$m. This feature was used to measure the lifetime of the $D^{\pm}$ and D^0 mesons. The measured lifetimes were found to be consistent with the world average.

The measured D meson cross sections were compared to the predictions of NLO QCD with the proton PDFs extracted from inclusive DIS data. A good description was found.

The visible cross section in bins of y and Q^2 has been used to extract the open charm contribution, $F_2^{c\bar{c}}$, to the proton structure function, F_2. The extraction was made with the NLO QCD calculation used to extrapolate outside of the measured p_T^D and η^D regions.

Through the use of the micro vertex detector, these results have increased precision and an extension in the kinematic range to lower p_T^D compared to previous ZEUS results with these mesons. Along with previous measurements of $F_2^{c\bar{c}}$, these data provide a direct constraint to the gluon density of the proton.

8.5 Potential for future improvements

The continual improvement in understanding of the track reconstruction in the ZEUS detector will directly benefit this analysis. Not only will tracks in data be better reconstructed from more advanced alignment procedures, the MC

simulation of these tracks will also converge to reflect more accurately the status of the detector. This will help to reduce the dominant systematic uncertainties associated with the MC based unfolding procedure. Before it was shut down in July 2007 ZEUS collected ~ 0.35 fb^{-1} with the MVD. This data can be used to produce more statistically precise and granular measurements of charm production. This analysis shows the advantage to $F_2^{c\bar{c}}$ extraction of being able to reconstruct D meson candidates at low p_T^D. From a more complete understanding of the detector it may be possible to further extend the available kinematic region both to lower p_T^D and to greater values of η^D. The lifetime based cuts used in these analyses are based on the spatial separation vertices in the transverse plane. With improved understanding of the detector it will be possible to use a fully three-dimensional decay length which will increase the effectiveness of such cuts at lower p_T^D.

Appendix A: Correction factors, efficiency and purity

This appendix contains figures showing the correction factors $\mathcal{C}$, efficiencies $\mathcal{E}$ and purities $\mathcal{P}$ for each analysis bin in both the $D^\pm$ and D^0 meson analyses along with the MC weighting procedure correction as described in section 6.3.1.
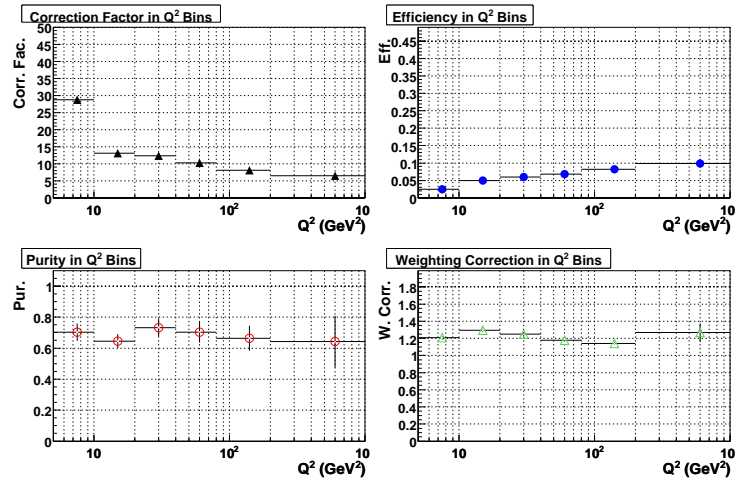
Figure A-1: *The correction factors, efficiencies, purities and weighting corrections for the Q^2 differential cross section in the $D^\pm$ analysis.*
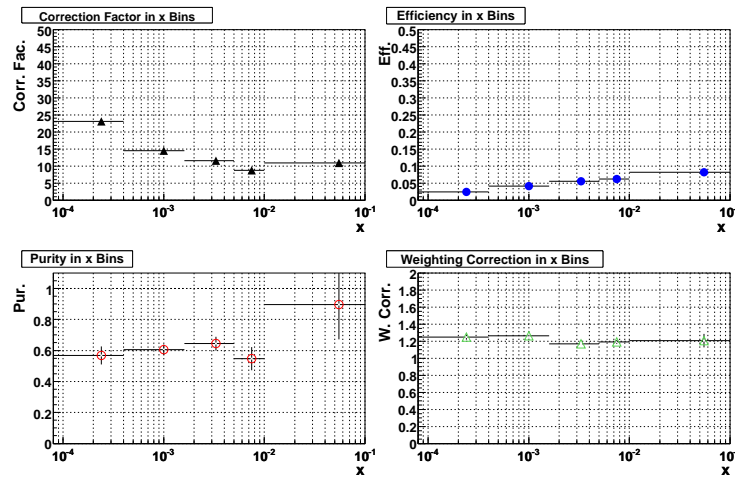
Figure A-2: *The correction factors, efficiencies, purities and weighting corrections for the x differential cross section in the $D^\pm$ analysis.*
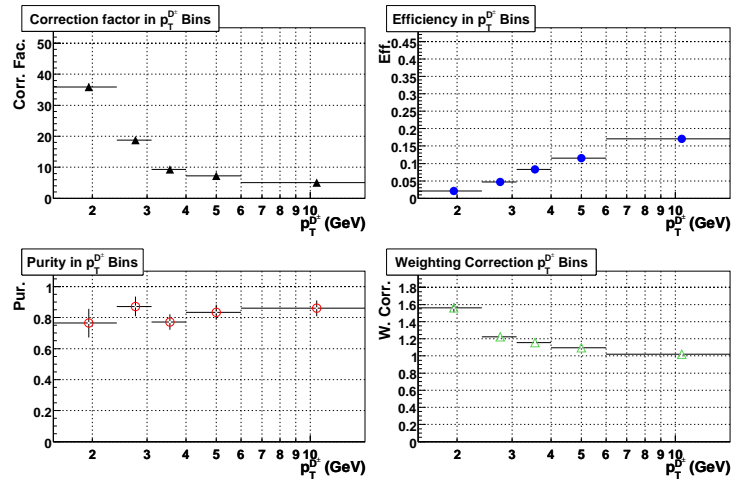
Figure A-3: *The correction factors, efficiencies, purities and weighting corrections for the* $p_T^{D^\pm}$ *differential cross section in the* $D^\pm$ *analysis.*
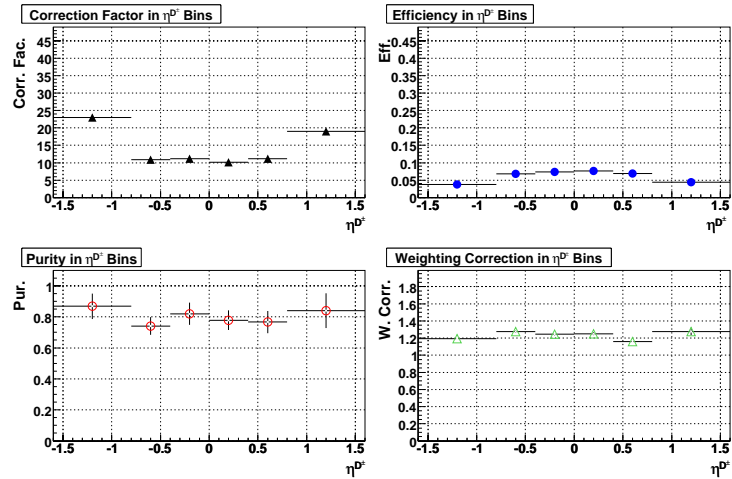
Figure A-4: *The correction factors, efficiencies, purities and weighting corrections for the* $\eta^{D^\pm}$ *differential cross section in the* $D^\pm$ *analysis.*
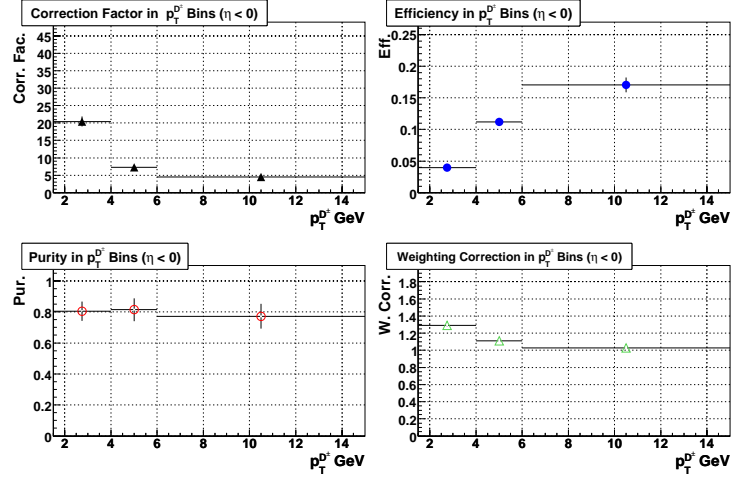
Figure A-5: *The correction factors, efficiencies, purities and weighting corrections for the* $p_T^{D^\pm}$, $\eta^{D^\pm} < 0$ *double differential cross sections in the* $D^\pm$ *analysis.*
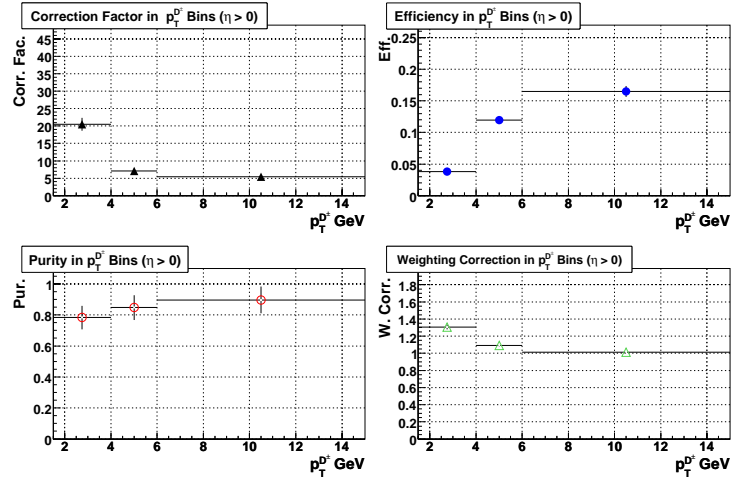
Figure A-6: *The correction factors, efficiencies, purities and weighting corrections for the* $p_T^{D^\pm}$, $\eta^{D^\pm} > 0$ *double differential cross sections in the* $D^\pm$ *analysis.*
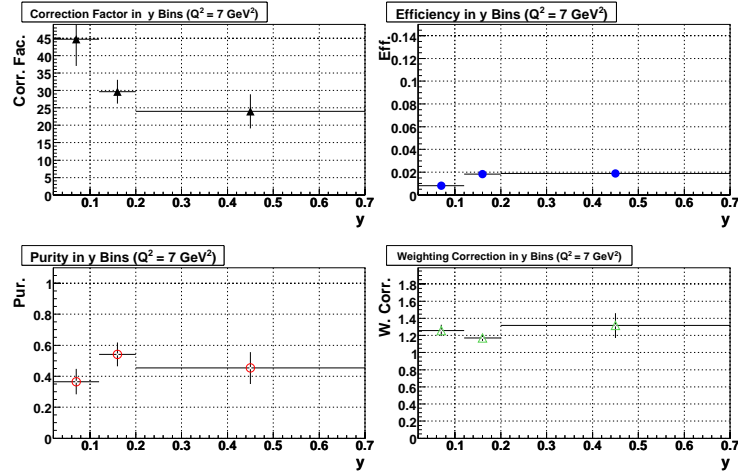
Figure A-7: *The correction factors, efficiencies, purities and weighting corrections for the the y bins in the $5 < Q^2 < 9$ GeV^2 region used for the $F_2^{c\bar{c}}$ extraction from the $D^{\pm}$ analysis.*
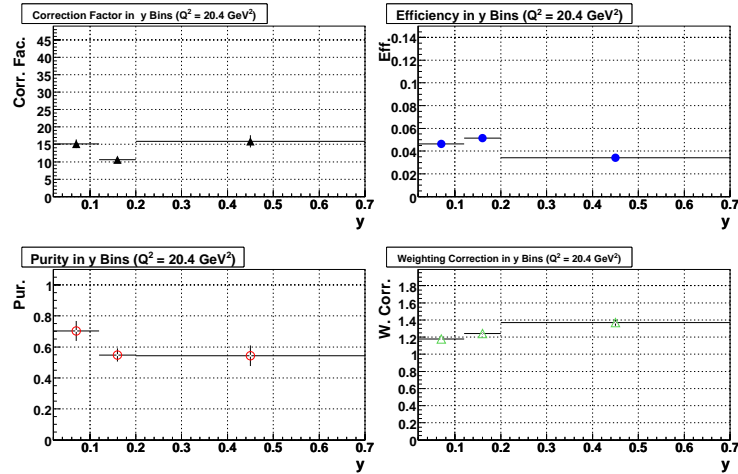
Figure A-8: *The correction factors, efficiencies, purities and weighting corrections for the the y bins in the $9 < Q^2 < 44$ GeV^2 region used for the $F_2^{c\bar{c}}$ extraction from the $D^{\pm}$ analysis.*
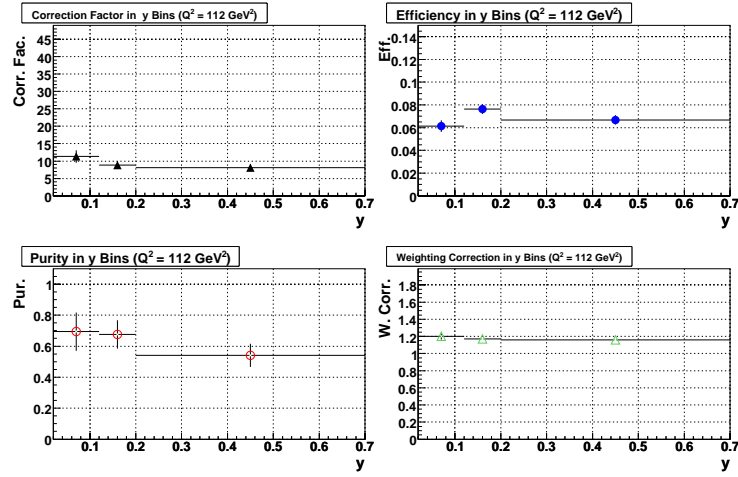
Figure A-9: *The correction factors, efficiencies, purities and weighting corrections for the the y bins in the $44 < Q^2 < 1000$ GeV^2 region used for the $F_2^{c\bar{c}}$ extraction from the $D^{\pm}$ analysis.*
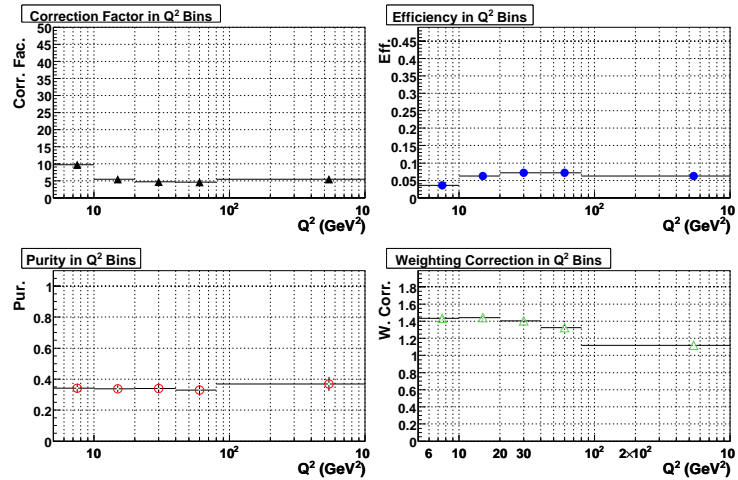
Figure A-10: *The correction factors, efficiencies, purities and weighting corrections for the Q^2 differential cross section in the D^0 analysis.*
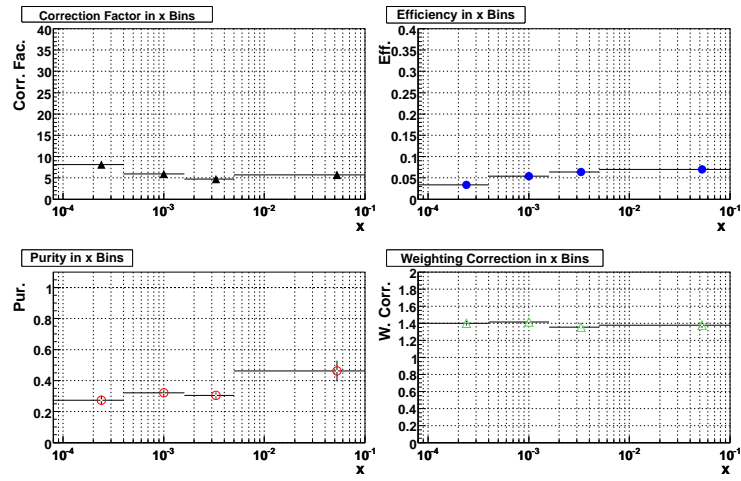
Figure A-11: *The correction factors, efficiencies, purities and weighting corrections for the x differential cross section in the D^0 analysis.*
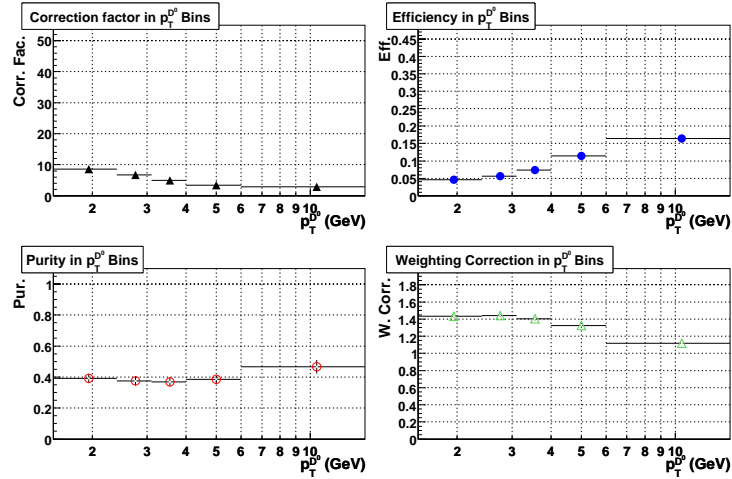
Figure A-12: *The correction factors, efficiencies, purities and weighting corrections for the $p_T^{D^0}$ differential cross section in the D^0 analysis.*

153
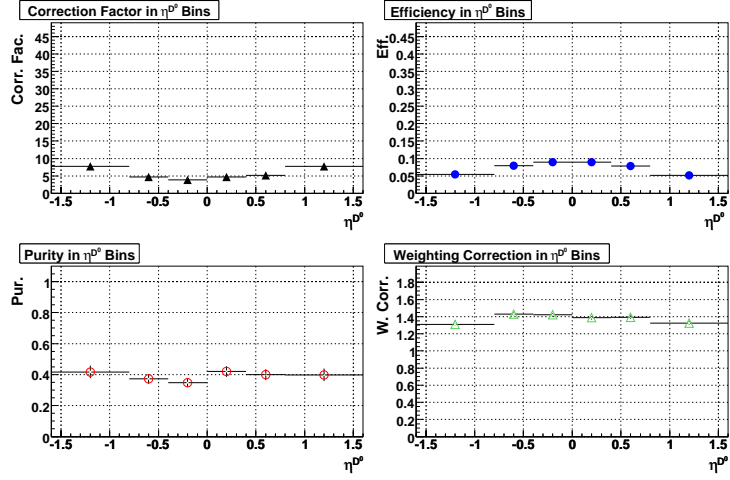
Figure A-13: *The correction factors, efficiencies, purities and weighting corrections for the η^{D^0} differential cross section in the D^0 analysis.*
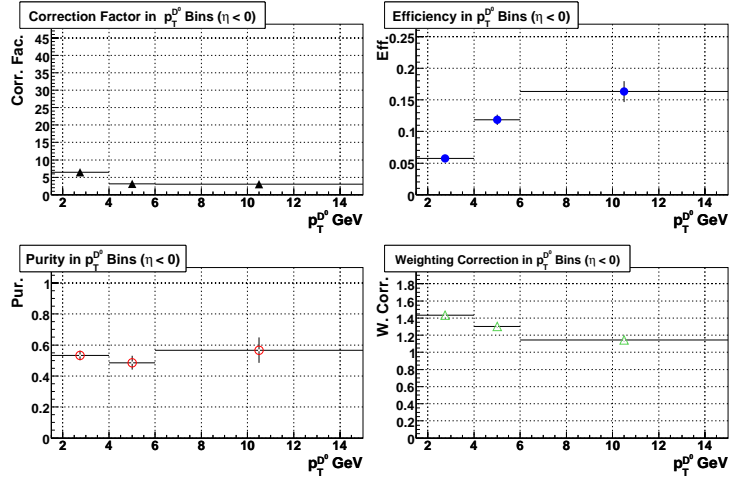
Figure A-14: *The correction factors, efficiencies, purities and weighting corrections for the $p_T^{D^0}$, $\eta^{D^0} < 0$ double differential cross sections in the D^0 analysis.*
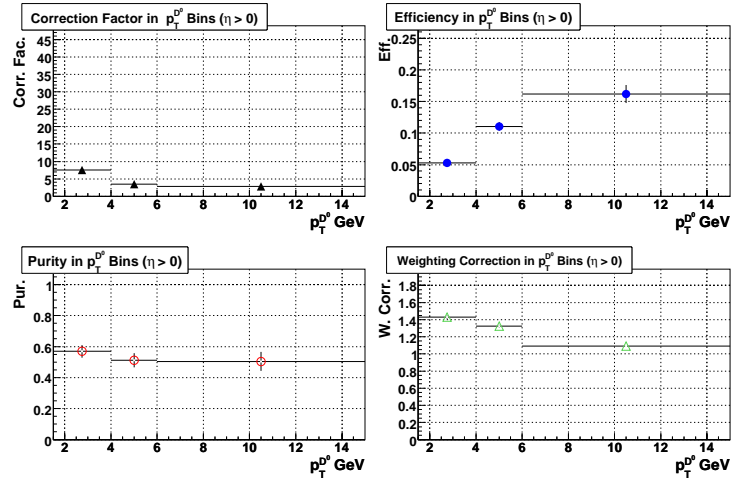
Figure A-15: *The correction factors, efficiencies, purities and weighting corrections for the $p_T^{D^0}$, $\eta^{D^0} > 0$ double differential cross sections in the D^0 analysis.*
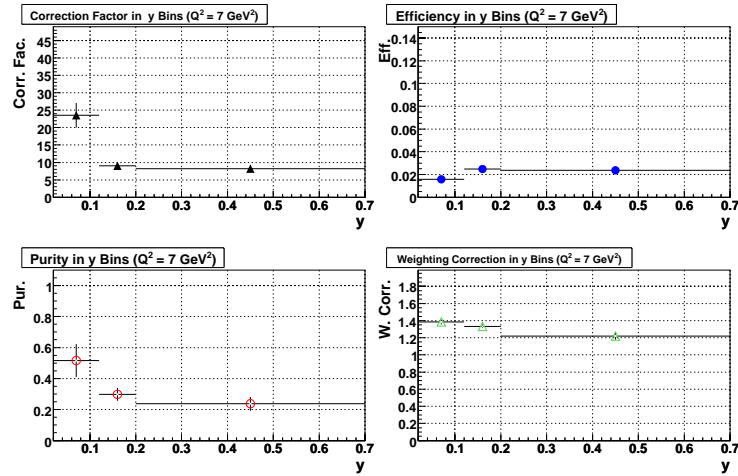
Figure A-16: *The correction factors, efficiencies, purities and weighting corrections for the the y bins in the $5 < Q^2 < 9$ GeV^2 region used for the $F_2^{c\bar{c}}$ extraction from the D^0 analysis.*
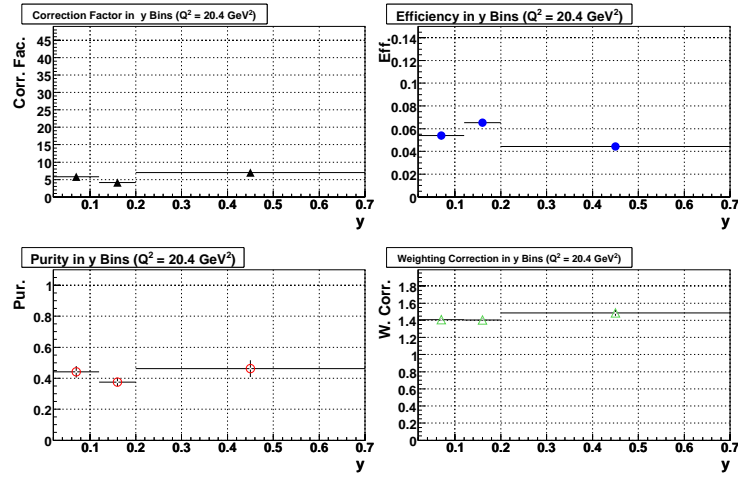
Figure A-17: *The correction factors, efficiencies, purities and weighting corrections for the the y bins in the $9 < Q^2 < 44$ GeV^2 region used for the $F_2^{c\bar{c}}$ extraction from the D^0 analysis.*
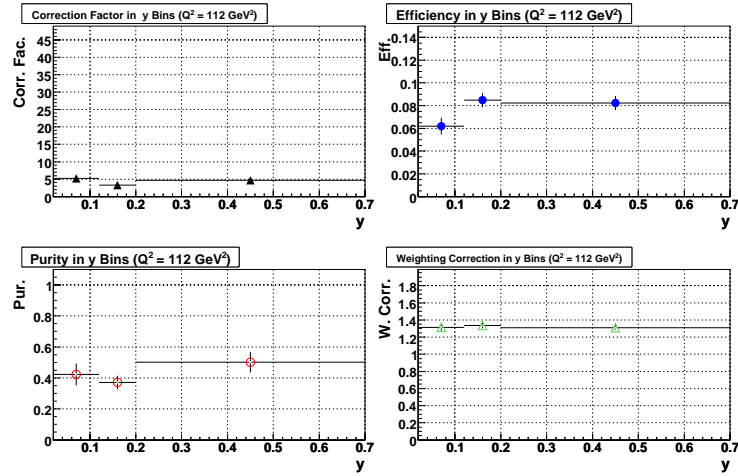
Figure A-18: *The correction factors, efficiencies, purities and weighting corrections for the the y bins in the $44 < Q^2 < 1000$ GeV^2 region used for the $F_2^{c\bar{c}}$ extraction from the D^0 analysis.*

Appendix B: Data and Monte Carlo $M(K\pi\pi)$ and $M(K\pi)$ distributions

This appendix contains figures showing the invariant mass distributions for data and MC in all single and double differential cross sections for both $D^\pm$ and D^0 analyses. The $M(K\pi\pi)$ and $M(K\pi)$ distributions in bins of $c\tau$ used to extract the D meson lifetimes are also shown. Both untagged and tagged distributions are shown for the D^0 analysis.
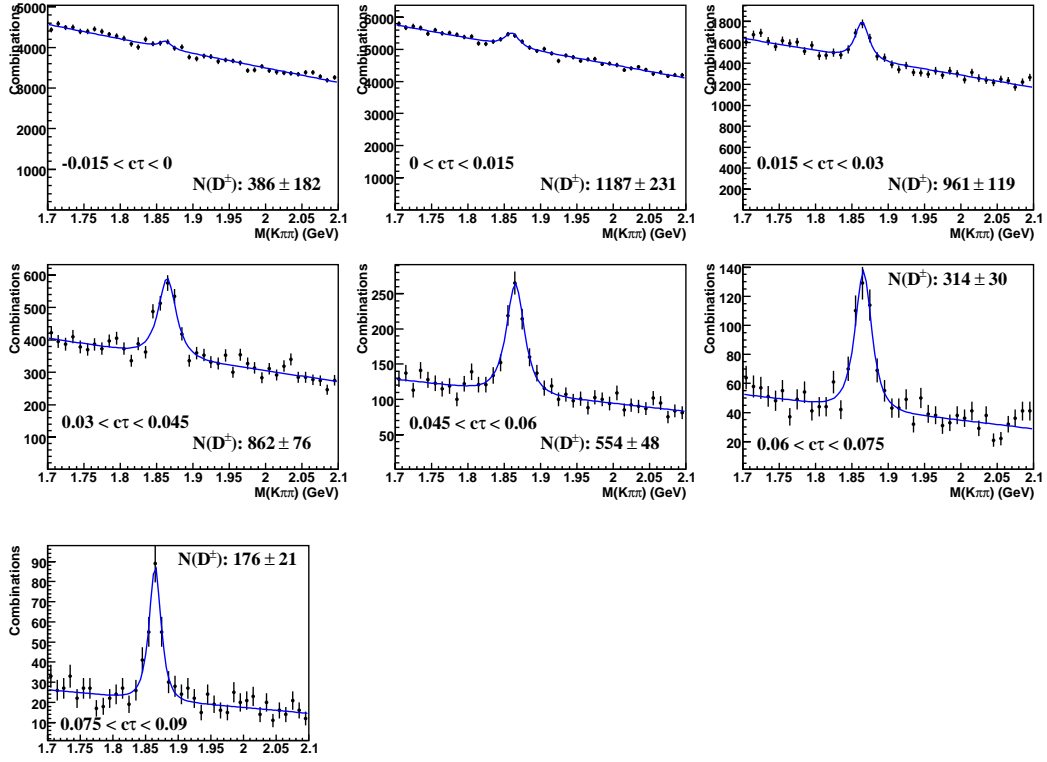
Figure B-1: $M(K\pi\pi)$ *distributions for* $D^{\pm}$ *mesons in data (points) differential in bins of* $c\tau$. *The fitted sum of a modified Gaussian and background function is also shown (line).*
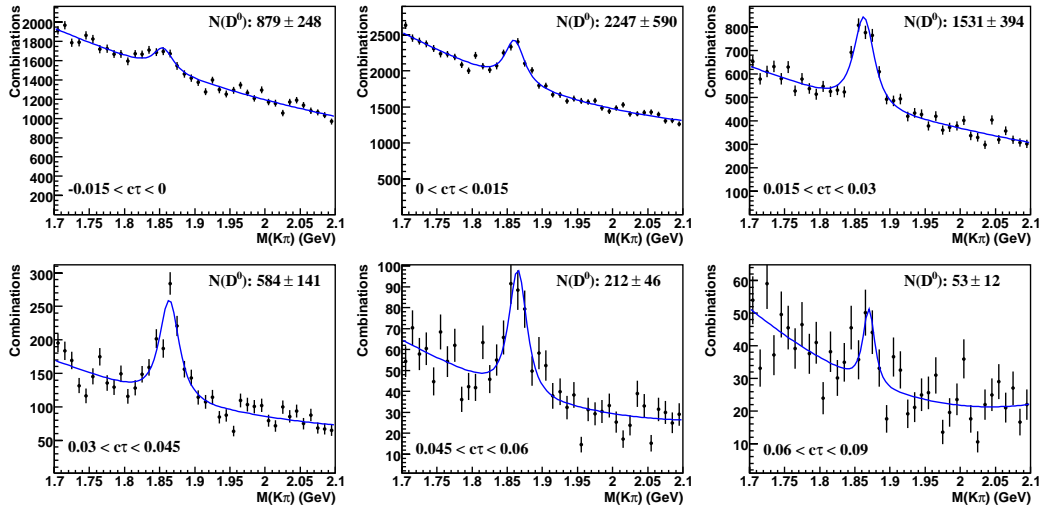
Figure B-2: $M(K\pi\pi)$ *distributions for untagged* D^0 *mesons in data (points) differential in bins of* $c\tau$. *The fitted sum of a modified Gaussian and background function is also shown (line).*
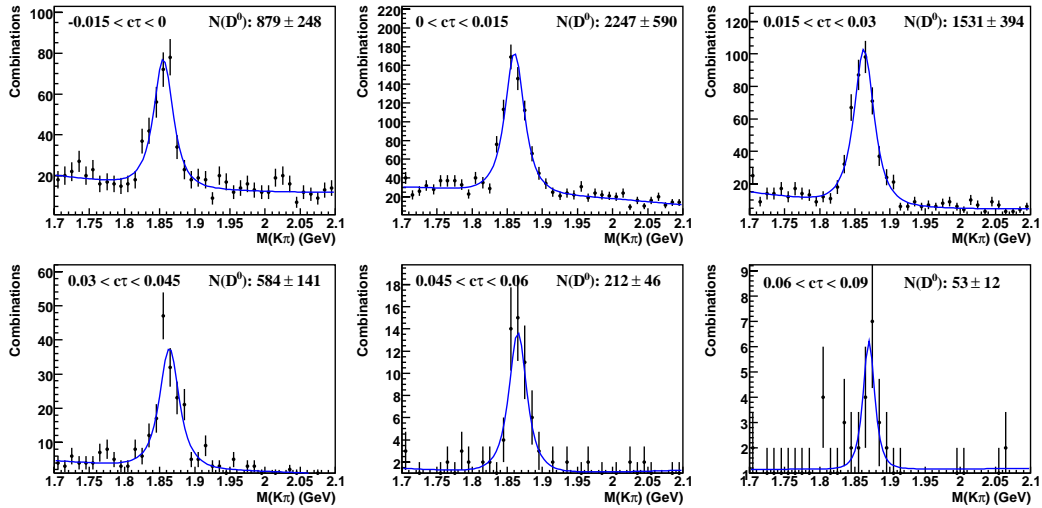
Figure B-3: $M(K\pi\pi)$ *distributions for tagged* D^0 *mesons in data (points) differential in bins of* $c\tau$. *The fitted sum of a modified Gaussian and background function is also shown (line).*
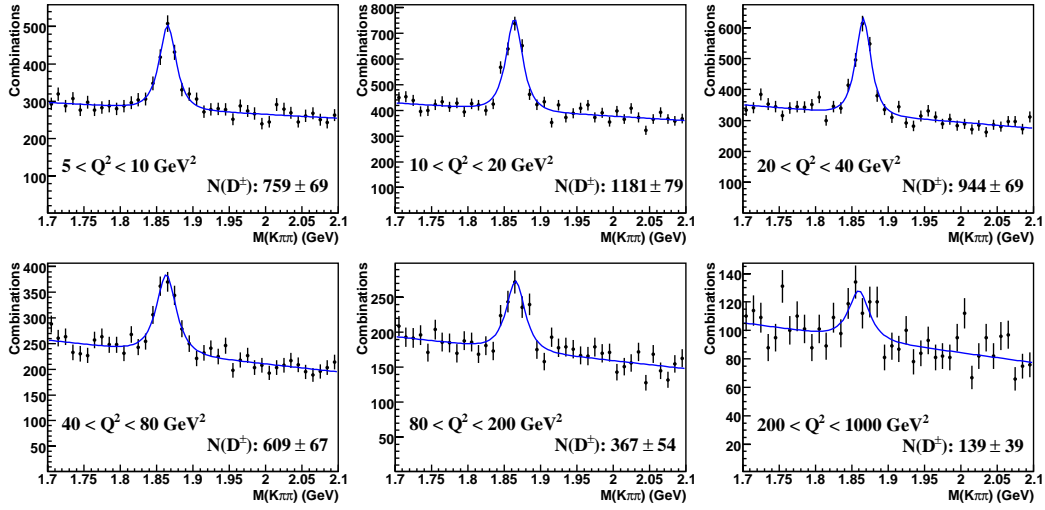
Figure B-4: $M(K\pi\pi)$ *distributions for* $D^{\pm}$ *mesons in data (points) differential in bins of* Q^2. *The fitted sum of a modified Gaussian and background function is also shown (line).*
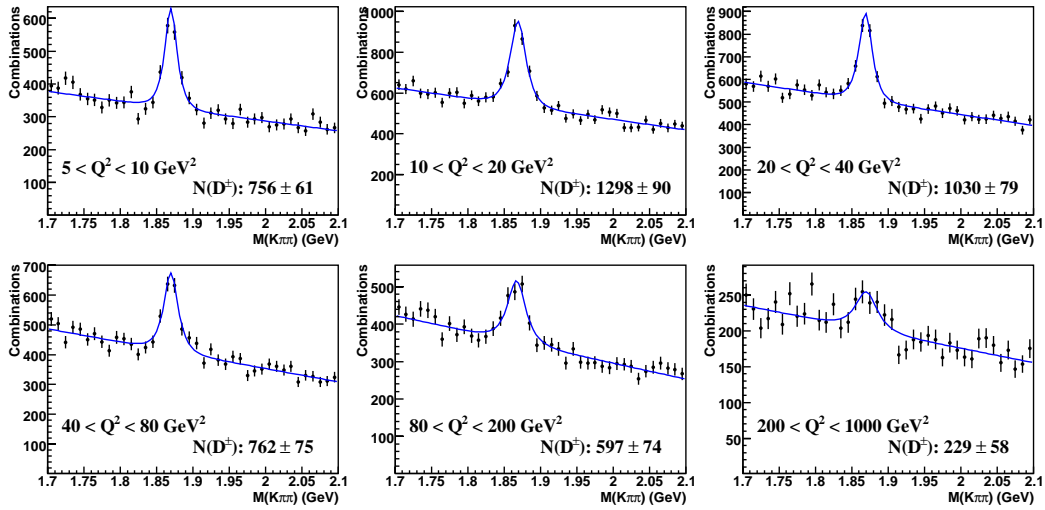
Figure B-5: $M(K\pi\pi)$ *distributions for* $D^{\pm}$ *mesons in MC (points) differential in bins of* Q^2. *The fitted sum of a modified Gaussian and background function is also shown (line).*
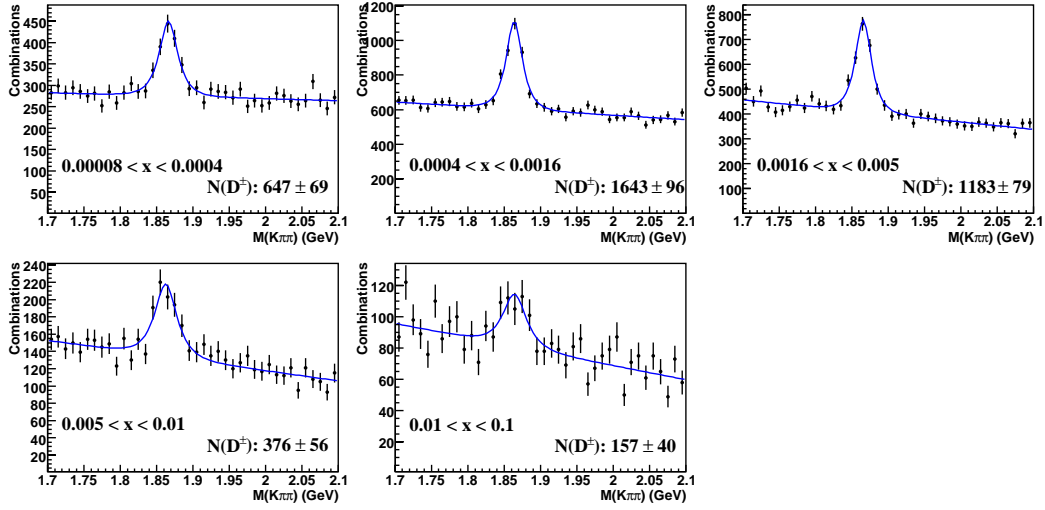
Figure B-6: $M(K\pi\pi)$ distributions for $D^\pm$ mesons in data (points) differential in bins of x. The fitted sum of a modified Gaussian and background function is also shown (line).
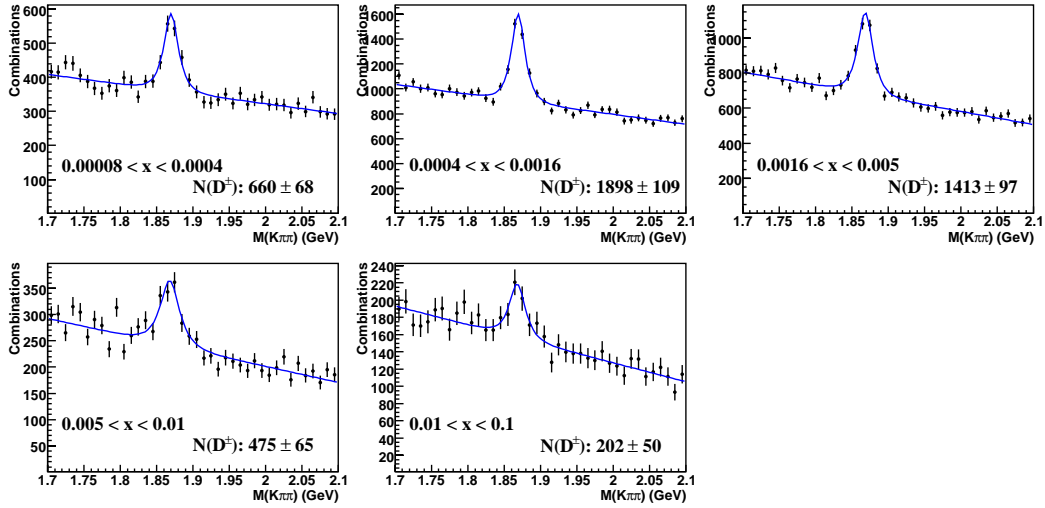
Figure B-7: $M(K\pi\pi)$ distributions for $D^\pm$ mesons in MC (points) differential in bins of x. The fitted sum of a modified Gaussian and background function is also shown (line).
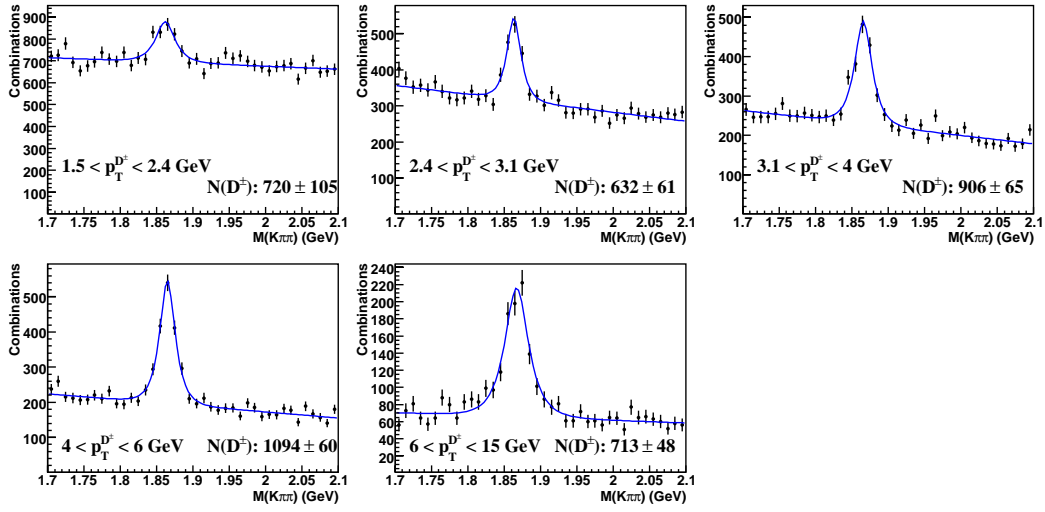
Figure B-8: $M(K\pi\pi)$ distributions for $D^{\pm}$ mesons in data (points) differential in bins of $p_T^{D\pm}$. The fitted sum of a modified Gaussian and background function is also shown (line).
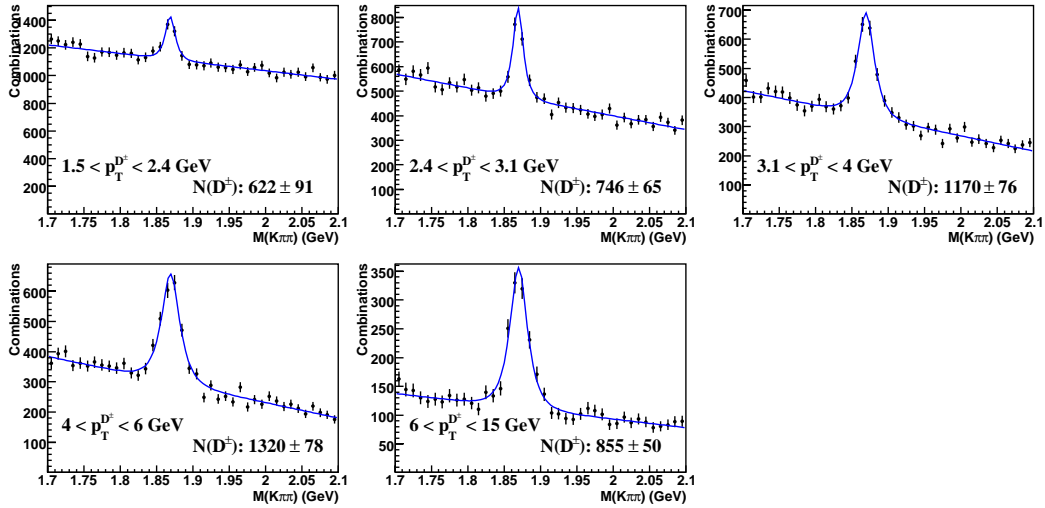
Figure B-9: $M(K\pi\pi)$ distributions for $D^{\pm}$ mesons in MC (points) differential in bins of $p_T^{D\pm}$. The fitted sum of a modified Gaussian and background function is also shown (line).
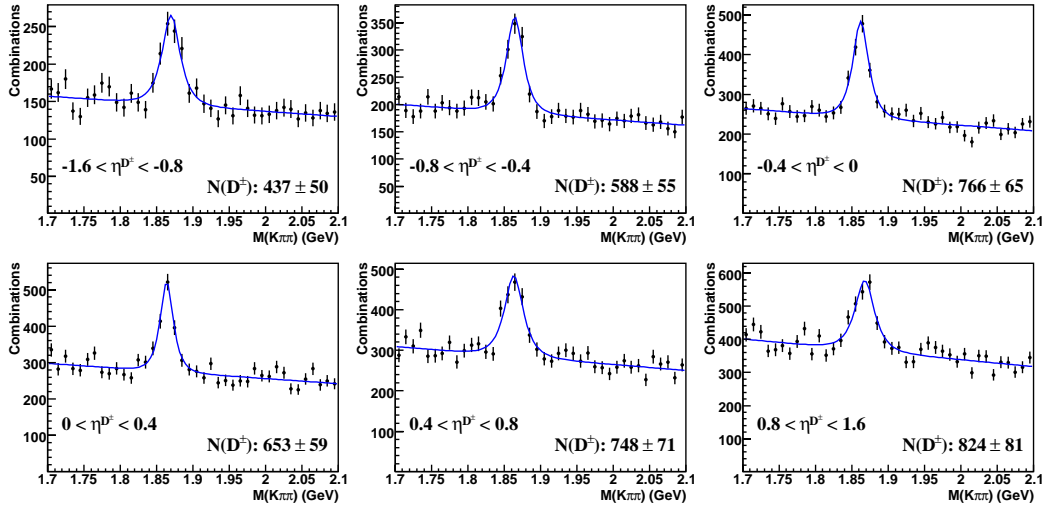
Figure B-10: $M(K\pi\pi)$ distributions for $D^{\pm}$ mesons in data (points) differential in bins of $\eta^{D^{\pm}}$. The fitted sum of a modified Gaussian and background function is also shown (line).
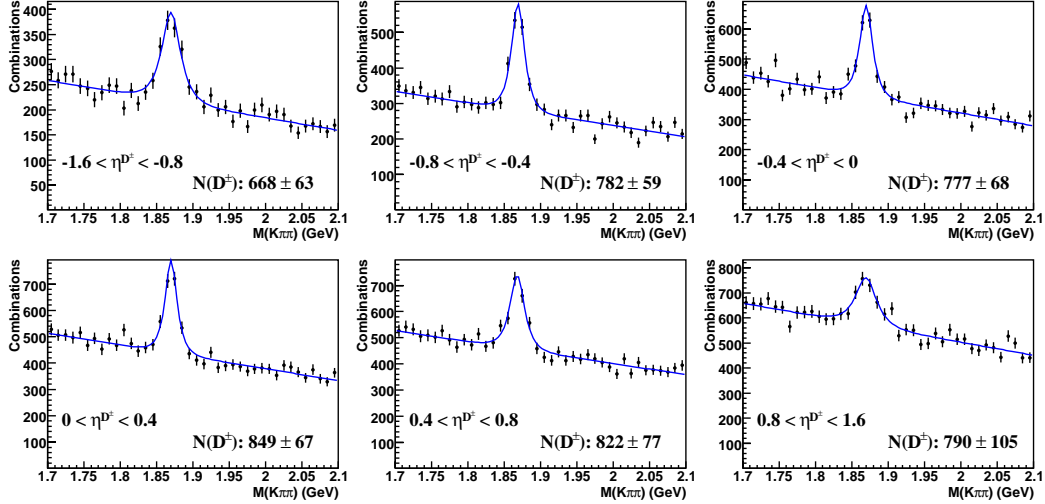
Figure B-11: $M(K\pi\pi)$ distributions for $D^{\pm}$ mesons in MC (points) differential in bins of $\eta^{D^{\pm}}$. The fitted sum of a modified Gaussian and background function is also shown (line).
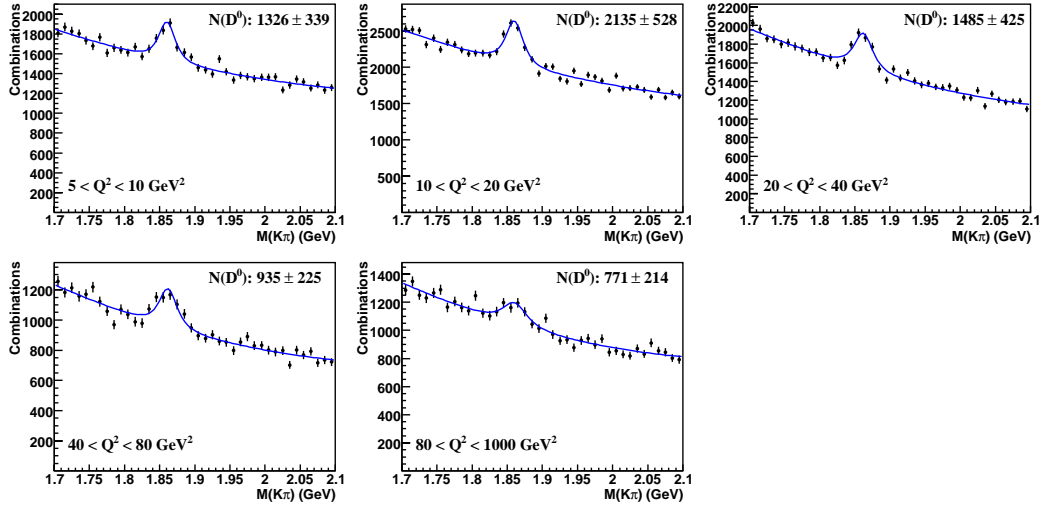
Figure B-12: $M(K\pi)$ distributions for untagged D^0 mesons in data (points) differential in bins of Q^2. The fitted sum of a modified Gaussian and background function is also shown (line).
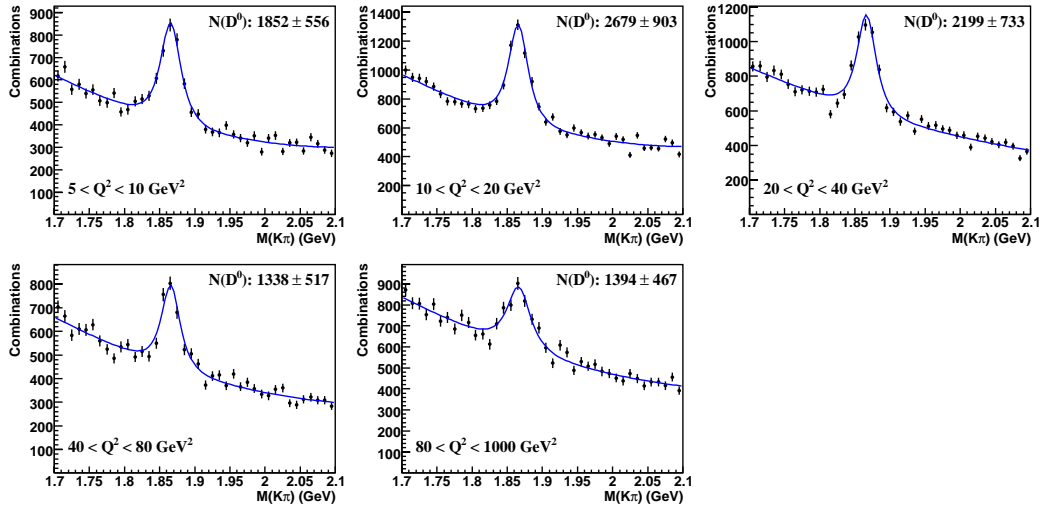
Figure B-13: $M(K\pi)$ distributions for untagged D^0 mesons in MC (points) differential in bins of Q^2. The fitted sum of a modified Gaussian and background function is also shown (line).
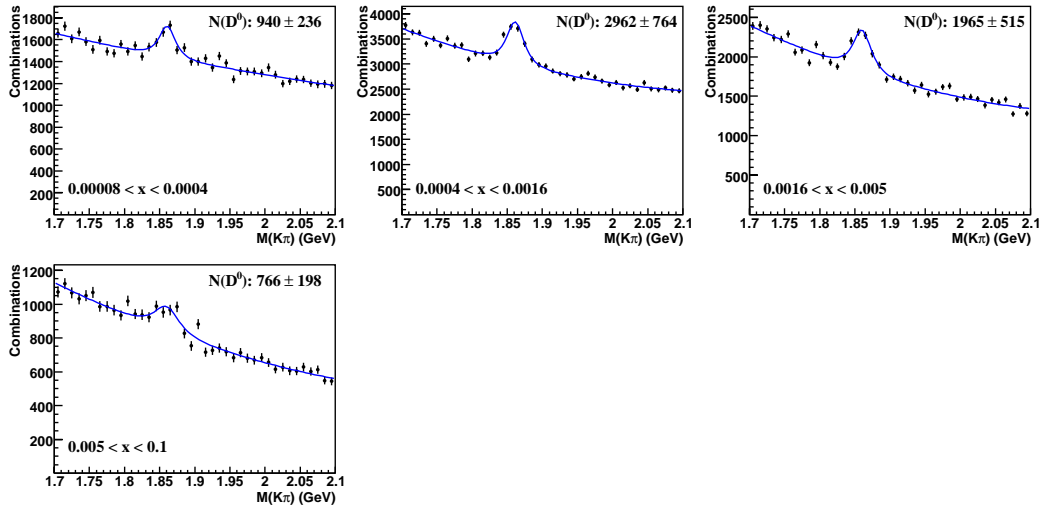
Figure B-14: $M(K\pi)$ *distributions for untagged* D^0 *mesons in data (points) differential in bins of* x. *The fitted sum of a modified Gaussian and background function is also shown (line).*
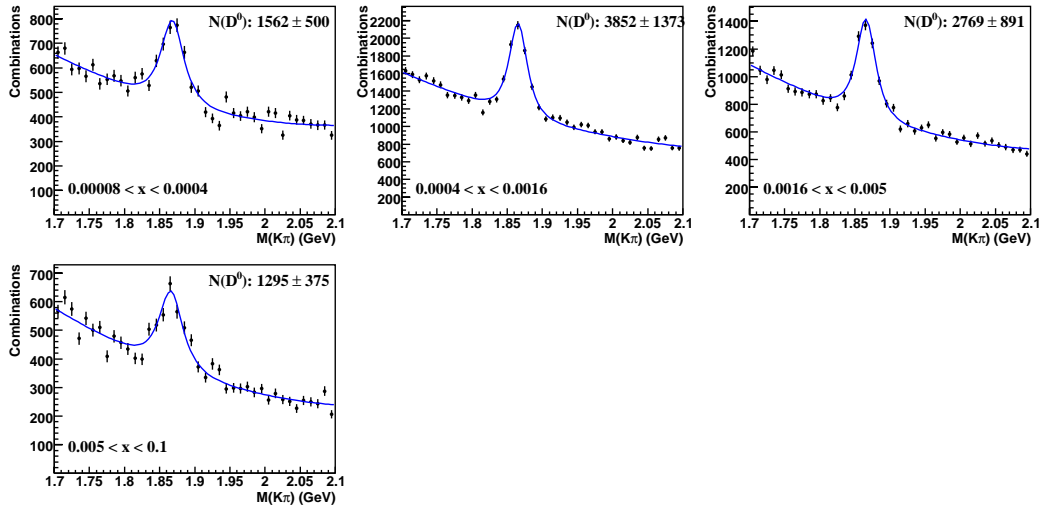
Figure B-15: $M(K\pi)$ *distributions for untagged* D^0 *mesons in MC (points) differential in bins of* x. *The fitted sum of a modified Gaussian and background function is also shown (line).*
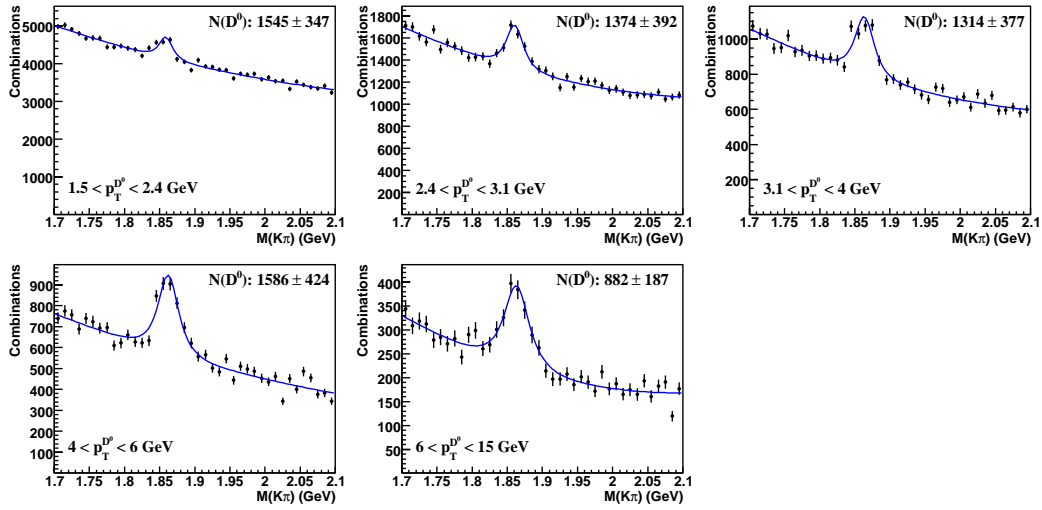
Figure B-16: $M(K\pi)$ distributions for untagged D^0 mesons in data (points) differential in bins of $p_T^{D^0}$. The fitted sum of a modified Gaussian and background function is also shown (line).
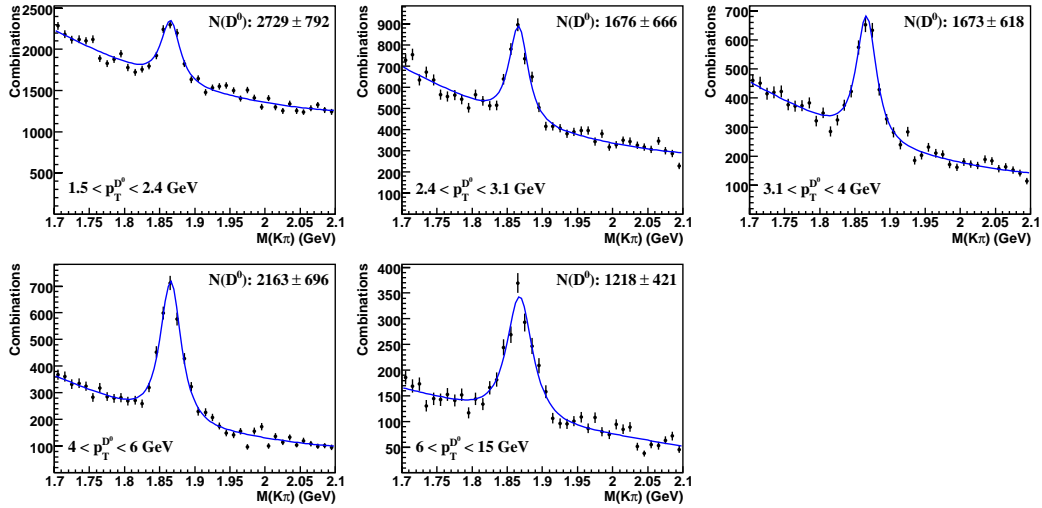
Figure B-17: $M(K\pi)$ distributions for untagged D^0 mesons in MC (points) differential in bins of $p_T^{D^0}$. The fitted sum of a modified Gaussian and background function is also shown (line).
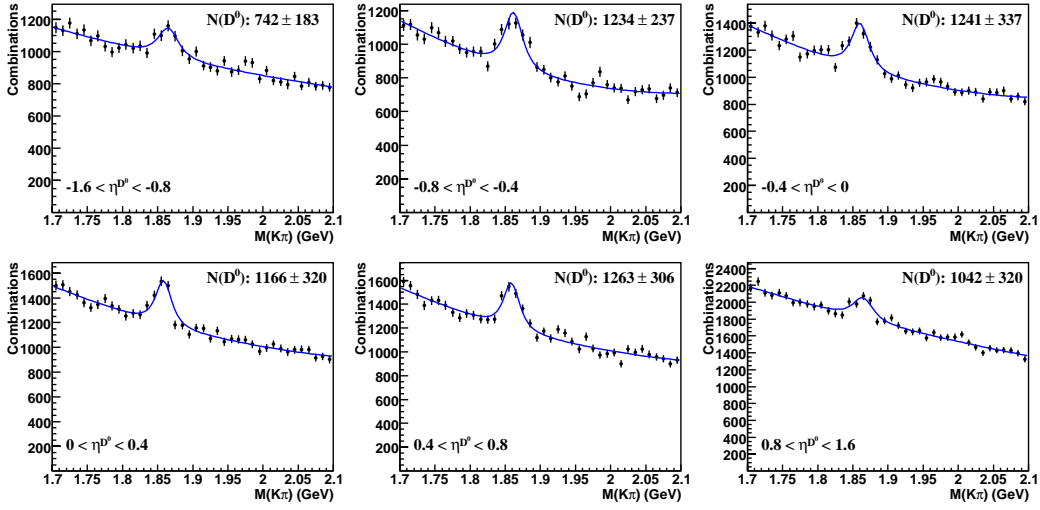
Figure B-18: $M(K\pi)$ distributions for untagged D^0 mesons in data (points) differential in bins of η^{D^0}. The fitted sum of a modified Gaussian and background function is also shown (line).
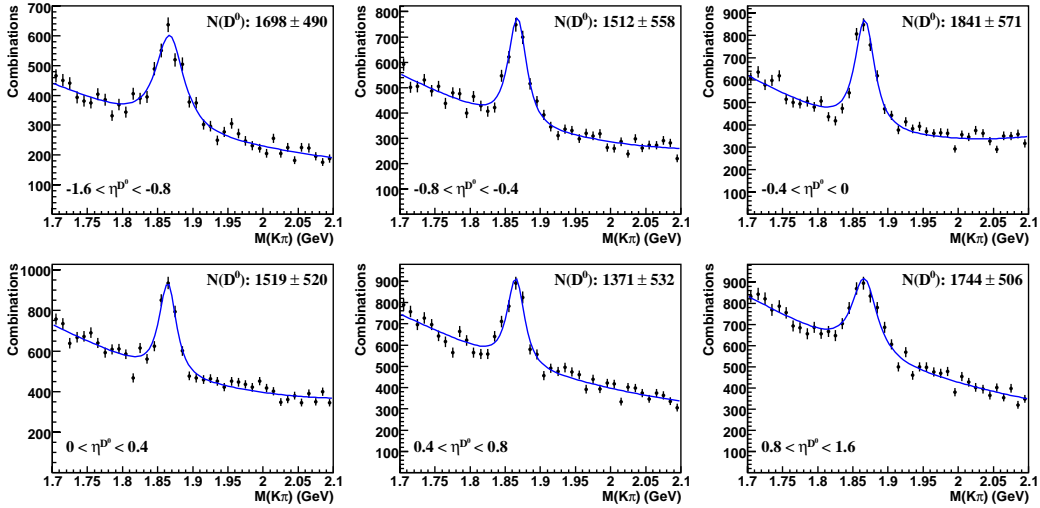
Figure B-19: $M(K\pi)$ distributions for untagged D^0 mesons in MC (points) differential in bins of η^{D^0}. The fitted sum of a modified Gaussian and background function is also shown (line).
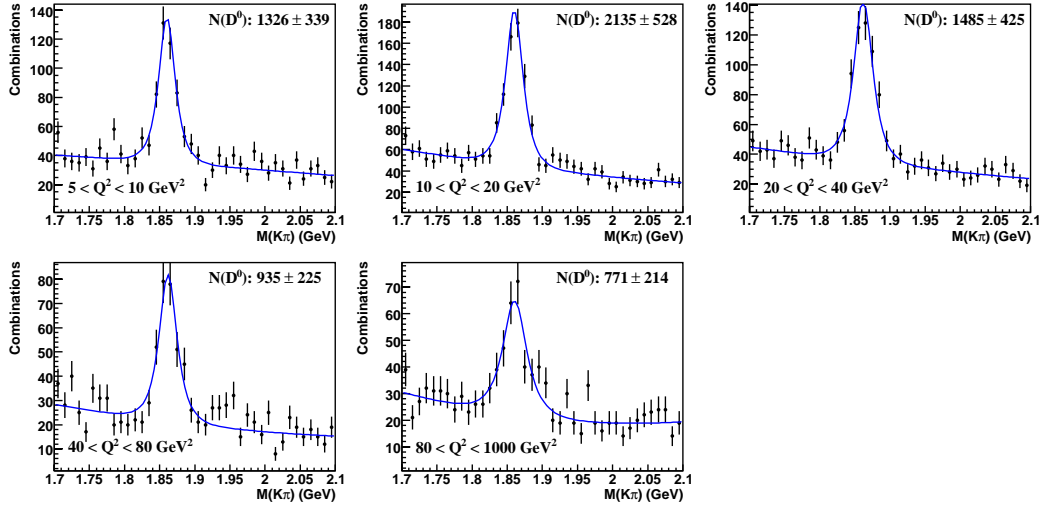
Figure B-20: $M(K\pi)$ distributions for tagged D^0 mesons in data (points) differential in bins of Q^2. The fitted sum of a modified Gaussian and background function is also shown (line).
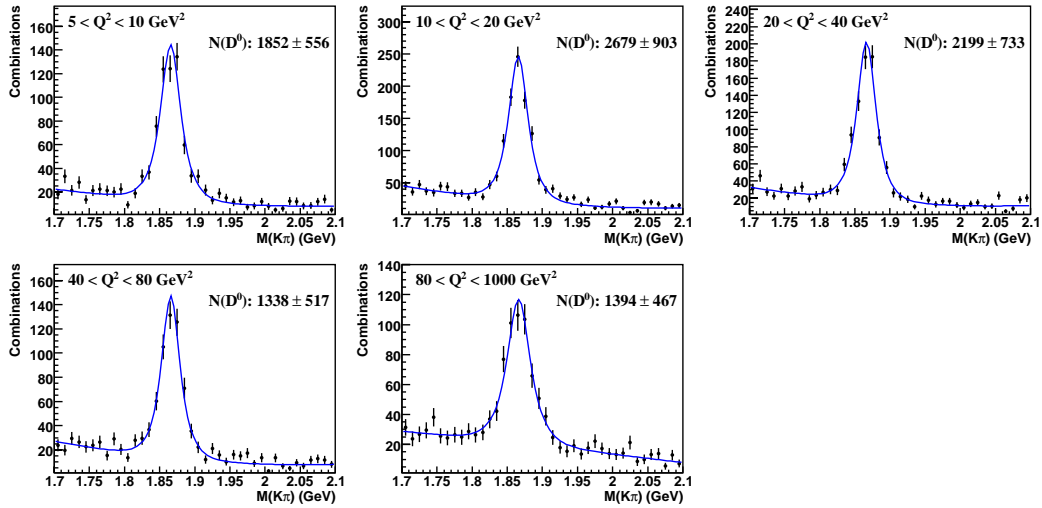
Figure B-21: $M(K\pi)$ distributions for tagged D^0 mesons in MC (points) differential in bins of Q^2. The fitted sum of a modified Gaussian and background function is also shown (line).
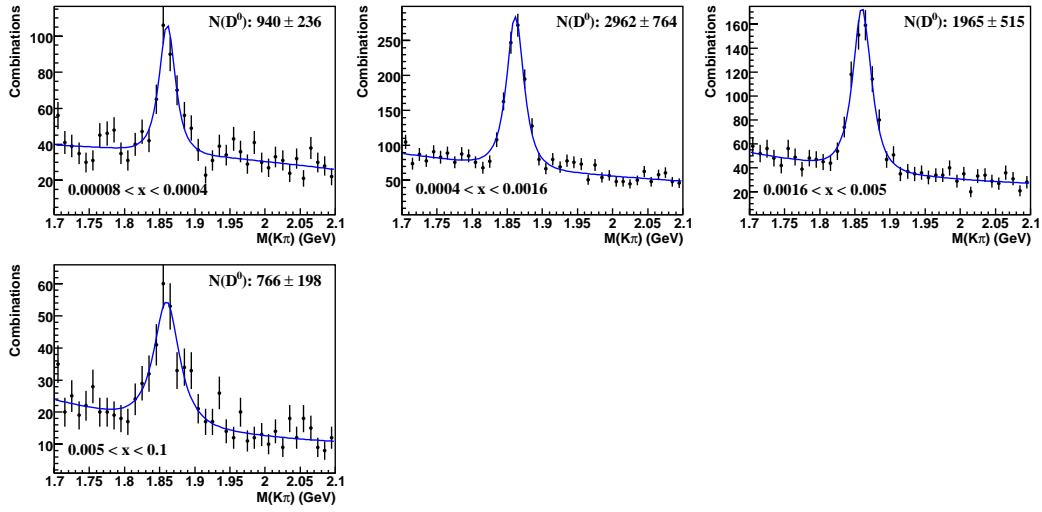
Figure B-22: $M(K\pi)$ distributions for tagged D^0 mesons in data (points) differential in bins of x. The fitted sum of a modified Gaussian and background function is also shown (line).
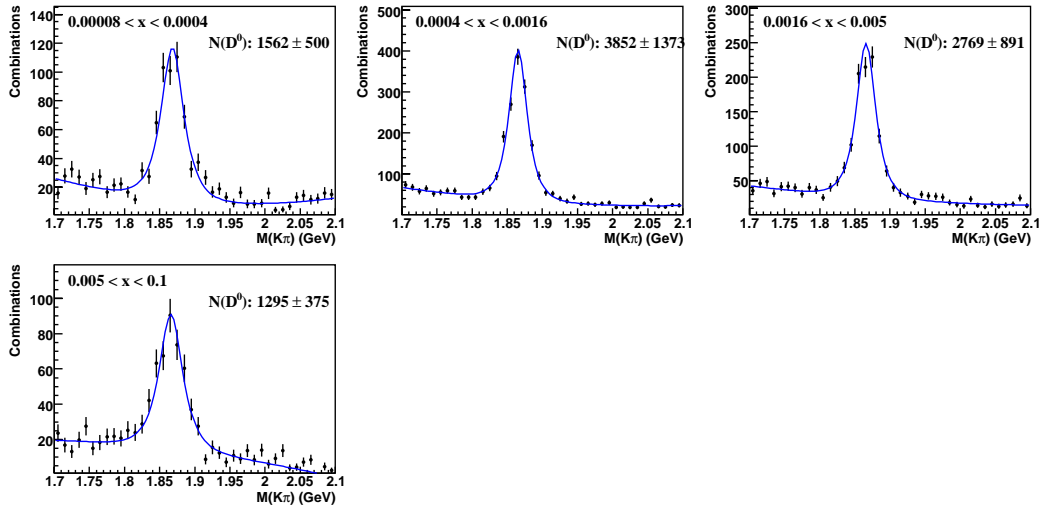
Figure B-23: $M(K\pi)$ distributions for tagged D^0 mesons in MC (points) differential in bins of x. The fitted sum of a modified Gaussian and background function is also shown (line).
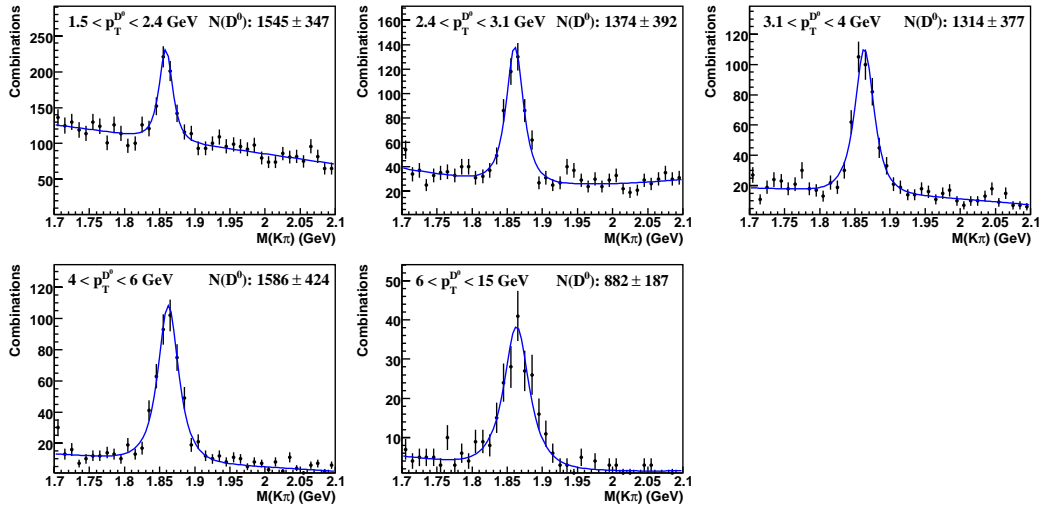
Figure B-24: $M(K\pi)$ distributions for tagged D^0 mesons in data (points) differential in bins of $p_T^{D^0}$. The fitted sum of a modified Gaussian and background function is also shown (line).
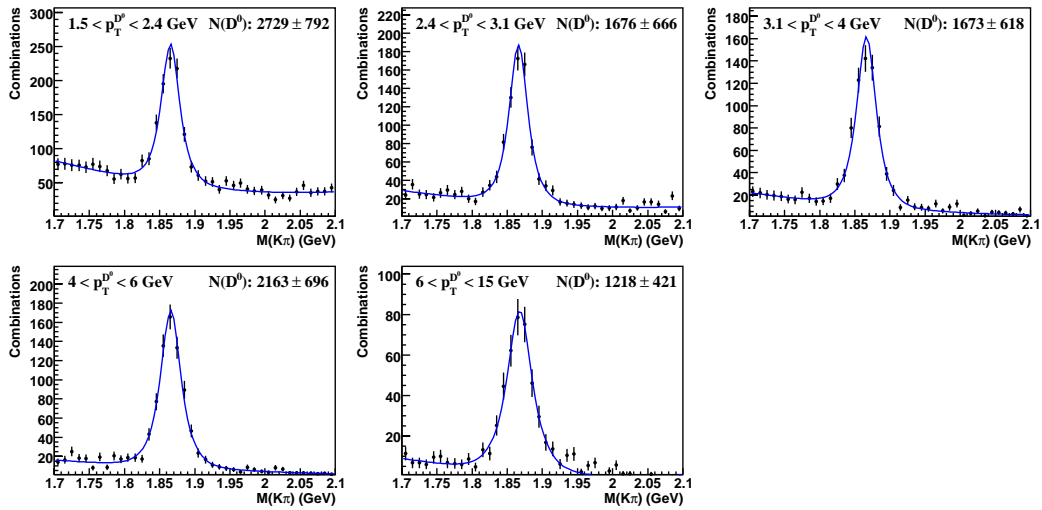
Figure B-25: $M(K\pi)$ distributions for tagged D^0 mesons in MC (points) differential in bins of $p_T^{D^0}$. The fitted sum of a modified Gaussian and background function is also shown (line).
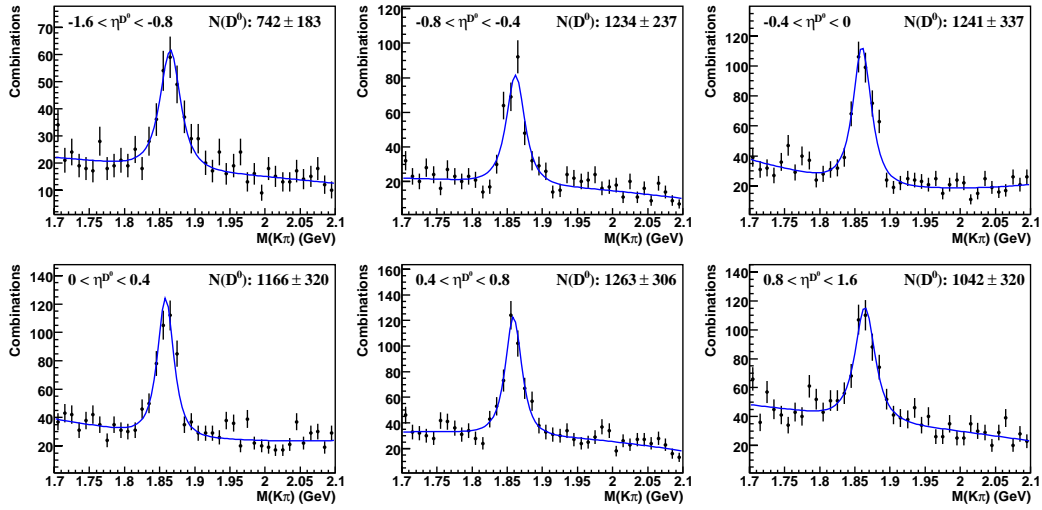
Figure B-26: $M(K\pi)$ *distributions for tagged* D^0 *mesons in data (points) differential in bins of* η^{D^0}. *The fitted sum of a modified Gaussian and background function is also shown (line).*
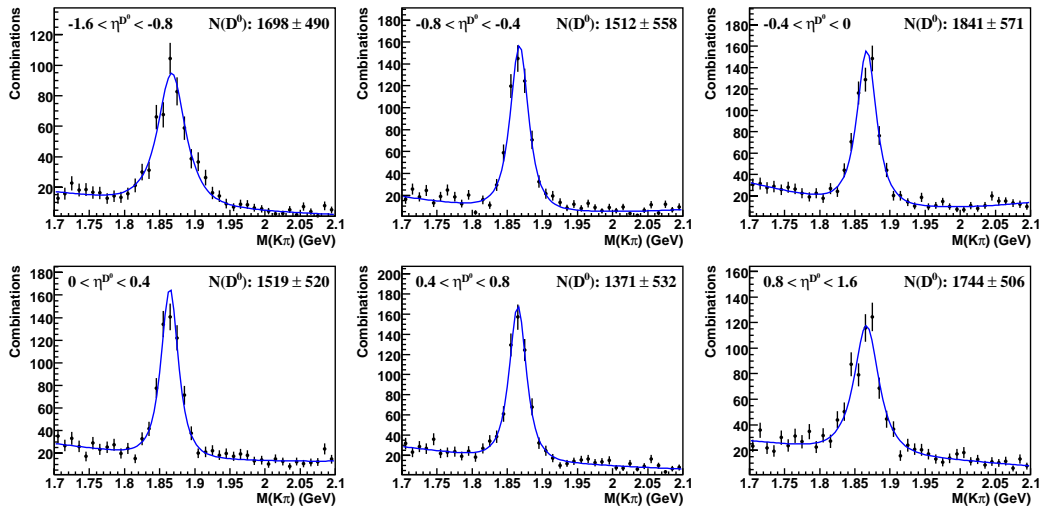
Figure B-27: $M(K\pi)$ *distributions for tagged* D^0 *mesons in MC (points) differential in bins of* η^{D^0}. *The fitted sum of a modified Gaussian and background function is also shown (line).*
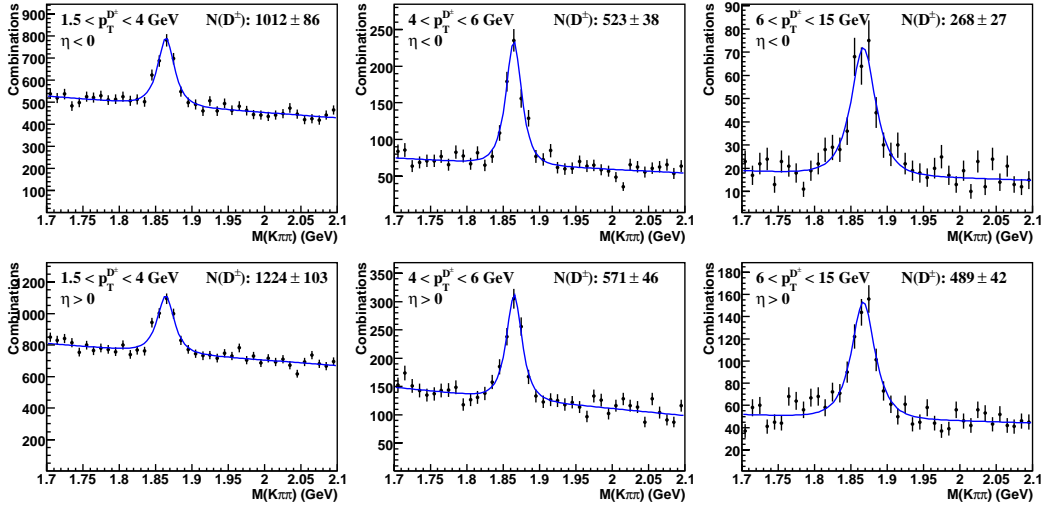
Figure B-28: $M(K\pi\pi)$ *distributions for* $D^{\pm}$ *mesons in data (points) double differential in bins of* $p_T^{D^{\pm}}$ *and* $\eta^{D^{\pm}}$*. The fitted sum of a modified Gaussian and background function is also shown (line).*
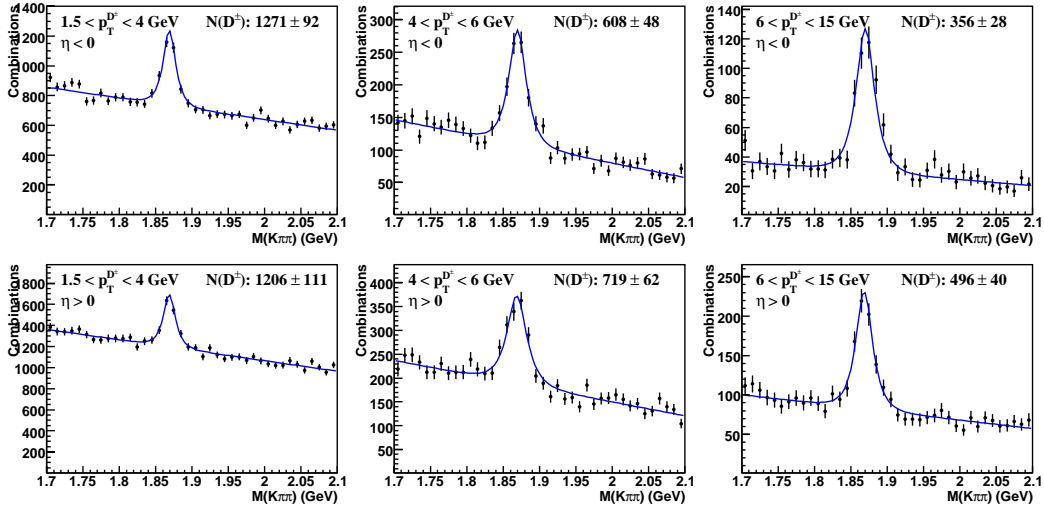
Figure B-29: $M(K\pi\pi)$ *distributions for* $D^{\pm}$ *mesons in MC (points) double differential in bins of* $p_T^{D^{\pm}}$ *and* $\eta^{D^{\pm}}$*. The fitted sum of a modified Gaussian and background function is also shown (line).*
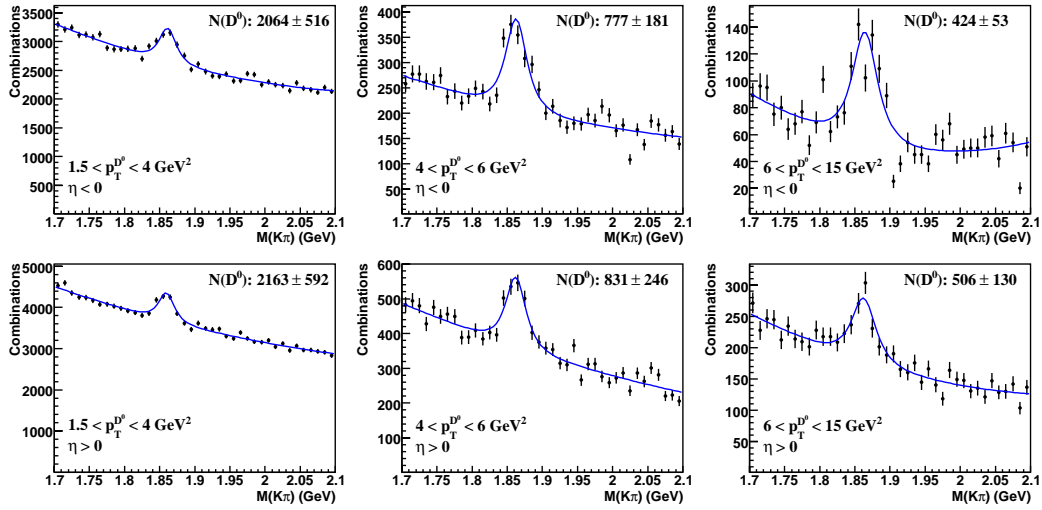
Figure B-30: $M(K\pi)$ *distributions for untagged* D^0 *mesons in data (points) double differential in bins of* $p_T^{D^0}$ *and* η^{D^0}*. The fitted sum of a modified Gaussian and background function is also shown (line).*
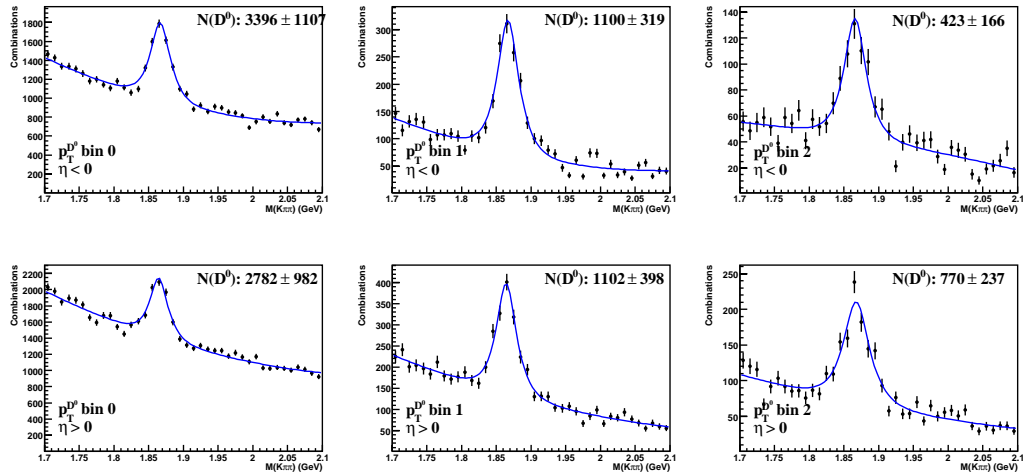
Figure B-31: $M(K\pi)$ *distributions for untagged* D^0 *mesons in MC (points) double differential in bins of* $p_T^{D^0}$ *and* η^{D^0}*. The fitted sum of a modified Gaussian and background function is also shown (line).*
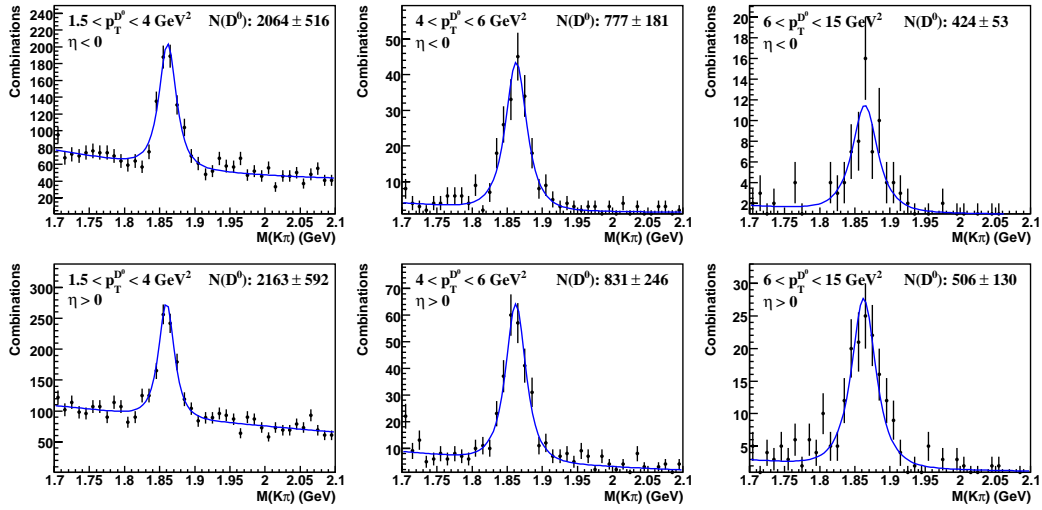
Figure B-32: $M(K\pi)$ distributions for tagged D^0 mesons in data (points) double differential in bins of $p_T^{D^0}$ and η^{D^0}. The fitted sum of a modified Gaussian and background function is also shown (line).
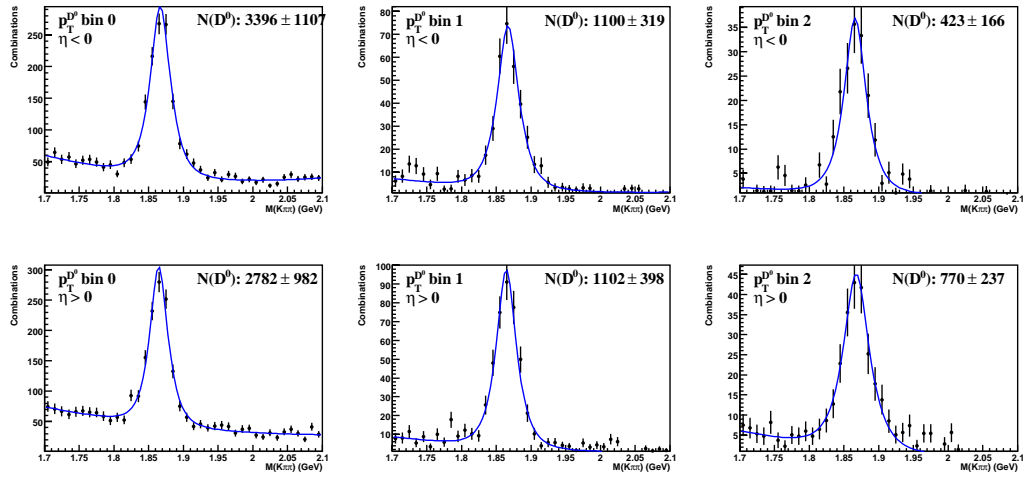
Figure B-33: $M(K\pi)$ distributions for tagged D^0 mesons in MC (points) double differential in bins of $p_T^{D^0}$ and η^{D^0}. The fitted sum of a modified Gaussian and background function is also shown (line).
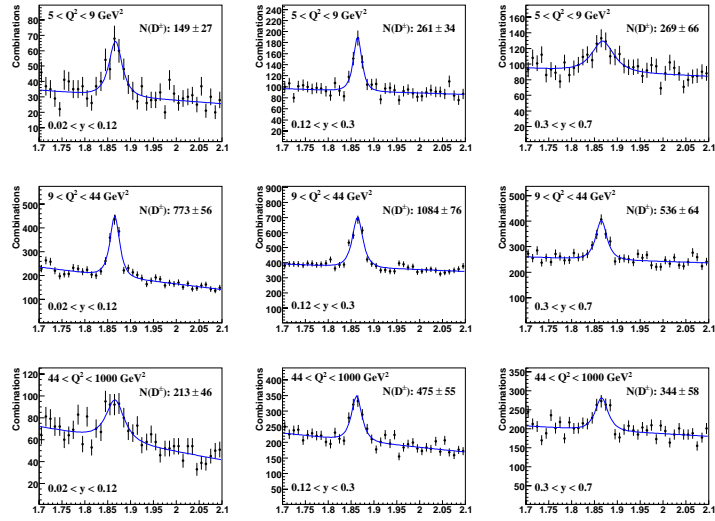
Figure B-34: $M(K\pi\pi)$ distributions for $D^{\pm}$ mesons in data (points) double differential in bins of Q^2 and y. The fitted sum of a modified Gaussian and background function is also shown (line).
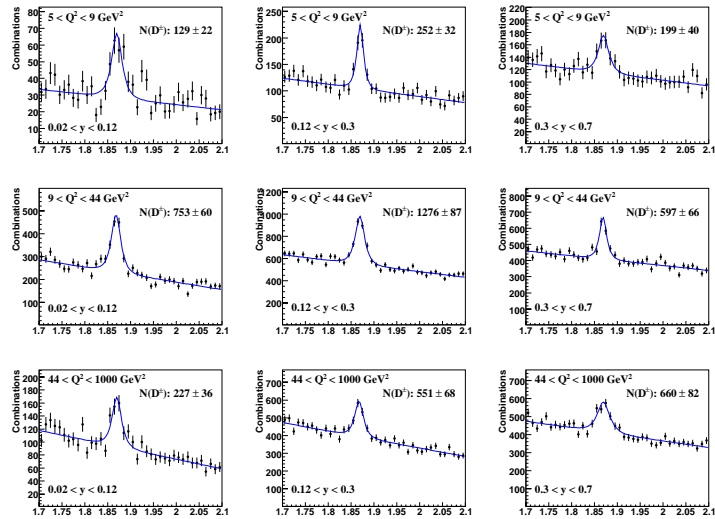
Figure B-35: $M(K\pi\pi)$ distributions for $D^{\pm}$ mesons in MC (points) double differential in bins of Q^2 and y. The fitted sum of a modified Gaussian and background function is also shown (line).
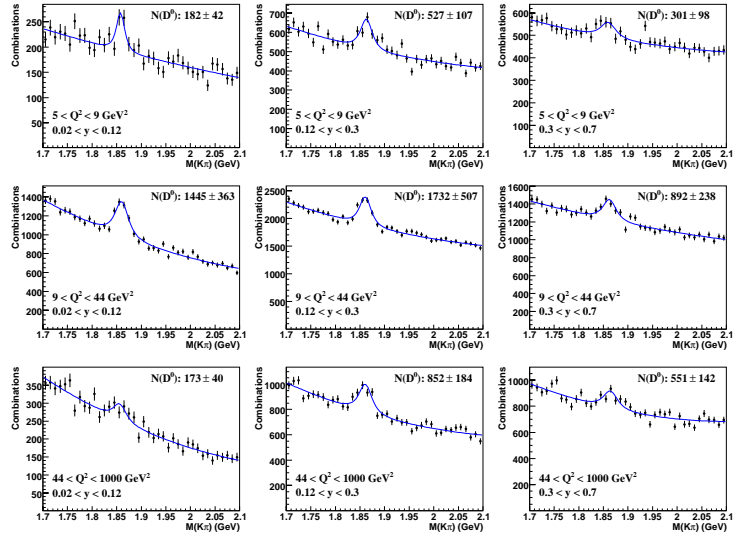
Figure B-36: $M(K\pi)$ distributions for untagged D^0 mesons in data (points) double differential in bins of Q^2 and y. The fitted sum of a modified Gaussian and background function is also shown (line).
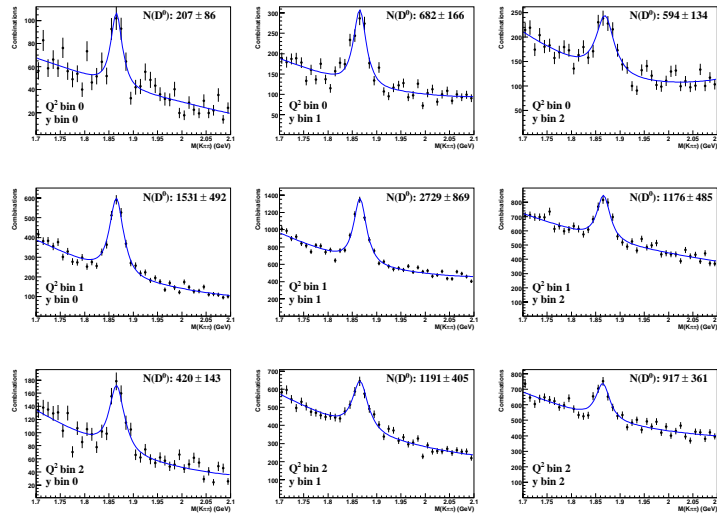
Figure B-37: $M(K\pi)$ distributions for untagged D^0 mesons in MC (points) double differential in bins of Q^2 and y. The fitted sum of a modified Gaussian and background function is also shown (line).
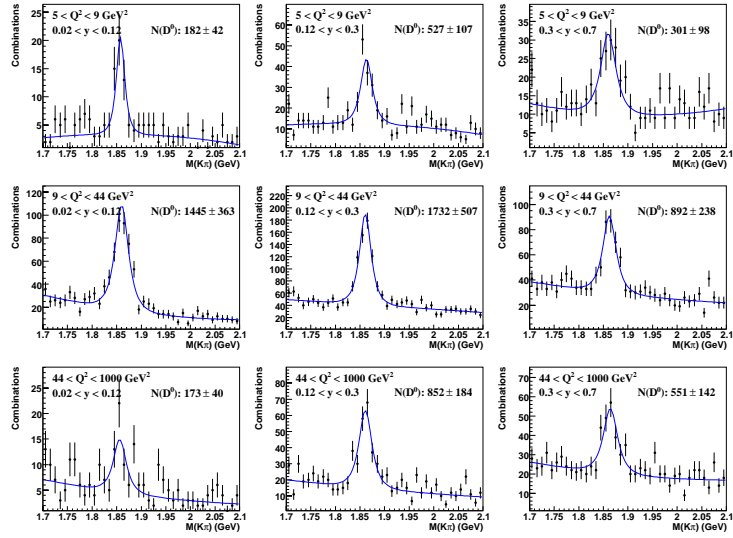
Figure B-38: $M(K\pi)$ *distributions for tagged* D^0 *mesons in data (points) double differential in bins of* Q^2 *and* y. *The fitted sum of a modified Gaussian and background function is also shown (line).*
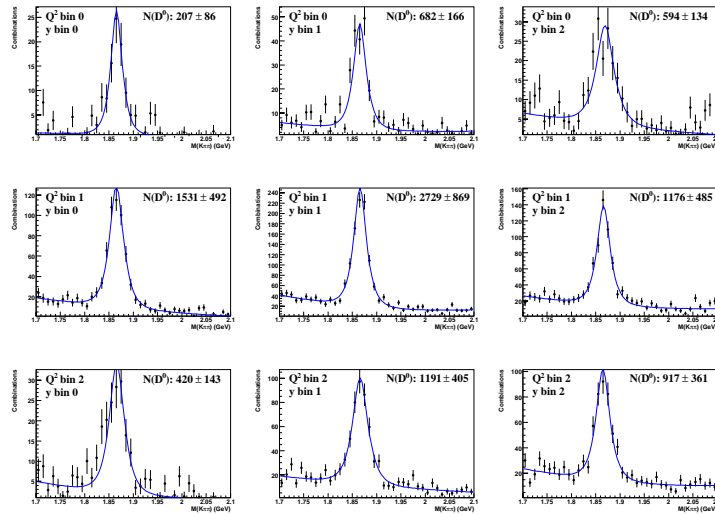
Figure B-39: $M(K\pi)$ *distributions for tagged* D^0 *mesons in MC (points) double differential in bins of* Q^2 *and* y. *The fitted sum of a modified Gaussian and background function is also shown (line).*

177

Appendix C: individual systematic uncertainties

This appendix contains tables showing the systematic uncertainties for each source considered in the D meson cross section analyses.

ID	Systematic source
1	EMC scale uncertainty
2	HAC scale uncertainty
3	MC y_{el} description
4	MC y_{JB} description
5	MC $E - p_z$ description
6	MC z_{vtx} description
7	MC $E_{e'}$ description
8	MC description of scattered electron position in the RCAL
9	b quark contribution to MC sample
10	Simulation of track momentum resolution
11	Simulation of track θ resolution
12	Simulation of track ϕ resolution
13	Simulation of magnetic field
14	MC description of MVD efficiency
15	MC description of S_l
16	MC description of χ^2
17	MC description of p_T^D
18	MC description of η^D
19	Uncertainty from MC weighting correction
20	Uncertainty from background parameterisation
21	Uncertainty from tagged signal (D^0)

Table C-1: *Key to systematic source as used in the following tables.*

D meson	1	2	3	4	5	6	7	8	9	10	11
$D^\pm$	+0.1% −0.0%	+0.1% −0.0%	+0.0% −0.3%	+0.0% −3.4%	+0.0% −0.9%	+0.0% −0.4%	+0.7% −1.2%	+0.1% −0.2%	+1.7% −1.8%	+0.2% −0.8%	+0.3% −0.2%
D^0	+0.1% −0.0%	+0.0% −0.0%	+0.0% −0.1%	+0.0% −0.7%	+0.5% −0.2%	+0.0% −0.1%	+1.5% −0.0%	+0.6% −0.0%	+0.8% −1.1%	+1.2% −0.4%	+0.0% −0.1%

D meson	12	13	14	15	16	17	18	19	20	21
$D^\pm$	+0.5% −0.0%	+0.6% −0.0%	+1.2% −1.2%	+0.1% −8.6%	+3.4% −1.6%	+0.0% −0.0%	+0.0% −0.0%	+0.6% −0.6%	+1.0% −1.0%	/
D^0	+0.1% −0.1%	+2.6% −0.0%	+0.8% −0.8%	+11.3% −5.6%	+0.4% −0.0%	+0.0% −0.0%	+0.0% −0.0%	+0.6% −0.6%	+3.7% −3.7%	+0.1% −0.1%

Table C-2: *Individual systematic uncertainties for total measured $D^\pm$ and D^0 cross sections.*

Q^2 range (GeV^2)	1	2	3	4	5	6	7	8	9	10
5, 10	+0.3% −0.0%	+0.0% −0.2%	+0.2% −0.0%	+0.1% −0.0%	+1.5% −2.7%	+0.2% −0.0%	+4.0% −5.5%	+3.3% −0.0%	+2.3% −2.5%	+1.7% −1.2%
10, 20	+0.3% −0.2%	+0.1% −0.0%	+1.4% −0.0%	+1.4% −2.5%	+2.0% −0.0%	+1.4% −0.0%	+1.4% −0.0%	+2.1% −0.0%	+1.1% −2.0%	+0.0% −2.3%
20, 40	+0.0% −0.4%	+0.2% −0.0%	+0.0% −1.2%	+0.0% −5.6%	+0.0% −2.5%	+0.0% −1.4%	+0.0% −1.6%	+0.0% −1.2%	+1.8% −1.7%	+0.0% −1.7%
40, 80	+0.4% −0.0%	+0.3% −0.0%	+0.0% −0.1%	+0.0% −3.2%	+0.0% −1.9%	+0.0% −0.2%	+1.5% −0.0%	+0.0% −0.1%	+1.8% −0.1%	+0.0% −3.8%
80, 200	+0.3% −0.0%	+0.1% −0.0%	+0.0% −1.1%	+0.0% −3.4%	+0.0% −1.6%	+0.0% −1.1%	+4.8% −0.0%	+0.0% −1.1%	+0.9% −0.7%	+0.1% −6.3%
200, 1000	+0.2% −0.1%	+0.3% −0.0%	+0.0% −6.7%	+0.0% −7.6%	+0.0% −11.0%	+0.0% −6.7%	+0.0% −10.3%	+0.0% −6.7%	+0.0% −2.1%	+1.8% −8.1%

Q^2 range (GeV^2)	11	12	13	14	15	16	17	18	19	20
5, 10	+0.2% −0.0%	+1.2% −0.2%	+3.8% −1.4%	+1.2% −1.2%	+0.1% −12.5%	+6.1% −2.9%	+4.1% −0.0%	+0.0% −0.2%	+1.7% −1.7%	+1.0% −1.0%
10, 20	+0.5% −0.0%	+0.7% −0.8%	+2.0% −3.5%	+1.2% −1.2%	+0.0% −8.2%	+1.5% −3.3%	+3.4% −0.0%	+0.0% −2.1%	+1.6% −1.6%	+1.2% −1.2%
20, 40	+0.1% −0.1%	+0.4% −0.3%	+1.2% −5.4%	+1.2% −1.2%	+22.3% −5.0%	+0.0% −1.1%	+2.6% −0.0%	+0.0% −1.9%	+1.5% −1.5%	+1.4% −1.4%
40, 80	+0.0% −1.3%	+0.9% −2.0%	+1.4% −9.7%	+1.2% −1.2%	+0.0% −6.5%	+3.8% −1.6%	+1.0% −0.0%	+0.0% −3.3%	+0.4% −0.4%	+1.6% −1.6%
80, 200	+0.7% −1.5%	+0.5% −2.1%	+1.0% −14.2%	+1.2% −1.2%	+4.6% −26.4%	+7.1% −4.0%	+0.1% −0.0%	+0.0% −1.6%	+1.4% −1.4%	+2.9% −2.9%
200, 1000	+0.0% −2.2%	+2.3% −3.8%	+8.0% −28.2%	+1.2% −1.2%	+26.4% −26.4%	+22.3% −0.0%	+0.0% −0.9%	+0.0% −1.6%	+8.4% −8.4%	+4.6% −4.6%

Table C-3: *Individual systematic uncertainties for measured $D^{\pm}$ cross sections as a function of Q^2.*

181

x range	1	2	3	4	5	6	7	8	9	10
8e-05, 0.0004	+0.1% −0.6%	+0.0% −0.0%	+0.5% −0.0%	+0.6% −0.0%	+1.3% −1.4%	+0.6% −0.0%	+2.7% −7.4%	+0.4% −0.1%	+0.8% −1.5%	+1.7% −1.4%
0.0004, 0.0016	+0.2% −0.0%	+0.2% −0.0%	+0.0% −0.1%	+0.2% −0.1%	+0.0% −0.8%	+0.0% −0.1%	+1.1% −0.2%	+0.8% −0.0%	+3.0% −2.9%	+0.0% −1.9%
0.0016, 0.005	+0.1% −0.0%	+0.0% −0.0%	+0.0% −0.2%	+0.0% −5.9%	+0.0% −0.6%	+0.0% −0.2%	+0.8% −0.0%	+0.4% −0.1%	+1.5% −1.6%	+0.0% −3.0%
0.005, 0.01	+0.2% −0.0%	+0.3% −0.0%	+0.0% −1.0%	+0.0% −16.6%	+0.0% −4.0%	+0.0% −1.3%	+0.0% −2.2%	+0.0% −1.6%	+0.5% −0.7%	+0.0% −7.0%
0.01, 0.1	+0.4% −0.2%	+0.0% −0.3%	+0.0% −4.6%	+0.0% −16.8%	+0.0% −6.9%	+0.0% −4.6%	+0.0% −4.8%	+0.0% −4.7%	+1.0% −2.5%	+0.0% −4.4%

x range	11	12	13	14	15	16	17	18	19	20
8e-05, 0.0004	+0.4% −0.7%	+1.3% −0.0%	+4.4% −9.3%	+1.2% −1.2%	+12.0% −15.4%	+2.1% −3.0%	+3.4% −0.0%	+0.0% −7.9%	+2.5% −2.5%	+1.6% −1.6%
0.0004, 0.0016	+0.4% −0.0%	+0.7% −0.4%	+1.7% −4.3%	+1.2% −1.2%	+1.8% −4.4%	+1.5% −2.8%	+3.6% −0.0%	+0.0% −0.1%	+1.0% −1.0%	+1.2% −1.2%
0.0016, 0.005	+0.3% −0.7%	+0.5% −1.4%	+1.1% −5.7%	+1.2% −1.2%	+0.0% −8.7%	+5.8% −1.4%	+2.7% −0.0%	+2.3% −0.0%	+0.6% −0.6%	+1.6% −1.6%
0.005, 0.01	+1.1% −2.7%	+0.5% −4.1%	+3.8% −19.1%	+1.2% −1.2%	+7.8% −22.2%	+9.0% −0.0%	+0.2% −0.0%	+3.4% −0.0%	+1.9% −1.9%	+1.8% −1.8%
0.01, 0.1	+0.0% −1.6%	+2.1% −1.3%	+4.0% −17.4%	+1.2% −1.2%	+8.7% −10.4%	+4.3% −0.0%	+0.0% −1.5%	+1.4% −0.0%	+6.6% −6.6%	+0.6% −0.6%

Table C-4: *Individual systematic uncertainties for measured $D^{\pm}$ cross sections as a function of x.*

$p_T^{D^\pm}$ range (GeV)	1	2	3	4	5	6	7	8	9	10
1.5, 2.4	+0.7% −0.0%	+0.3% −0.0%	+1.1% −0.0%	+0.8% −4.6%	+0.0% −1.1%	+1.0% −0.0%	+6.4% −0.0%	+5.7% −0.6%	+5.0% −2.0%	+0.0% −4.1%
2.4, 3.1	+0.3% −0.0%	+0.1% −0.0%	+0.0% −0.2%	+0.0% −2.8%	+0.0% −0.9%	+0.0% −0.2%	+1.3% −0.0%	+0.5% −0.4%	+0.3% −0.4%	+0.0% −2.8%
3.1, 4	+0.1% −0.1%	+0.2% −0.0%	+0.0% −0.4%	+0.0% −3.3%	+0.0% −1.0%	+0.0% −0.4%	+0.0% −1.1%	+1.6% −0.0%	+1.5% −1.5%	+0.5% −1.5%
4, 6	+0.1% −0.1%	+0.0% −0.0%	+0.0% −0.0%	+0.0% −2.9%	+0.4% −0.0%	+0.0% −0.1%	+0.2% −2.6%	+0.8% −2.0%	+1.5% −3.5%	+0.0% −2.5%
6, 15	+0.0% −0.5%	+0.0% −0.1%	+0.0% −0.3%	+0.0% −2.0%	+0.0% −0.6%	+0.0% −0.3%	+1.5% −4.2%	+0.5% −0.1%	+1.5% −2.4%	+0.3% −1.7%

$p_T^{D^\pm}$ range (GeV)	11	12	13	14	15	16	17	18	19	20
1.5, 2.4	+0.8% −1.2%	+1.4% −2.7%	+3.3% −21.0%	+1.2% −1.2%	+0.0% −23.9%	+0.0% −2.9%	+0.0% −0.0%	+0.0% −2.5%	+3.3% −3.3%	+1.1% −1.1%
2.4, 3.1	+0.1% −0.4%	+1.4% −1.1%	+1.0% −9.1%	+1.2% −1.2%	+0.0% −10.0%	+5.2% −0.0%	+0.0% −0.0%	+0.0% −2.0%	+0.1% −0.1%	+1.8% −1.8%
3.1, 4	+0.2% −0.0%	+0.5% −0.6%	+1.3% −1.4%	+1.2% −1.2%	+7.3% −0.0%	+0.0% −2.4%	+0.0% −0.1%	+0.0% −1.2%	+0.8% −0.8%	+2.4% −2.4%
4, 6	+0.0% −0.7%	+0.0% −0.8%	+1.8% −0.9%	+1.2% −1.2%	+8.4% −4.3%	+4.3% −1.2%	+0.0% −0.1%	+0.0% −1.0%	+0.6% −0.6%	+2.9% −2.9%
6, 15	+0.2% −0.0%	+0.9% −0.2%	+0.5% −0.0%	+1.2% −1.2%	+0.9% −6.2%	+10.1% −4.4%	+0.0% −0.0%	+0.1% −0.0%	+0.3% −0.3%	+0.8% −0.8%

Table C-5: *Individual systematic uncertainties for measured $D^\pm$ cross sections as a function of $p_T^{D^\pm}$.*

183

$\eta^{D^\pm}$ range	1	2	3	4	5	6	7	8	9	10
$-1.6, -0.8$	+0.4% / −0.5%	+0.0% / −0.3%	+0.7% / −0.0%	+0.8% / −0.0%	+1.5% / −0.0%	+0.9% / −0.0%	+5.7% / −3.7%	+3.6% / −0.0%	+1.2% / −1.1%	+0.3% / −2.3%
$-0.8, -0.4$	+0.0% / −0.2%	+0.1% / −0.0%	+0.0% / −0.4%	+0.0% / −0.4%	+0.6% / −0.0%	+0.0% / −0.4%	+0.0% / −4.1%	+2.1% / −1.1%	+1.2% / −2.4%	+0.0% / −1.9%
$-0.4, 0$	+0.2% / −0.0%	+0.3% / −0.0%	+0.0% / −0.3%	+0.0% / −0.3%	+0.0% / −0.9%	+0.0% / −0.3%	+0.9% / −1.1%	+0.5% / −2.6%	+2.5% / −1.6%	+0.0% / −2.0%
$0, 0.4$	+0.0% / −0.1%	+0.2% / −0.0%	+0.0% / −0.4%	+0.0% / −0.4%	+2.1% / −0.0%	+0.0% / −0.4%	+0.0% / −0.6%	+0.0% / −1.3%	+2.3% / −3.5%	+0.1% / −2.4%
$0.4, 0.8$	+0.2% / −0.0%	+0.1% / −0.0%	+0.0% / −0.7%	+0.0% / −2.7%	+0.0% / −4.0%	+0.0% / −0.7%	+2.1% / −1.5%	+1.5% / −0.2%	+0.4% / −0.3%	+1.0% / −4.2%
$0.8, 1.6$	+0.4% / −0.0%	+0.0% / −0.1%	+0.0% / −0.6%	+0.0% / −14.9%	+0.0% / −2.6%	+0.0% / −0.8%	+0.3% / −0.5%	+0.0% / −1.6%	+3.8% / −2.6%	+0.0% / −4.2%

$\eta^{D^\pm}$ range	11	12	13	14	15	16	17	18	19	20
$-1.6, -0.8$	+0.1% / −0.0%	+0.5% / −0.8%	+1.1% / −6.7%	+1.2% / −1.2%	+26.4% / −4.1%	+0.9% / −5.2%	+3.8% / −0.0%	+0.2% / −0.0%	+0.7% / −0.7%	+1.8% / −1.8%
$-0.8, -0.4$	+0.1% / −0.0%	+0.6% / −0.0%	+2.8% / −1.5%	+1.2% / −1.2%	+0.0% / −10.4%	+0.1% / −3.9%	+3.3% / −0.0%	+0.1% / −0.0%	+1.2% / −1.2%	+1.5% / −1.5%
$-0.4, 0$	+0.0% / −0.4%	+0.4% / −1.5%	+0.0% / −2.2%	+1.2% / −1.2%	+9.9% / −11.2%	+1.9% / −3.2%	+2.4% / −0.0%	+0.0% / −0.0%	+1.1% / −1.1%	+1.1% / −1.1%
$0, 0.4$	+0.3% / −0.6%	+1.0% / −1.2%	+1.1% / −5.4%	+1.2% / −1.2%	+0.0% / −11.0%	+9.5% / −1.6%	+2.8% / −0.0%	+0.0% / −0.0%	+1.3% / −1.3%	+2.0% / −2.0%
$0.4, 0.8$	+0.7% / −1.3%	+1.2% / −0.8%	+3.6% / −11.7%	+1.2% / −1.2%	+0.0% / −19.1%	+9.0% / −0.0%	+2.7% / −0.0%	+0.0% / −0.2%	+1.0% / −1.0%	+2.4% / −2.4%
$0.8, 1.6$	+0.9% / −0.0%	+1.6% / −1.3%	+3.2% / −16.2%	+1.2% / −1.2%	+13.5% / −6.2%	+5.0% / −5.3%	+2.6% / −0.0%	+0.0% / −0.2%	+3.4% / −3.4%	+1.6% / −1.6%

Table C-6: *Individual systematic uncertainties for measured $D^\pm$ cross sections as a function of $\eta^{D^\pm}$.*

Q^2 range (GeV^2)	1	2	3	4	5	6	7	8	9	10	11
5, 10	+0.0% −0.2%	+0.0% −0.0%	+0.9% −0.0%	+4.2% −0.0%	+1.4% −1.9%	+0.9% −0.0%	+4.6% −2.3%	+9.7% −0.7%	+1.4% −1.1%	+1.7% −0.0%	+0.3% −0.1%
10, 20	+0.0% −0.2%	+0.0% −0.0%	+0.1% −0.0%	+0.0% −5.2%	+1.9% −0.3%	+0.1% −0.0%	+3.0% −0.0%	+0.5% −0.6%	+0.9% −1.3%	+2.4% −0.6%	+0.0% −0.5%
20, 40	+0.1% −0.0%	+0.0% −0.0%	+0.0% −0.6%	+0.0% −0.6%	+1.1% −2.2%	+0.0% −0.7%	+3.8% −1.2%	+0.0% −0.6%	+0.3% −0.5%	+1.5% −0.5%	+0.7% −0.1%
40, 80	+0.3% −0.0%	+0.0% −0.0%	+0.3% −0.0%	+2.5% −0.0%	+3.1% −0.1%	+0.3% −0.0%	+0.8% −1.4%	+0.3% −0.0%	+0.5% −0.5%	+1.8% −1.3%	+0.0% −1.0%
80, 1000	+0.4% −0.0%	+0.0% −0.0%	+0.6% −0.0%	+3.3% −0.0%	+7.6% −1.1%	+0.6% −0.0%	+4.0% −0.6%	+0.6% −0.0%	+0.7% −1.2%	+0.3% −3.5%	+0.3% −0.0%

Q^2 range (GeV^2)	12	13	14	15	16	17	18	19	20	21
5, 10	+0.6% −0.0%	+2.5% −0.0%	+0.8% −0.8%	+7.0% −3.1%	+0.0% −2.0%	+0.0% −4.4%	+0.0% −4.1%	+1.3% −1.3%	+2.7% −2.7%	+3.4% −3.4%
10, 20	+0.0% −0.5%	+0.8% −0.0%	+0.8% −0.8%	+5.9% −0.0%	+1.5% −0.0%	+0.0% −2.4%	+0.0% −6.0%	+1.1% −1.1%	+0.2% −0.2%	+0.3% −0.3%
20, 40	+0.4% −0.0%	+4.1% −1.4%	+0.8% −0.8%	+5.8% −8.5%	+0.3% −0.0%	+0.0% −2.6%	+0.0% −6.4%	+1.2% −1.2%	+4.6% −4.6%	+1.4% −1.4%
40, 80	+0.6% −0.2%	+3.4% −0.0%	+0.8% −0.8%	+0.0% −11.3%	+6.9% −2.2%	+0.0% −1.5%	+0.0% −6.7%	+1.5% −1.5%	+6.7% −6.7%	+6.6% −6.6%
80, 1000	+0.0% −0.6%	+4.0% −0.0%	+0.8% −0.8%	+16.0% −0.0%	+2.8% −7.8%	+0.0% −0.9%	+13.9% −0.0%	+2.0% −2.0%	+19.6% −19.6%	+8.1% −8.1%

Table C-7: *Individual systematic uncertainties for measured D^0 cross sections as a function of Q^2.*

x range	1	2	3	4	5	6	7	8	9	10	11
8e-05, 0.0004	+0.0% −0.4%	+0.0% −0.0%	+0.3% −0.0%	+0.3% −0.4%	+0.0% −2.4%	+0.4% −0.0%	+6.6% −0.0%	+6.7% −2.4%	+2.0% −2.1%	+3.9% −0.0%	+0.7% −1.2%
0.0004, 0.0016	+0.0% −0.1%	+0.0% −0.0%	+0.0% −0.1%	+0.4% −0.1%	+2.2% −0.0%	+0.0% −0.1%	+1.4% −0.2%	+1.0% −0.3%	+0.5% −0.6%	+0.7% −0.8%	+0.0% −0.2%
0.0016, 0.005	+0.4% −0.0%	+0.0% −0.0%	+0.3% −0.0%	+0.2% −4.6%	+1.4% −0.2%	+0.3% −0.0%	+1.1% −0.5%	+1.0% −0.0%	+1.1% −1.6%	+1.1% −1.1%	+0.0% −0.3%
0.005, 0.1	+0.4% −0.0%	+0.0% −0.0%	+0.4% −0.0%	+9.6% −0.0%	+3.0% −0.0%	+0.4% −0.0%	+0.5% −0.0%	+0.2% −0.4%	+0.2% −0.8%	+1.5% −0.4%	+0.3% −0.0%

x range	12	13	14	15	16	17	18	19	20	21
8e-05, 0.0004	+0.3% −0.3%	+1.7% −0.0%	+0.8% −0.8%	+3.4% −0.0%	+0.0% −2.7%	+0.0% −3.5%	+0.0% −10.5%	+1.9% −1.9%	+10.0% −10.0%	+6.4% −6.4%
0.0004, 0.0016	+0.3% −0.3%	+1.6% −0.4%	+0.8% −0.8%	+1.3% −1.6%	+1.2% −0.0%	+0.0% −3.8%	+0.0% −3.2%	+0.8% −0.8%	+7.0% −7.0%	+0.7% −0.7%
0.0016, 0.005	+0.1% −0.0%	+3.8% −0.0%	+0.8% −0.8%	+3.0% −5.4%	+2.0% −0.0%	+0.0% −3.7%	+0.0% −3.7%	+1.0% −1.0%	+4.9% −4.9%	+0.8% −0.8%
0.005, 0.1	+0.0% −0.9%	+3.7% −0.0%	+0.8% −0.8%	+15.9% −0.0%	+0.4% −6.6%	+0.0% −20.9%	+35.2% −0.0%	+2.3% −2.3%	+2.6% −2.6%	+7.7% −7.7%

Table C-8: *Individual systematic uncertainties for measured D^0 cross sections as a function of x.*

$p_T^{D^0}$ range (GeV)	1	2	3	4	5	6	7	8	9	10	11
1.5, 2.4	+0.3% −0.0%	+0.0% −0.0%	+0.2% −0.0%	+0.2% −1.5%	+2.0% −0.0%	+0.1% −0.1%	+5.7% −0.0%	+0.0% −0.6%	+1.3% −1.2%	+0.5% −0.0%	+0.3% −0.3%
2.4, 3.1	+0.0% −0.3%	+0.0% −0.0%	+0.2% −0.0%	+0.2% −0.3%	+0.0% −1.9%	+0.2% −0.0%	+0.0% −1.0%	+1.9% −0.0%	+1.4% −2.0%	+0.4% −1.2%	+0.1% −0.3%
3.1, 4	+0.3% −0.1%	+0.0% −0.0%	+0.1% −0.3%	+0.0% −4.7%	+1.1% −2.5%	+0.0% −0.4%	+1.4% −0.0%	+1.0% −0.3%	+0.8% −1.2%	+0.5% −1.0%	+0.1% −0.5%
4, 6	+0.5% −0.3%	+0.0% −0.0%	+0.1% −0.0%	+0.8% −0.0%	+0.6% −0.6%	+0.2% −0.0%	+0.9% −0.3%	+0.1% −1.6%	+0.0% −0.3%	+3.6% −0.7%	+0.2% −0.0%
6, 15	+0.2% −0.0%	+0.0% −0.0%	+0.1% −0.0%	+0.8% −0.0%	+1.8% −0.1%	+0.1% −0.0%	+0.0% −5.1%	+1.1% −0.0%	+0.7% −0.3%	+2.3% −0.0%	+0.3% −0.0%

$p_T^{D^0}$ range (GeV)	12	13	14	15	16	17	18	19	20	21
1.5, 2.4	+0.6% −0.1%	+0.0% −2.4%	+0.8% −0.8%	+4.9% −6.5%	+2.7% −0.3%	+0.0% −0.0%	+0.0% −6.3%	+1.4% −1.4%	+0.9% −0.9%	+1.9% −1.9%
2.4, 3.1	+0.2% −0.0%	+4.8% −0.0%	+0.8% −0.8%	+1.2% −0.0%	+0.0% −1.6%	+0.0% −0.0%	+0.0% −6.4%	+1.2% −1.2%	+9.9% −9.9%	+0.1% −0.1%
3.1, 4	+0.0% −0.9%	+5.5% −0.1%	+0.8% −0.8%	+6.6% −6.1%	+0.9% −0.0%	+0.0% −0.0%	+0.0% −5.2%	+1.1% −1.1%	+4.0% −4.0%	+1.8% −1.8%
4, 6	+0.3% −0.0%	+4.0% −0.0%	+0.8% −0.8%	+1.0% −2.1%	+0.6% −0.0%	+0.0% −0.0%	+0.0% −4.6%	+0.8% −0.8%	+2.0% −2.0%	+0.6% −0.6%
6, 15	+0.2% −0.7%	+4.4% −0.6%	+0.8% −0.8%	+12.0% −1.3%	+0.5% −0.3%	+0.0% −0.1%	+0.0% −3.0%	+0.7% −0.7%	+14.6% −14.6%	+3.1% −3.1%

Table C-9: *Individual systematic uncertainties for measured D^0 cross sections as a function of $p_T^{D^0}$.*

187

$\eta^{D^\pm}$ range	1	2	3	4	5	6	7	8	9	10	11
-1.6, -0.8	+0.1% -0.2%	+0.0% -0.0%	+0.1% -0.0%	+0.1% -0.2%	+2.3% -0.8%	+0.1% -0.0%	+4.5% -0.1%	+4.8% -2.0%	+0.1% -0.5%	+2.4% -3.2%	+0.9% -0.8%
-0.8, -0.4	+0.6% -0.0%	+0.0% -0.0%	+0.4% -0.0%	+0.4% -0.0%	+5.5% -0.0%	+0.4% -0.0%	+0.1% -2.8%	+3.5% -2.0%	+0.5% -0.5%	+1.1% -0.8%	+0.0% -0.5%
-0.4, 0	+0.0% -0.3%	+0.0% -0.0%	+0.0% -0.2%	+0.0% -0.2%	+0.0% -2.0%	+0.0% -0.2%	+2.1% -0.0%	+0.0% -1.9%	+1.3% -1.5%	+3.0% -0.0%	+0.0% -0.4%
0, 0.4	+0.0% -0.4%	+0.0% -0.0%	+0.0% -0.3%	+0.0% -1.4%	+1.8% -0.0%	+0.0% -0.2%	+0.7% -0.0%	+1.2% -0.0%	+0.2% -1.0%	+1.3% -1.5%	+0.3% -0.0%
0.4, 0.8	+0.3% -0.0%	+0.0% -0.0%	+0.7% -0.0%	+0.4% -0.0%	+0.0% -4.2%	+0.4% -0.0%	+4.1% -0.0%	+3.3% -0.0%	+1.2% -1.5%	+0.5% -0.0%	+0.3% -0.5%
0.8, 1.6	+0.7% -0.0%	+0.0% -0.0%	+0.5% -0.0%	+0.5% -9.7%	+3.6% -0.0%	+0.5% -0.0%	+4.7% -3.1%	+4.4% -2.8%	+1.3% -1.2%	+0.1% -0.0%	+0.6% -0.6%

$\eta^{D^\pm}$ range	12	13	14	15	16	17	18	19	20	21
-1.6, -0.8	+0.1% -0.5%	+3.7% -0.7%	+0.8% -0.8%	+0.6% -0.6%	+0.7% -1.7%	+0.0% -3.3%	+0.0% -0.0%	+1.3% -1.3%	+0.8% -0.8%	+15.3% -15.3%
-0.8, -0.4	+0.0% -0.7%	+1.6% -0.0%	+0.8% -0.8%	+1.2% -1.7%	+1.2% -1.7%	+0.0% -3.9%	+0.0% -0.0%	+1.1% -1.1%	+12.1% -12.1%	+0.2% -0.2%
-0.4, 0	+0.9% -0.0%	+4.4% -0.2%	+0.8% -0.8%	+0.0% -14.3%	+4.7% -0.0%	+0.0% -3.8%	+0.0% -0.0%	+1.4% -1.4%	+10.2% -10.2%	+1.0% -1.0%
0, 0.4	+0.4% -0.4%	+0.3% -1.7%	+0.8% -0.8%	+14.7% -0.0%	+2.0% -0.0%	+0.0% -3.5%	+0.0% -0.0%	+1.5% -1.5%	+2.9% -2.9%	+3.0% -3.0%
0.4, 0.8	+0.2% -0.2%	+3.8% -0.0%	+0.8% -0.8%	+7.4% -8.3%	+1.7% -0.7%	+0.0% -4.9%	+0.0% -0.0%	+1.6% -1.6%	+0.6% -0.6%	+2.0% -2.0%
0.8, 1.6	+0.3% -0.6%	+2.2% -0.0%	+0.8% -0.8%	+15.5% -0.0%	+0.0% -3.2%	+0.0% -5.2%	+0.0% -0.0%	+1.6% -1.6%	+8.3% -8.3%	+2.2% -2.2%

Table C-10: *Individual systematic uncertainties for measured D^0 cross sections as a function of η^{D^0}.*

$\eta^{D^\pm}$ range	$p_T^{D^\pm}$ range (GeV)	1	2	3	4	5	6	7	8	9	10
$\eta < 0$	1.5, 4	+0.2% −0.0%	+0.2% −0.0%	+0.2% −0.0%	+0.2% −0.0%	+0.1% −0.0%	+0.2% −0.0%	+2.0% −0.0%	+1.3% −0.0%	+4.8% −0.5%	+0.0% −2.4%
	4, 6	+0.0% −0.2%	+0.1% −0.0%	+0.0% −0.0%	+0.0% −0.0%	+0.7% −0.2%	+0.0% −0.0%	+0.0% −3.3%	+1.3% −0.7%	+5.9% −3.8%	+0.0% −1.7%
	6, 15	+0.0% −1.0%	+0.0% −0.4%	+0.0% −0.5%	+0.0% −0.8%	+0.0% −2.3%	+0.0% −0.5%	+2.8% −7.0%	+0.7% −1.6%	+4.0% −2.4%	+0.0% −1.4%
$\eta > 0$	1.5, 4	+0.3% −0.0%	+0.2% −0.0%	+0.0% −0.0%	+0.0% −6.1%	+0.0% −1.4%	+0.0% −0.1%	+1.6% −0.0%	+3.2% −0.9%	+5.7% −1.3%	+0.0% −3.6%
	4, 6	+0.1% −0.0%	+0.0% −0.1%	+0.0% −0.1%	+0.0% −5.6%	+0.4% −0.0%	+0.0% −0.1%	+1.2% −2.2%	+0.2% −3.2%	+4.0% −3.3%	+0.0% −3.4%
	6, 15	+0.0% −0.2%	+0.0% −0.0%	+0.0% −7.4%	+0.0% −10.0%	+0.0% −6.9%	+0.0% −7.4%	+0.0% −9.7%	+0.0% −8.2%	+5.4% −2.5%	+1.1% −0.6%

$\eta^{D^\pm}$ range	$p_T^{D^\pm}$ range (GeV)	11	12	13	14	15	16	17	18	19	20
$\eta < 0$	1.5, 4	+0.0% −0.2%	+0.7% −1.5%	+1.4% −6.6%	+1.2% −1.2%	+4.1% −13.5%	+0.0% −3.2%	+4.4% −0.0%	+0.0% −7.5%	+1.1% −1.1%	+1.2% −1.2%
	4, 6	+0.0% −0.4%	+0.0% −0.2%	+1.0% −0.0%	+1.2% −1.2%	+20.7% −3.0%	+5.8% −1.0%	+0.1% −0.0%	+0.0% −4.7%	+0.5% −0.5%	+2.8% −2.8%
	6, 15	+0.1% −0.6%	+0.1% −0.1%	+5.3% −1.5%	+1.2% −1.2%	+3.7% −8.9%	+9.2% −7.9%	+0.2% −0.0%	+0.0% −1.6%	+0.3% −0.3%	+2.4% −2.4%
$\eta > 0$	1.5, 4	+0.7% −0.8%	+1.5% −1.4%	+2.8% −15.4%	+1.2% −1.2%	+0.0% −10.7%	+3.5% −0.0%	+4.4% −0.0%	+3.1% −0.0%	+2.1% −2.1%	+2.0% −2.0%
	4, 6	+0.2% −1.2%	+0.2% −1.6%	+2.4% −2.7%	+1.2% −1.2%	+0.0% −5.9%	+2.5% −1.4%	+0.0% −0.3%	+2.2% −0.0%	+1.1% −1.1%	+2.9% −2.9%
	6, 15	+0.1% −0.0%	+1.6% −0.1%	+2.9% −1.4%	+1.2% −1.2%	+0.0% −3.9%	+10.3% −2.6%	+0.0% −0.2%	+1.0% −0.0%	+0.4% −0.4%	+1.1% −1.1%

Table C-11: *Individual systematic uncertainties for measured $D^\pm$ cross sections in bins of $p_T^{D^\pm}$ and $\eta^{D^\pm}$.*

189

Q^2 range (GeV²)	y range	1	2	3	4	5	6	7	8	9	10
5, 9	0.02, 0.12	+1.5% −0.0%	+0.0% −0.4%	+1.1% −0.0%	+0.9% −1.8%	+14.7% −1.5%	+1.1% −0.0%	+1.1% −0.0%	+25.8% −4.2%	+4.0% −1.1%	+4.7% −2.2%
	0.12, 0.3	+0.0% −0.5%	+0.0% −0.1%	+0.5% −0.0%	+0.6% −0.0%	+0.0% −5.5%	+0.5% −0.0%	+3.0% −0.0%	+8.4% −0.0%	+6.7% −7.7%	+1.8% −2.6%
	0.3, 0.7	+0.0% −0.9%	+0.0% −0.6%	+2.1% −0.0%	+2.3% −0.0%	+5.3% −4.0%	+2.1% −0.0%	+4.5% −11.6%	+0.0% −10.8%	+5.3% −0.0%	+1.2% −0.7%
9, 44	0.02, 0.12	+0.1% −0.1%	+0.0% −0.1%	+0.0% −0.0%	+0.0% −10.8%	+0.4% −0.3%	+0.0% −0.1%	+0.0% −0.0%	+0.7% −0.0%	+4.8% −1.0%	+0.0% −1.4%
	0.12, 0.3	+0.1% −0.1%	+0.1% −0.0%	+0.3% −0.0%	+0.6% −0.0%	+0.5% −1.0%	+0.3% −0.0%	+0.0% −0.4%	+0.9% −0.6%	+3.9% −1.4%	+0.0% −2.1%
	0.3, 0.7	+0.3% −0.6%	+0.4% −0.0%	+0.0% −0.5%	+0.0% −0.6%	+0.0% −2.1%	+0.0% −0.4%	+1.7% −4.8%	+0.0% −1.8%	+8.5% −4.5%	+0.0% −2.8%
44, 1000	0.02, 0.12	+0.2% −0.0%	+0.0% −0.1%	+0.0% −0.8%	+0.0% −11.0%	+0.0% −4.5%	+0.0% −0.9%	+0.0% −0.8%	+0.0% −0.8%	+2.8% −0.0%	+0.1% −3.5%
	0.12, 0.3	+0.0% −0.1%	+0.1% −0.0%	+0.0% −1.4%	+0.0% −1.4%	+0.0% −2.8%	+0.0% −1.4%	+0.0% −1.4%	+0.0% −1.4%	+2.5% −0.0%	+0.0% −4.1%
	0.3, 0.7	+0.8% −0.0%	+0.5% −0.0%	+0.0% −1.9%	+0.0% −2.0%	+0.0% −3.2%	+0.0% −2.0%	+3.3% −0.0%	+0.0% −1.9%	+7.7% −4.0%	+0.1% −7.3%

Q^2 range (GeV²)	y range	11	12	13	14	15	16	17	18	19	20
5, 9	0.02, 0.12	+0.6% −0.9%	+0.0% −2.0%	+1.7% −0.0%	+1.2% −1.2%	+4.7% −26.4%	+6.4% −0.0%	+6.1% −0.0%	+3.4% −0.0%	+5.2% −5.2%	+7.6% −7.6%
	0.12, 0.3	+0.0% −0.9%	+1.6% −0.0%	+1.2% −0.0%	+1.2% −1.2%	+0.0% −25.9%	+2.8% −3.1%	+3.7% −0.0%	+0.0% −3.5%	+2.8% −2.8%	+1.4% −1.4%
	0.3, 0.7	+3.7% −0.5%	+2.2% −0.0%	+4.1% −4.5%	+1.2% −1.2%	+26.4% −0.0%	+1.8% −12.0%	+2.6% −0.0%	+0.0% −8.3%	+11.1% −11.1%	+0.1% −0.1%
9, 44	0.02, 0.12	+0.3% −0.0%	+0.0% −1.2%	+2.8% −1.2%	+1.2% −1.2%	+0.3% −7.5%	+1.2% −3.0%	+3.6% −0.0%	+2.7% −0.0%	+1.0% −1.0%	+0.0% −0.0%
	0.12, 0.3	+0.2% −0.0%	+0.9% −0.0%	+0.7% −2.6%	+1.2% −1.2%	+0.0% −3.8%	+3.6% −0.1%	+3.4% −0.0%	+0.0% −1.9%	+1.1% −1.1%	+1.5% −1.5%
	0.3, 0.7	+0.5% −0.7%	+0.7% −1.6%	+3.0% −12.8%	+1.2% −1.2%	+4.7% −17.6%	+2.9% −9.1%	+2.7% −0.0%	+0.0% −10.2%	+2.8% −2.8%	+1.8% −1.8%
44, 1000	0.02, 0.12	+0.1% −0.2%	+0.2% −1.7%	+0.5% −6.0%	+1.2% −1.2%	+1.7% −7.2%	+0.4% −3.9%	+0.3% −0.0%	+0.9% −0.0%	+3.0% −3.0%	+2.5% −2.5%
	0.12, 0.3	+0.0% −1.6%	+1.0% −2.6%	+0.9% −11.0%	+1.2% −1.2%	+0.0% −18.9%	+13.3% −0.0%	+0.2% −0.0%	+0.0% −0.8%	+0.0% −0.0%	+2.5% −2.5%
	0.3, 0.7	+0.4% −1.7%	+0.7% −2.8%	+3.1% −20.3%	+1.2% −1.2%	+6.4% −0.0%	+0.0% −7.0%	+0.1% −0.0%	+0.0% −8.1%	+0.2% −0.2%	+3.7% −3.7%

Table C-12: *Individual systematic uncertainties for measured $D^{\pm}$ cross sections in bins of Q^2 and y.*

Table C-13 (part 1): columns 1–11

η^{D^0} range	$p_T^{D^0}$ range (GeV)	1	2	3	4	5	6	7	8	9	10	11
$\eta < 0$	1.5, 4	+0.0% −0.2%	+0.0% −0.0%	+0.0% −0.1%	+0.0% −0.2%	+1.5% −0.4%	+0.0% −0.2%	+2.1% −0.2%	+2.4% −2.1%	+1.0% −1.3%	+2.0% −0.9%	+0.1% −0.5%
	4, 6	+0.8% −0.1%	+0.0% −0.0%	+0.6% −0.0%	+0.6% −0.0%	+1.4% −0.7%	+0.6% −0.0%	+3.3% −0.3%	+0.1% −0.0%	+0.0% −0.3%	+3.1% −1.2%	+0.7% −0.0%
	6, 15	+0.0% −0.5%	+0.0% −0.0%	+0.0% −0.1%	+0.0% −1.0%	+0.1% −0.6%	+0.0% −0.1%	+0.0% −11.1%	+0.0% −1.5%	+0.7% −0.7%	+3.7% −0.0%	+0.8% −0.7%
$\eta > 0$	1.5, 4	+0.2% −0.0%	+0.0% −0.0%	+0.2% −0.0%	+0.3% −4.0%	+0.4% −0.1%	+0.2% −0.0%	+5.0% −0.0%	+1.9% −0.2%	+1.4% −1.7%	+0.0% −1.6%	+0.3% −0.2%
	4, 6	+0.2% −0.6%	+0.0% −0.0%	+0.0% −0.0%	+0.0% −0.1%	+1.1% −0.2%	+0.0% −0.0%	+0.0% −1.4%	+0.0% −2.7%	+0.0% −0.4%	+3.9% −0.0%	+0.0% −0.2%
	6, 15	+0.4% −0.0%	+0.0% −0.0%	+0.0% −8.5%	+0.0% −8.7%	+0.0% −8.0%	+0.0% −8.6%	+0.0% −11.0%	+0.0% −6.4%	+0.7% −0.2%	+0.5% −0.6%	+0.5% −0.4%

Table C-13 (part 2): columns 12–21

η^{D^0} range	$p_T^{D^0}$ range (GeV)	12	13	14	15	16	17	18	19	20	21
$\eta < 0$	1.5, 4	+0.3% −0.2%	+2.5% −0.5%	+0.8% −0.8%	+0.0% −6.7%	+1.5% −0.0%	+0.0% −2.1%	+0.0% −8.7%	+0.9% −0.9%	+9.4% −9.4%	+3.0% −3.0%
	4, 6	+0.4% −0.0%	+5.5% −0.2%	+0.8% −0.8%	+0.0% −8.5%	+2.7% −0.1%	+0.0% −0.0%	+0.0% −7.3%	+1.1% −1.1%	+9.3% −9.3%	+3.5% −3.5%
	6, 15	+0.0% −1.4%	+4.8% −0.0%	+0.8% −0.8%	+2.4% −0.0%	+0.0% −2.5%	+0.0% −0.1%	+0.0% −3.6%	+1.3% −1.3%	+17.6% −17.6%	+6.1% −6.1%
$\eta > 0$	1.5, 4	+0.0% −0.3%	+0.6% −0.6%	+0.8% −0.8%	+11.9% −0.0%	+0.0% −0.3%	+0.0% −2.2%	+0.0% −3.6%	+1.3% −1.3%	+0.1% −0.1%	+1.7% −1.7%
	4, 6	+0.1% −0.0%	+3.3% −0.0%	+0.8% −0.8%	+3.8% −0.0%	+1.2% −0.3%	+0.0% −0.0%	+0.0% −2.6%	+1.1% −1.1%	+5.1% −5.1%	+0.7% −0.7%
	6, 15	+0.6% −0.4%	+7.7% −2.0%	+0.8% −0.8%	+14.9% −4.6%	+0.6% −0.6%	+0.0% −0.0%	+0.0% −2.4%	+0.9% −0.9%	+15.4% −15.4%	+1.6% −1.6%

Table C-13: *Individual systematic uncertainties for measured D^0 cross sections in bins of $p_T^{D^0}$ and η^{D^0}.*

191

Q^2 range (GeV²)	y range	1	2	3	4	5	6	7	8	9	10	11
5, 9	0.02, 0.12	+0.5% −0.0%	+0.0% −0.0%	+1.7% −0.0%	+14.7% −0.0%	+5.3% −3.7%	+1.2% −0.0%	+2.0% −0.0%	+15.0% −0.0%	+0.0% −2.5%	+0.5% −2.5%	+0.0% −1.4%
	0.12, 0.3	+0.0% −1.2%	+0.0% −0.0%	+0.9% −0.0%	+0.9% −0.3%	+0.0% −5.7%	+1.0% −0.0%	+2.7% −0.0%	+10.3% −5.3%	+1.2% −0.0%	+1.3% −1.6%	+2.5% −0.0%
	0.3, 0.7	+0.9% −1.0%	+0.0% −0.0%	+0.7% −0.0%	+0.8% −0.0%	+2.2% −8.5%	+0.7% −0.0%	+6.9% −14.4%	+10.0% −4.6%	+5.1% −4.9%	+3.6% −0.0%	+0.8% −1.1%
9, 44	0.02, 0.12	+0.1% −0.1%	+0.0% −0.0%	+0.0% −0.4%	+0.0% −4.1%	+0.0% −1.6%	+0.0% −0.5%	+0.0% −0.5%	+0.9% −0.0%	+0.5% −0.5%	+0.8% −1.9%	+0.8% −0.6%
	0.12, 0.3	+0.0% −0.0%	+0.0% −0.0%	+0.0% −0.0%	+0.0% −0.1%	+1.3% −0.0%	+0.0% −0.1%	+0.3% −0.0%	+1.0% −0.0%	+0.5% −0.6%	+1.7% −0.0%	+0.0% −0.4%
	0.3, 0.7	+0.2% −0.2%	+0.0% −0.0%	+0.3% −0.0%	+0.4% −0.0%	+2.1% −0.0%	+0.3% −0.0%	+11.7% −0.0%	+1.5% −1.4%	+1.5% −1.4%	+2.3% −0.0%	+0.3% −0.0%
44, 1000	0.02, 0.12	+1.1% −0.0%	+0.0% −0.0%	+2.2% −0.0%	+17.7% −0.0%	+14.6% −0.0%	+2.2% −0.0%	+2.2% −0.0%	+2.2% −0.0%	+0.9% −1.2%	+0.0% −2.2%	+1.4% −0.2%
	0.12, 0.3	+0.4% −0.0%	+0.0% −0.0%	+0.0% −0.5%	+0.0% −0.5%	+2.4% −2.4%	+0.0% −0.4%	+0.0% −0.3%	+0.0% −0.5%	+1.3% −1.2%	+2.4% −0.0%	+0.0% −1.0%
	0.3, 0.7	+0.4% −0.0%	+0.0% −0.0%	+0.0% −0.0%	+0.0% −0.0%	+1.2% −0.0%	+0.0% −0.5%	+0.0% −8.5%	+0.0% −0.0%	+0.2% −1.4%	+0.0% −3.9%	+0.9% −0.7%

Q^2 range (GeV²)	y range	12	13	14	15	16	17	18	19	20	21
5, 9	0.02, 0.12	+0.0% −1.8%	+6.2% −0.0%	+0.8% −0.8%	+0.0% −7.7%	+3.0% −1.6%	+0.0% −3.8%	+0.0% −3.1%	+2.0% −2.0%	+16.6% −16.6%	+0.4% −0.4%
	0.12, 0.3	+2.4% −0.0%	+3.0% −0.0%	+0.8% −0.8%	+4.4% −5.1%	+0.0% −4.1%	+0.0% −3.8%	+0.0% −3.8%	+1.6% −1.6%	+5.6% −5.6%	+2.5% −2.5%
	0.3, 0.7	+1.1% −0.0%	+4.1% −0.0%	+0.8% −0.8%	+11.5% −0.0%	+2.4% −11.6%	+0.0% −2.3%	+0.0% −14.9%	+3.6% −3.6%	+0.5% −0.5%	+14.8% −14.8%
9, 44	0.02, 0.12	+0.2% −0.3%	+2.4% −0.0%	+0.8% −0.8%	+2.1% −0.0%	+0.4% −0.0%	+0.0% −2.1%	+0.0% −3.1%	+1.1% −1.1%	+4.2% −4.2%	+1.7% −1.7%
	0.12, 0.3	+0.0% −0.2%	+1.3% −1.3%	+0.8% −0.8%	+0.6% −0.4%	+1.3% −0.0%	+0.0% −1.8%	+0.0% −3.1%	+0.9% −0.9%	+1.5% −1.5%	+0.5% −0.5%
	0.3, 0.7	+0.0% −0.6%	+2.6% −0.0%	+0.8% −0.8%	+13.7% −1.9%	+5.4% −0.1%	+0.0% −1.0%	+0.0% −14.2%	+2.4% −2.4%	+1.4% −1.4%	+0.9% −0.9%
44, 1000	0.02, 0.12	+0.7% −1.3%	+3.2% −0.1%	+0.8% −0.8%	+10.4% −0.0%	+2.6% −7.8%	+0.0% −0.9%	+0.0% −1.7%	+2.7% −2.7%	+16.9% −16.9%	+0.9% −0.9%
	0.12, 0.3	+0.3% −0.0%	+2.7% −0.0%	+0.8% −0.8%	+8.9% −3.4%	+2.5% −1.8%	+0.0% −0.2%	+0.0% −2.4%	+2.4% −2.4%	+3.8% −3.8%	+3.7% −3.7%
	0.3, 0.7	+0.1% −0.8%	+4.7% −0.0%	+0.8% −0.8%	+0.0% −16.0%	+5.4% −0.0%	+0.4% −0.0%	+0.0% −11.6%	+1.9% −1.9%	+26.0% −26.0%	+4.1% −4.1%

Table C-14: *Individual systematic uncertainties for measured D^0 cross sections in bins of Q^2 and y.*

Bibliography

[1] R.P. Feynman, Phys. Rev. Lett. **23**, 1415 (1969).

[2] J.D. Bjorken, Phys. Rev. **179**, 1547 (1969).

[3] G. Miller et al., Phys. Rev. **D 5**, 528 (1972).

[4] M. Gell-Mann, Phys. Lett. **8**, 214 (1964).

[5] T. Eichten et al., Phys. Lett. **B 46**, 274 (1973).

[6] R. Brandelik et al., Phys. Lett. **B 86**, 243 (1979).

[7] ZEUS Coll., M. Derrick et al., Phys. Lett. **B 316**, 412 (1993);
    H1 Coll., I. Abt et al., Nucl. Phys. **B 407**, 515 (1993).

[8] A.D. Martin et al., Eur. Phys. J. **C 23**, 73 (2002).

[9] J. Pumplin et al., JHEP **07**, 012 (2002).

[10] V.N. Gribov and L.N. Lipatov, Sov. J. Nucl. Phys. **15**, 438 (1972);
    L.N. Lipatov, Sov. J. Nucl. Phys. **20**, 94 (1975);
    G. Altarelli and G. Parisi, Nucl. Phys. **B 126**, 298 (1977);
    Yu.L. Dokshitzer, Sov. Phys. JETP **46**, 641 (1977).

[11] S.L. Glashow et al., Phys. Rev. **D 2**, 1285 (1970).

[12] J.J. Aubert et al., Phys. Rev. Lett. **33**, 1404 (1974);
J.E. Augustin et al., Phys. Rev. Lett. **33**, 1406 (1974).

[13] R. Devenish and A. Cooper-Sarkar, *Deep Inelastic Scattering*. Oxford University Press, 2003.

[14] B.W. Harris and J. Smith, Phys. Rev. **D 57**, 2806 (1998).

[15] R. Thorne, *private communication* (unpublished). 2008.

[16] D. Buskulic et al., Phys. Lett. **B 388**, 648 (1996).

[17] J.D. Bjorken,, Phys. Rev. **D 17**, 171 (1978).

[18] P. Nason et al., Nucl. Phys. **B 565**, 245 (2000).

[19] Y.-M. Yao et al. (Particle Data Group), Journal of Physics G **33** (2006).

[20] ZEUS Coll., S. Chekanov et al., JHEP **07**, 074 (2007).

[21] S. Chekanov et al., Eur. Phys. J. **C 44**, 351 (2005).

[22] L. Gladilin, Preprint hep-ex/9912064, 1999.

[23] H1 Coll., A. Aktas et al., Eur. Phys. J. **C 38**, 447 (2005).

[24] G. Blaylock, Int. J. Mod. Phys. **A 15S1**, 80 (2000).

[25] ZEUS Coll., S. Chekanov et al., Phys. Rev. **D 69**, 012004 (2004).

[26] A. Aktas et al., Eur. Phys. J. **C 45**, 23 (2006).

[27] ZEUS Coll., U. Holm (ed.), *The ZEUS Detector*. Status Report (unpublished), DESY (1993), available on http://www-zeus.desy.de/bluebook/bluebook.html.

[28] A. Polini et al., Nucl. Inst. Meth. **A 581**, 656 (2007).

[29] N. Harnew et al., Nucl. Inst. Meth. **A 279**, 290 (1989);
B. Foster et al., Nucl. Phys. Proc. Suppl. **B 32**, 181 (1993);
B. Foster et al., Nucl. Inst. Meth. **A 338**, 254 (1994).

[30] M. Derrick et al., Nucl. Inst. Meth. **A 309**, 77 (1991).

[31] A. Andresen et al., Nucl. Inst. Meth. **A 309**, 101 (1991).

[32] H. Bethe and W. Heitler, Proc. Roy. Soc. Lond. **A 146**, 83 (1934).

[33] J. Andruszków et al., Preprint DESY-92-066, DESY, 1992;
ZEUS Coll., M. Derrick et al., Z. Phys. **C 63**, 391 (1994);
J. Andruszków et al., Acta Phys. Pol. **B 32**, 2025 (2001).

[34] M. Helbich et al., Nucl. Inst. Meth. **A 565**, 572 (2006).

[35] W. H. Smith, K. Tokushuku and L. W. Wiggers, *Proc. Computing in High-Energy Physics (CHEP), Annecy, France, Sept. 1992*, C. Verkerk and W. Wojcik (eds.), p. 222. CERN, Geneva, Switzerland (1992). Also in preprint DESY 92-150B.

[36] P.D. Allfrey et al., Nucl. Inst. Meth. **A 580**, 1257 (2007).

[37] K. Korcsak-Gorzo et al., Nucl. Inst. Meth. **A 580**, 1227 (2007).

[38] T. Kohno, Nucl. Inst. Meth. **A 559**, 153 (2006).

[39] V. Blobel, *Linear least square fits with a large number of parameters* (2000), available on http://www.desy.de/~blobel.

[40] E. Maddox, *Study of heavy quark production at HERA using the ZEUS microvertex detector*. Ph.D. Thesis, NIKHEF, Amsterdam, Netherlands, 2004.

[41] R. Mankel, *Mathematical framework for the ZEUS microvertex detector* (unpublished). ZEUS-07-002, internal ZEUS note, 2007.

[42] F. Jacquet and A. Blondel, *Proc. the Study of an eP Facility for Europe*, U. Amaldi (ed.), p. 391. (1979). Also in preprint DESY 79-48.

[43] S. Bentvelsen, J. Engelen and P. Kooijman, *Proc. Workshop on Physics at HERA*, W. Buchmüller and G. Ingelman (eds.), Vol. 1, p. 23. Hamburg, Germany, DESY (1992).

[44] G.F. Hartner, *VCTRAK Briefing: Program and Math* (unpublished). ZEUS-98-058, internal ZEUS Note, 1998.

[45] R. Hall-Wilton et al., *The CTD tracking resolution* (unpublished). ZEUS-99-024, internal ZEUS note, 1999.

[46] H. Stadie, *New Vertex Tools & How to Use Them* (unpublished). 2/8/2006, internal ZEUS presentation, 2006.

[47] P. Billoir, R. Frühwirth and M. Regler, Nucl. Inst. Meth. **A 241**, 115 (1985).

[48] R. Mankel, *How Wide is the HERA-II Beam Spot* (unpublished). 24/5/2006, internal ZEUS presentation, 2006.

[49] F. Karstens, *HERA II D meson finders* (unpublished). 16/2/2006, internal ZEUS presentation, 2006.

[50] R. Brun et al., GEANT3, Technical Report CERN-DD/EE/84-1, CERN, 1987.

[51] H. Jung, Comp. Phys. Comm. **86**, 147 (1995).

[52] M. Glück, E. Reya and A. Vogt, Z. Phys. **C 67**, 433 (1995).

[53] L. Lonnblad, Comp. Phys. Comm. **71**, 15 (1992).

[54] B. Andersson et al., Phys. Rep. **97**, 31 (1983).

[55] S. Chekanov et al., *Measurement of D^* cross sections and the charm structure function of the proton in DIS at HERA* (unpublished). ZEUS-05-016, internal ZEUS Note, 2005.

[56] G.M. Briskin, *Diffractive Dissociation in ep Deep Inelastic Scattering*. Ph.D. Thesis, Tel Aviv University, Report DESY-THESIS 1998-036, 1998.

[57] J. Gassner, *A measurement of D-meson production at HERA by decay vertex identification.* Ph.D. Thesis, ETH Zürich, 2002.

[58] ZEUS Coll., S. Chekanov et al., Phys. Rev. **D 69**, 12004 (2004).

[59] M. Wing, *Measurement of the charm fragmentation function in D^* photoproduction at HERA* (unpublished). 7/2/2008, internal ZEUS presentation, 2008.

[60] ZEUS Coll., S. Chekanov et al., Phys. Rev. **D 67**, 012007 (2003).

[61] ZEUS Coll., J. Breitweg et al., Eur. Phys. J. **C 12**, 35 (2000).

[62] A. Glazov, *DIS2005, Proceedings of the 13th International Workshop on Deep Inelastic Scattering*, W. H. Smith et al. (ed.), pp. 237–240. American Institue of Physics (2005).